

---

# LEARNING THE EFFECTIVE DYNAMICS OF COMPLEX MULTISCALE SYSTEMS

---

A PREPRINT - NOVEMBER 26, 2021

 **Pantelis R. Vlachas**

Computational Science and Engineering Laboratory  
ETH Zürich  
CH-8092, Switzerland  
vlachas@collegium.ethz.ch

 **Georgios Arampatzis**

Computational Science and Engineering Laboratory  
ETH Zürich  
CH-8092, Switzerland  
garampat@ethz.ch

 **Caroline Uhler**

Institute for Data, Systems, and Society  
Massachusetts Institute of Technology  
Massachusetts Avenue 77, Cambridge, MA 02139, USA  
garampat@ethz.ch

 **Petros Koumoutsakos\***

Computational Science and Engineering Laboratory  
ETH Zürich  
CH-8092, Switzerland  
petros@ethz.ch

November 26, 2021

## ABSTRACT

Simulations of complex multiscale systems are essential for science and technology ranging from weather forecasting to aircraft design. The predictive capabilities of simulations hinges on their capacity to capture the governing system dynamics. Large scale simulations, resolving all spatiotemporal scales, provide invaluable insight at a high computational cost. In turn, simulations using reduced order models are affordable but their veracity hinges often on linearisation and/or heuristics. Here we present a novel systematic framework to extract and forecast accurately the effective dynamics (LED) of complex systems with multiple spatio-temporal scales. The framework fuses advanced machine learning algorithms with equation-free approaches. It deploys autoencoders to obtain a mapping between fine and coarse grained representations of the system and learns to forecast the latent space dynamics using recurrent neural networks. We compare the LED framework with existing approaches on a number of benchmark problems and demonstrate reduction in computational efforts by several orders of magnitude without sacrificing the accuracy of the system.

**Keywords** Multiscale modeling · Equation-free · Autoencoders

## 1 Introduction

A wide range of scientific problems and engineering designs is founded on the study of complex systems with dynamics spanning multiple spatio-temporal scales. Examples include protein dynamics [1], turbulence [2], brain [3] and cancer dynamics [4], climate [5], ocean dynamics [6] and social systems [7]. Over the last fifty years, simulations have become a key component of these studies thanks to a confluence of advances in computing architectures, numerical methods and software. Large scale simulations have led to unprecedented insight, acting as in-silico microscopes [8] or telescopes to reveal the dynamics of galaxy formations [9]. At the same time these simulations have led to the understanding that resolving the full range of spatio-temporal scales in such complex systems will remain out of reach in the foreseeable future.

In recent years there have been intense efforts to develop efficient simulations that exploit the multiscale character of the systems under investigation [10, 11, 12, 13, 14, 15]. Multiscale methods rely on judicious approximations

---

\*To whom correspondence should be addressed. E-mail: petros@ethz.ch

of the interactions between processes occurring over different scales and a number of potent frameworks have been proposed including the equation-free framework (EFF) [13, 16, 11, 17, 18], the Heterogeneous Multiscale Method (HMM) [12, 19, 20] and the FLOW AVERAGED INTEGRATOR (FLAVOR) [21, 22]. In these algorithms the system dynamics are distinguished into fine and coarse scales or expensive and affordable simulations respectively. Their success depends on the separation of scales that are inherent to the system dynamics and their capability to capture the transfer of information between scales. Effective applications of multiscale methodologies minimize the computational effort while maximizing the accuracy of the propagated dynamics. The EFF relies on few fine scale simulations that are used to acquire, through “restricting”, information about the evolution of the coarse grained quantities of interest. In turn various time stepping procedures are used to propagate the coarse grained dynamics. The fine scale dynamics are obtained by judiciously “lifting” the coarse scales to return to the fine scale description of the system and repeat. When the EFF reproduces trajectories of the original system, the identified low order dynamics represent the intrinsic system dynamics, also called effective dynamics, inertial manifold [23, 24] or slow collective variables [25] or reaction coordinates [26] in molecular kinetics.

While it is undisputed that the EFF, HMM, FLAVOR and related frameworks have revolutionized the field of multiscale modeling and simulation, we identify two critical issues that presently limit their potential. First, the accuracy of propagating the coarse grained dynamics hinges on the employed time integrators. More importantly the choice of information transfer, in particular from coarse to fine scale dynamics in ‘lifting’, greatly affects the forecasting capacity of the methods.

In the present work we resolve these two critical issues through Machine Learning algorithms that (i) deploy state of the art recurrent neural networks (RNNs) with gating mechanisms to evolve the coarse grained (latent) dynamics and (ii) employ advanced probabilistic autoencoders (AEs) to transfer in a systematic, data driven manner, the information between coarse and fine scale descriptions.

Over the last years, machine learning (ML) algorithms have exploited the ample availability of data, and powerful computing architectures [27], to provide us with remarkable successes across scientific disciplines from physics [28, 29, 30, 31], fluid dynamics [32, 33, 34], image and language processing [35], mathematics [36] to medicine [37]. The particular elements of our algorithms have been employed in the modeling of dynamical systems. Autoencoders [38, 39] have been used to identify a linear latent space based on the Koopman framework [40, 41], model high dimensional fluid flows [42, 43] or sample effectively the state space in the kinetics of proteins [44, 45, 46]. Recurrent neural networks with gating mechanisms have been shown successful in capturing the coarse grained dynamics of complex systems [47, 48]. However, these previous works fail to employ one or more of the following mechanisms: consider the coarse scale dynamics, account their non-Markovian or non-linear nature, exploit a probabilistic generative mapping from the coarse to the fine scale, and scale to high dimensional systems. In [49], the authors identify a PDE on a coarse level using diffusion maps, Gaussian processes or neural networks, and utilize forward integration in the coarse representation to model the FitzHugh-Nagumo equation (FHN) in the equation-free formalism.

We find that by augmenting multiscale frameworks (including EFF, HMM, FAVOR) with state of the art Machine Learning algorithms allows for evolving the coarse scale dynamics by taking into account their time history and by providing consistent lifting and restriction operators to transfer information between fine and coarse scales. To the best of our knowledge, this is the first time that machine learning algorithms are exploited in the context of multiscale modeling. We demonstrate that the proposed LED allows for simulations of complex multiscale systems that reduce the computational cost by orders of magnitude, to capture spatiotemporal scales that would be impossible to resolve with existing computing resources.

## 2 Learning the Effective Dynamics (LED)

We propose a learning framework to identify and propagate the effective dynamics of multiscale systems. The proposed learned effective dynamics (LED) allow for an accurate prediction of the evolution of the system at a significant reduced computational cost.

The LED framework is founded on the multiscale framework of Equation Free Methods [11] and the related Heterogeneous Multiscale Methods (HMM) [20] and FLOW AVERAGED INTEGRATORS (FLAVOR) [21] methodologies. LEDs provide a unified description and augment these methods by delivering a consistent transfer of information between coarse and fine grain scales, using AEs, and a non-Markovian advancement of the nonlinear dynamics of the latent space, using RNNs.

In the following, the high dimensional state of a dynamical system is given by  $\mathbf{s}_t \in \mathbb{R}^{d_s}$ , and the discrete time dynamics are given by

$$\mathbf{s}_{t+\Delta t} = \mathbf{F}(\mathbf{s}_t), \quad (1)$$

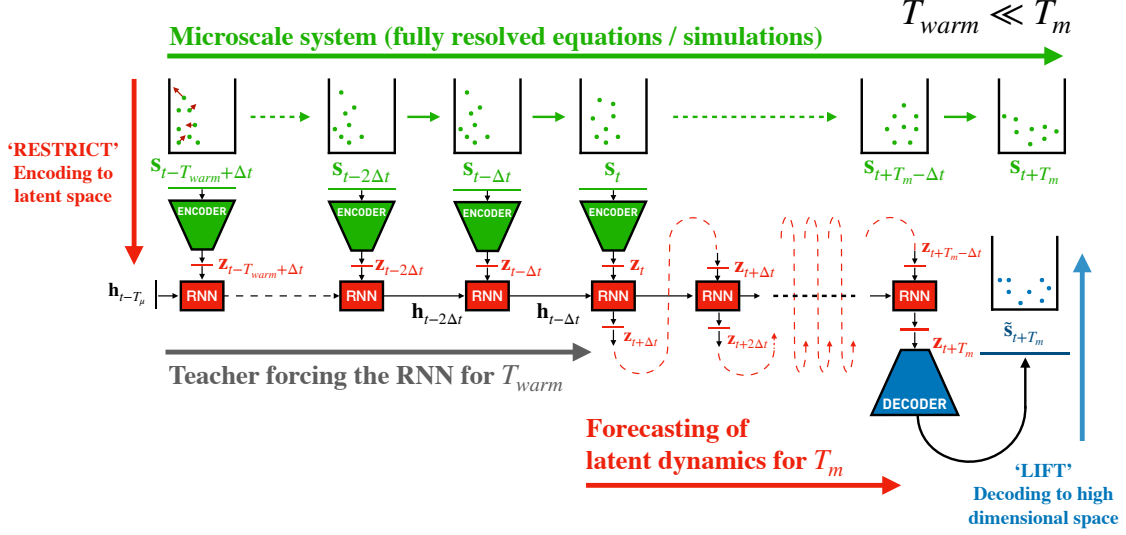


Figure 1: The high dimensional dynamics  $s_t$  are simulated for a short period of  $T_{warm}$  time units. During this warm-up period, the state  $s_t$  is passed through the encoder network. The outputs of the encoder  $z_t$  are iteratively provided as the input to the RNN, allowing for the update of its hidden state  $h_t$  capturing non-Markovian effects. Starting from the last latent state  $z_t$  the RNN iteratively propagates the **low order latent** dynamics up to a total horizon of  $T_m$  time units, with  $T_m \gg T_{warm}$ . The LED decoder maps the last latent state  $z_{t+T_m}$  back to a high-dimensional representation  $\tilde{s}_{t+T_m}$ . Propagation in the low order space unraveled by LED can be orders of magnitude cheaper compared to evolving the high dimensional system based on first principles. As a consequence, LED can accelerate simulations, enabling the study of the dynamics in much longer time scales, and unraveling state space regions that would be otherwise intractable.

where  $\Delta t$  is the sampling period and  $F$  may be nonlinear, deterministic or stochastic. We assume that the dynamics of the system can be described by a few variables, on a low order manifold  $z_t \in \mathbb{R}^{d_z}$ , where  $d_s \gg d_z$ . In order to identify this manifold, we utilize an encoder  $\mathcal{E}^{w_\mathcal{E}} : \mathbb{R}^{d_s} \rightarrow \mathbb{R}^{d_z}$ , where  $w_\mathcal{E}$  are trainable parameters, projecting the high dimensional state to  $z_t = \mathcal{E}^{w_\mathcal{E}}(s_t)$ . In turn, we utilize a decoder that maps back this latent representation to the high dimensional state, i.e.  $\tilde{s}_t = \mathcal{D}^{w_\mathcal{D}}(z_t)$ . Variational AEs regularizing the training of AEs, described in detail in the supplementary information (SI) document are also embedded in LED. For stochastic systems,  $\mathcal{D}^{w_\mathcal{D}}$  is modeled with a Mixture Density (MD) decoder [50], approximating the probability distribution of the state  $\tilde{s}_t \sim p(\cdot; w_{\text{MD}})$ , where  $w_{\text{MD}} = \mathcal{D}^{w_\mathcal{D}}(z_t)$  are the outputs of the decoder, parametrizing the distribution.

The parameters  $w_\mathcal{E}, w_\mathcal{D}$  are identified by maximizing the log-likelihood of the reconstruction,

$$w_\mathcal{E}, w_\mathcal{D} = \underset{w_\mathcal{E}, w_\mathcal{D}}{\operatorname{argmax}} \log p(s_t; w_{\text{MD}}), \quad (2)$$

$$w_{\text{MD}} = \mathcal{D}^{w_\mathcal{D}}(z_t) = \mathcal{D}^{w_\mathcal{D}}(\mathcal{E}^{w_\mathcal{E}}(s_t)). \quad (3)$$

For a deterministic decoder, this loss reduces to the classical reconstruction loss  $\|s_t - \mathcal{D}^{w_\mathcal{D}}(\mathcal{E}^{w_\mathcal{E}}(s_t))\|_2^2$ . Further details on the implementation of the MD decoder are provided in the SI.

As the LEDs are targeting physical systems we take into consideration properties such as energy conservation [51], translation invariance [52], or permutation invariance. Such invariants can be embedded in the proposed multiscale framework. In this work, we demonstrate that LED can be easily coupled with a permutation invariant layer [53] (see details in the SI), and utilized later in the modeling of the dynamics of a large set of particles governed by the advection diffusion equation.

As a non-linear propagator in the low order manifold (coarse scale), we utilize a RNN, capturing non-Markovian, memory effects by keeping an internal memory state. The efficiency of RNNs in capturing non-Markovian temporal dependencies has been demonstrated in complex high-dimensional dynamical systems [48, 47], yet their capabilities in multiscale modeling has not been demonstrated before. The RNN is learning a forecasting rule

$$h_t = \mathcal{H}^{w_\mathcal{H}}(z_t, h_{t-\Delta t}), \quad \tilde{z}_{t+\Delta t} = \mathcal{R}^{w_\mathcal{R}}(h_t), \quad (4)$$

where  $h_t \in \mathbb{R}^{d_h}$  is an internal hidden memory state, and  $\tilde{z}_{t+\Delta t}$  is a prediction of the latent state.

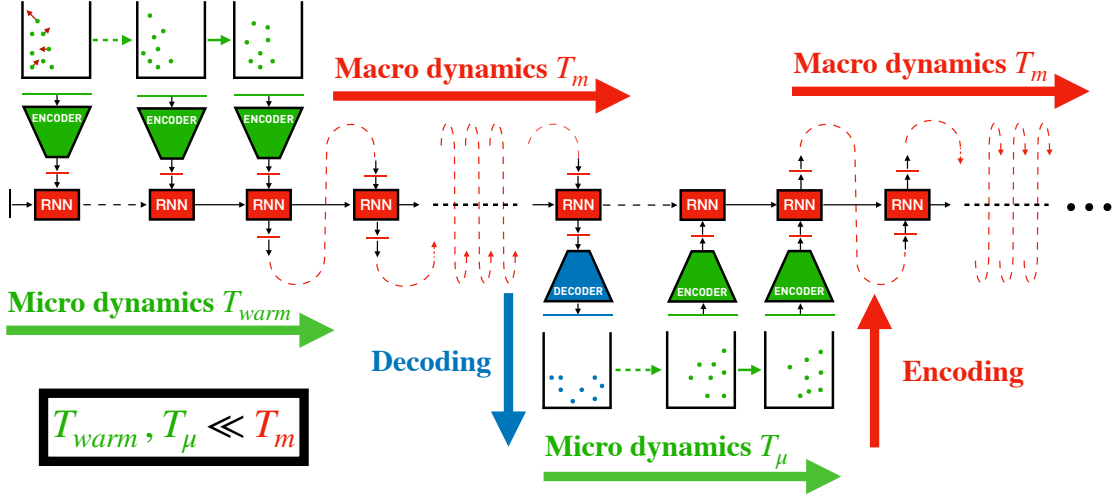


Figure 2: Multiscale forecasting with LED (**testing phase**). Starting from an initial condition in the test data, use the **equations/first principles** to evolve the dynamics for  $T_{warm}$ , project to the latent space dynamics using the autoencoder, and teacher force the RNN to warm up the hidden state for this initial time  $T_{warm}$ . Next, **iteratively (1)** propagate the dynamics on the low-dimensional latent space with the RNN for  $T_m$  time units, **(2)** project the latent dynamics at  $t = T_m$  back to the high dimensional state, **(3)** starting from this high-dimensional state as an initial condition, use the **equations/first principles** to evolve the dynamics for  $T_\mu$ , and so on and so forth.

The role of the RNN is twofold. First, it is updating its hidden memory state  $\mathbf{h}_t$ , given the current state provided at the input  $\mathbf{z}_t$  and the hidden memory state at the previous time-step  $\mathbf{h}_{t-\Delta t}$ , tracking the history of the low order state to model non-Markovian dynamics. Second, given the updated hidden state  $\mathbf{h}_t$  the RNN forecasts the latent state at the next time-step(s)  $\tilde{\mathbf{z}}_{t+\Delta t}$ .  $\mathcal{H}^{w_{\mathcal{H}}}$  and  $\mathcal{R}^{w_{\mathcal{R}}}$  are the hidden-to-hidden mapping, and the hidden-to-output mappings, while  $w_{\mathcal{H}}$  and  $w_{\mathcal{R}}$  are the trainable parameters of the RNN. Possible implementations of  $\mathcal{H}^{w_{\mathcal{H}}}$  and  $\mathcal{R}^{w_{\mathcal{R}}}$  are the long short-term memory (LSTM) [54] cell or the Gated Recurrent Unit (GRU) [55], explained in the SI. The RNN is trained to minimize the forecasting loss  $\|\tilde{\mathbf{z}}_{t+\Delta t} - \mathbf{z}_{t+\Delta t}\|_2^2$  by backpropagation through time (BPTT) [56].

Firstly, the RNN and the autoencoder, jointly referred to as learned effective dynamics (LED), are trained on data from short simulations of the fully resolved (or microscale) dynamical system. After training, LED is employed to forecast the dynamics on unseen data, by propagating the low order latent state with the RNN and avoiding the computationally expensive simulation of high-dimensional dynamics, as depicted in Figure 1.

The LED framework allows for data driven information transfer between coarse and fine scales through the AEs. Moreover it propagates the latent space dynamics without the need to upscale back to the high-dimensional state space at every time-step. The interface with the high dimensional state space is enabled only at the time-steps and scales of interest. This is in contrast to [45, 46], and is easily adaptable to the needs of particular applications thus augmenting the arsenal of models developed for multiscale problems. We note that, as is the case for any approximate iterative integrator (here the RNN), the initial model errors will propagate. In order to mitigate potential instabilities, we propose the multiscale forecasting scheme in Figure 2. In this way, the approximation error can be reduced at the cost of the computational complexity associated with evolving the high dimensional dynamics. We note that, training of LED models is performed with the Adam stochastic optimization method [57]. All LED models are implemented in Pytorch, mapped to a single Nvidia Tesla P100 GPU and executed on the XC50 compute nodes of the Piz Daint supercomputer at the Swiss national supercomputing centre (CSCS).

### 3 Results

We demonstrate the application of LED in a number of benchmark problems and compare its performance with existing state of the art algorithms.

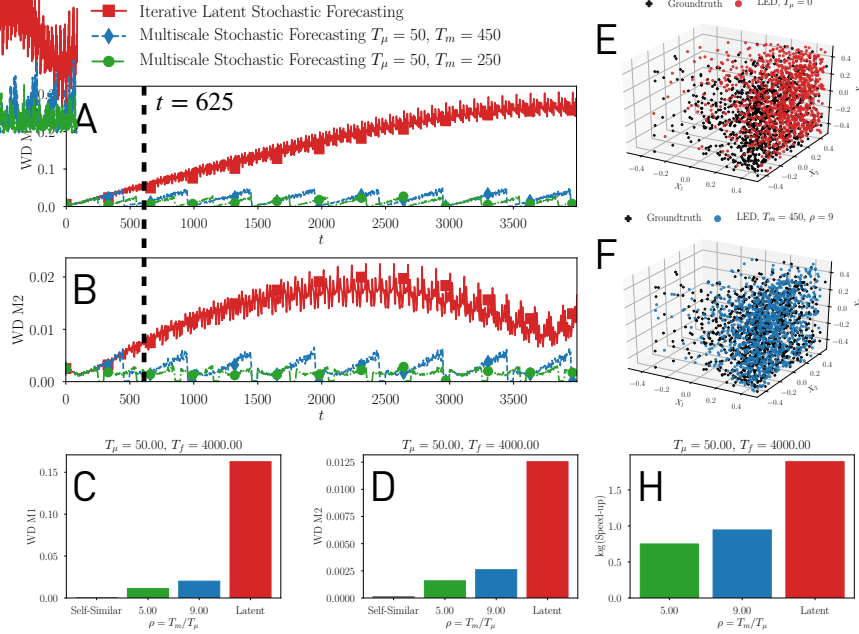


Figure 3: Starting from 12 different initial conditions on the test data, we propagate the dynamics with LED restarting from each initial condition 600 different times (changing the random seed in each restart), up to a final time of  $T_f = 4000$ . For every run, we calculate the first two moments of the distribution of the particle positions, M1 and M2. At each time-step, we have 600 predicted M1 and M2. Three LED variants are considered, LED with  $T_m = 0$  (iterative latent propagation), and two variants with  $T_\mu = 50, T_m = 450$ , and  $T_\mu = 50, T_m = 250$ . The warm-up time is  $T_{warm} = 60$  for all variants. **A,B**) The evolution of the Wasserstein distance (WD) between the predicted distributions of M1/M2 and the groundtruth, averaged over the initial conditions. **C,D**) The Wasserstein distance in M1/M2 averaged over initial conditions and time. LED variants capture the variance (M2) accurately, with relatively low errors on M1 (compared with the domain size  $L = 1$ ). The self-similar error is plotted for reference [58] as errors below this level are statistically insignificant. **E,F**) Examples of predicted particle positions at  $t = 625$  from a single run starting from the same initial condition on the test data for each model. In the SI we provide additional results on the L1-histogram distance, and the evolution of the L1-histogram distance and the WD on the particle positions on single random runs, supporting the aforementioned arguments. **H**) The speed-up of LED compared to the micro scale solver is plotted w.r.t.  $\rho$ .

### 3.1 LED for Advection-Diffusion Equation

We apply the LED method to the simulation of the advection-diffusion equation. We model the microscale description of the Advection-Diffusion (AD) process with a system of  $N = 1000$  particles on a bounded domain  $\Omega = [-L/2, L/2]^{d_x}$ . The particle dynamics are modeled with the stochastic differential equation (SDE)

$$d\mathbf{x}_t = \mathbf{u}_t dt + \sqrt{D} d\mathbf{W}_t, \quad (5)$$

where  $\mathbf{x}_t \in \Omega$  denotes the position of the particle at time  $t$ ,  $D \in \mathbb{R}$  is the diffusion coefficient,  $d\mathbf{W}_t \in \mathbb{R}^{d_x}$  is a Wiener process, and  $\mathbf{u}_t = \mathbf{A} \cos(\omega t) \in \mathbb{R}^{d_x}$  is a cosine advection (drift) term. In the following, we consider the three dimensional space  $d_x = 3$  with  $D = 0.2$ ,  $\mathbf{A} = [1, 1.5, 0.0]^T$  and  $\omega = [0.2, 1.0, 0.5]^T$  and a domain size of  $L = 1$ . We report the Péclet number  $Pe = 9$  quantifying the rate of advection by the rate of diffusion, i.e.

$$Pe = \frac{LU}{D}, \quad (6)$$

where  $L = 1$ ,  $U = |\mathbf{A}|_2 \approx 1.8$ . Equation (5) is solved with explicit Euler integration with  $\Delta t = 10^{-3}$ , initial conditions  $\mathbf{x}_0 = \mathbf{0}$ , and reflective boundary conditions ensuring that  $\mathbf{x}_t \in \Omega, \forall t$ . The positions of the particles are saved at a coarser time-step  $\Delta t = 0.5$  and by starting from randomly selected initial conditions, we generate three datasets. The training and validation datasets consist of  $10^3$  samples each, and the test dataset consists of  $10^4$  samples. The full state of the system is high dimensional, i.e.  $\mathbf{s}_t = [\mathbf{x}_t^1; \dots; \mathbf{x}_t^N]^T \in \mathbb{R}^{N \times 3}$ . We find that the particles concentrate on a few “meta-stable” states, and jump between them, suggesting that the collective dynamics can be captured by a few

latent variables. However, it is not straightforward to determine a-priori the number of these states and the patterns of collective motion. LED unravels this information and provides a computationally efficient multiscale model to approximate the system dynamics. We employ an AE with a permutation invariant input layer (see SI) with a latent dimension  $d_z = 8$ , a MD decoder and a stateful LSTM-RNN to learn and forecast the dynamics on the low-dimensional manifold. The network is fed an initial configuration of particles  $s_t \in \mathbb{R}^{N \times 3}$ , compresses the configuration to the latent state  $z_t \in \mathbb{R}^8$ , and utilizes the RNN to forecast the latent dynamics  $z_{t+1}$ . From this latent space, the MD decoder of LED is sampling the next configuration  $s_{t+1}$ . After training the RNN, we evaluate the efficiency of LED to capture the statistics of the system Figure 3.

In the testing phase, we examine two variants of LED. The first variant does not evolve the dynamics on the particle level (we denote it as ‘‘Latent’’ LED) and its error increases with time and exhibits the highest errors on average. The second variant, (we denote it as ‘‘multiscale’’ LED), evolves the low order manifold dynamics (coarse scale) for  $T_m$  time units, and the particle dynamics (fine scale) for  $T_\mu = 50$  and corrects iteratively for the statistical error. This effect is due to the explicit dependence of the coarse system dynamics in time, as the  $\cos(\omega t)$  advection term dominates. Two values for  $T_m$  are considered,  $T_m = 250$  leading to a relative ratio of coarse to fine simulation time of  $\rho = T_m/T_\mu = 5$ , and another one with  $T_m = 450$ , leading to  $\rho = 9$ . This incurs additional computational cost induced by the evolution of the high dimensional state. As the multiscale ratio  $\rho = T_m/T_\mu$  is increased, spending more time in the latent propagation, the errors gradually increase. We note that the propagation in the low dimensional latent space is far less computationally expensive compared to the evolution of the high dimensional dynamics. As we increase  $\rho$ , we can achieve greater computational savings, albeit at the cost of higher approximation error, as depicted in Figure 3. We demonstrate that the LED is able to generalize to different numbers of particles and provide additional results on the one-dimensional AD case in the SI. The effectiveness of LED depending on the diffusion coefficient  $D$  is shown in Figure 5.

Moreover, in Figure 4, it is shown that by clustering the latent space dynamics, identified by LED, we can gain insight on the collective high dimensional dynamics of the system.

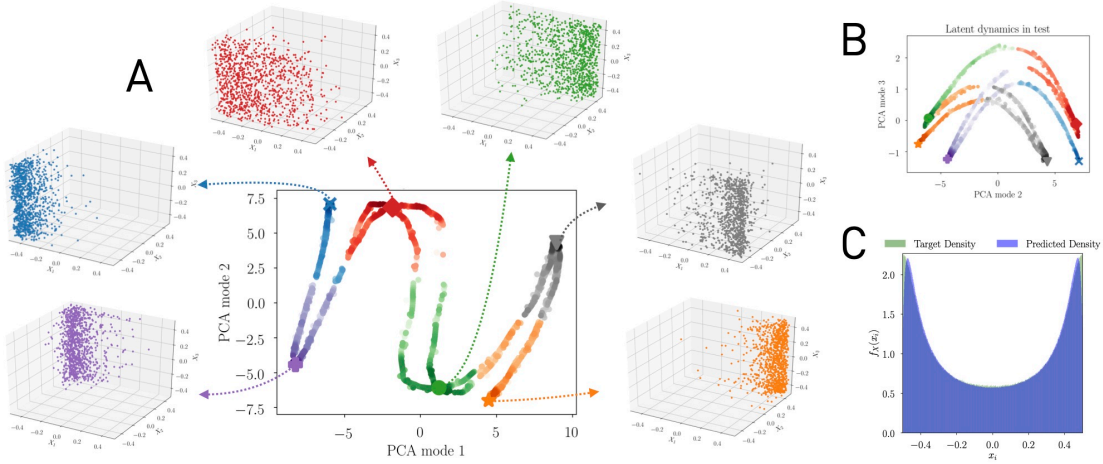


Figure 4: **A)** Evolution of the second PCA mode of the latent state  $z_t \in \mathbb{R}^{d_z=8}$ , against the first mode. Higher color intensity denotes higher density. Six high density regions are identified. We perform spectral clustering on the PCA modes of the latent dynamics. The six identified cluster centers are marked, while color illustrates the cluster membership. The LED probabilistic decoder is employed to map each cluster center to a realization of a high-dimensional simulation state. LED effectively unravels six meta stable states of the Advection-Diffusion equation, along with the transitions between them, representing the low order effective dynamics. **B)** Evolution of the third PCA mode against the second one, colored according to cluster assignment. **C)** Density of the particle positions from simulation plotted against the distribution of the positions predicted by LED. We remark the good agreement between the two distributions.

### 3.2 FitzHugh-Nagumo Model (FHN)

We examine the capability of LED to capture the evolution of the FitzHugh-Nagumo [59, 60] equations (FHN). The FHN model describes the evolution of an inhibitor  $u(x, t) = \rho^{ac}(x, t)$  and an activator density  $v(x, t) = \rho^{in}(x, t)$  on

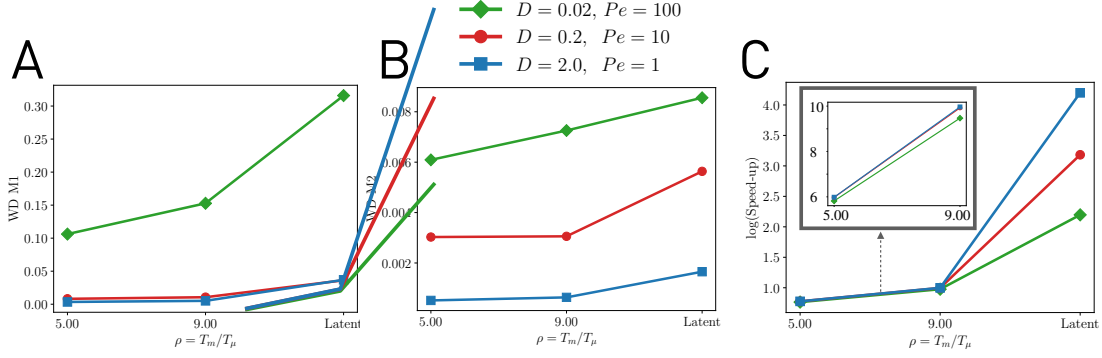


Figure 5: Analysis of the performance of LED for different Péclet numbers  $Pe \in \{100, 10, 1\}$ . To measure the errors, we perform 400 runs, starting a random initial condition, up to final time  $T_f = 3000$ . **A, B**) WD on the distributions of the first two moments between the micro scale simulation and LED. The methods consistently exhibit lower error as the Péclet number decreases. **C**) The speed-up is plotted w.r.t.  $\rho$ . Simulation of micro dynamics for lower Péclet numbers is more expensive, due to the lower time-step necessary to resolve the diffusive dynamics. As  $Pe$  decreases, the computational savings of LED increase by orders of magnitude (see the SI for further details).

the domain  $x \in [0, L]$ :

$$\begin{aligned} \frac{\partial u}{\partial t} &= D^u \frac{\partial^2 u}{\partial x^2} + u - u^3 - v, \\ \frac{\partial v}{\partial t} &= D^v \frac{\partial^2 v}{\partial x^2} + \epsilon(u - \alpha_1 v - \alpha_0). \end{aligned} \quad (7)$$

The system evolves under two timescales, with the activator/inhibitor density acting as the “fast”/“slow” variable respectively. The bifurcation parameter  $\epsilon = 0.006$  controls the difference in the time-scales. We set  $D^u = 1$  and  $D^v = 4$  the diffusion coefficients of the activator and the inhibitor, respectively, and select  $L = 20$ ,  $\alpha_0 = -0.03$  and  $\alpha_1 = 2$ .

Equation (7) is discretized with  $N = 101$  grid points and solved using the Lattice Boltzmann (LB) method [61], with time-step  $\Delta t = 0.005$ . In the following, the mesoscopic solution obtained by LB is considered the fine-grained solution. LED is operating on a coarser time-scale  $\Delta t = 1$ , and a coarse latent scale  $d_z = 8$  (increasing the latent scale further did not lead to lower reconstruction error of the LED autoencoder as reported in the SI). In this case, LED is not utilizing a MD decoder, as the system under study is deterministic. LED is benchmarked against equation free variants [49] in the FHN equation in Figure 6.

LED identifies and propagates the low order intrinsic dynamics, and is able to up-scale back to the activator density, forecasting its evolution accurately, while being  $S = T^{\text{LED}}/T^{\text{fine}} \approx 10^2$  times faster, where  $T^{\text{LED}}$  is the average time that LED takes for one step of size  $\Delta t$  time units, and  $T^{\text{fine}}$  is the average time the LB solver takes for one coarse time unit  $\Delta t = 1$ . This speed-up can be decisive in accelerating simulations and achieving much larger time horizons. Using the multiscale propagation (iteratively exchanging between the coarse-grained dynamics of LED and using the solver on the fine-scale), the approximation error of LED decreases, at the cost of reduced speed-up. This interplay can be seen in Figure 7. The warm-up time is  $T_{\text{warm}} = 60$  for all variants.

### 3.3 Kuramoto-Sivashinsky

The Kuramoto-Sivashinsky (KS) is a prototypical spatially partial differential equation (PDE) of fourth order that exhibits a very rich range of nonlinear phenomena [62]. We examine the capability of LED to learn the low order manifold of the effective dynamics in KS [63, 64]. Even though PDEs, such as the KS modeling viscous flows, are infinite dimensional, in case of high dissipation and small spatial extent, the long-term dynamics can be represented on a low dimensional inertial manifold [24, 23], that attracts all neighboring states at an exponential rate after a transient period.

We consider the one dimensional K-S equation given by the PDE

$$\frac{\partial u}{\partial t} = -\nu \frac{\partial^4 u}{\partial x^4} - \frac{\partial^2 u}{\partial x^2} - u \frac{\partial u}{\partial x}, \quad (8)$$

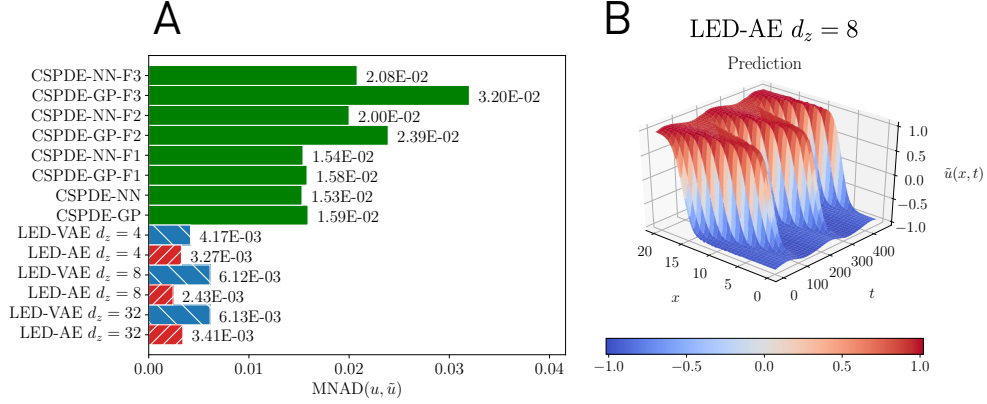


Figure 6: Comparison of LED with equation-free variants [49] that are based on the identification of PDEs on the coarse level (CSPDE), in forecasting the dynamics of the FHN equation starting from an initial condition from the test data up to final time  $T_f = 451$ . CSPDE variants are utilizing Gaussian processes (GP) or neural networks (NN), features of the fine scale dynamics obtained through diffusion maps (F1 to F3) and forward integration to propagate the coarse representation in time. **A**) Mean normalised absolute difference (MNAD) on the activator density, between the result of the LB simulation  $u(x, t)$  considered as groundtruth and the model forecasts  $\hat{u}$ , either LED or CSPDE variants. Variants of LED with autoencoders (AE), variational autoencoders (VAE), and different sizes of the latent dimension (LD) are considered, to evaluate the sensitivity of the performance on these parameters. LED outperform CSPDE variants by an order of magnitude. The definition of the MNAD, and additional results on the inhibitor density are given in the SI. **B**) Prediction of the dynamics of the activator density of the FHN equation on the test dataset using LED with a coarse dimension  $d_z = 8$ .

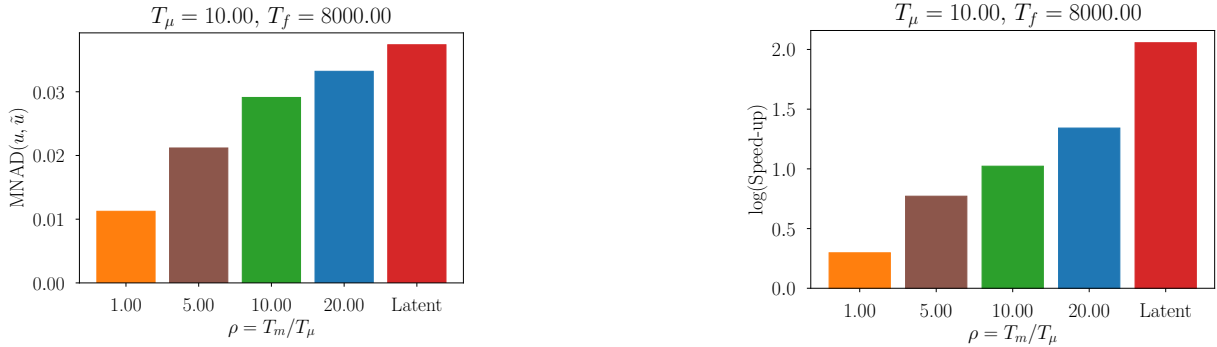


Figure 7: Starting from 100 different initial conditions in the test data, the LB method is utilized to compute the FHN dynamics up to a large horizon  $T_f = 8000$ , approximately 16 times larger than the training data. Using the LED framework, either with full iterative propagation on the reduced order space ( $T_\mu = 0$ ), or alternating between macro-dynamics for  $T_m = 10$  and high-dimensional dynamics for  $T_\mu$ , we approximate the evolution. The results for  $T_\mu = 0$  are denoted with the label “Latent”. The warm-up period is set to  $T_{warm} = 75$ . **(a)** The average MNAD error between the predicted and ground-truth evolution of the activator density is plotted as a function of the macro-to-micro ratio  $\rho = T_m/T_\mu$ . **(b)** The speed-up compared to the LB solver is plotted w.r.t.  $\rho$ . For  $T_m = T_\mu = 10$  ( $\rho = 1$ ), we observe that the MNAD is reduced from  $\approx 0.04$ , to  $\approx 0.01$  compared to the iterative latent propagation. However, the speed-up is reduced from  $S \approx 10^2$  to  $S \approx 2$ . By increasing  $T_m \in \{50, 100, 200\}$ , we get the intermediate regimes between propagation of the computationally expensive (and possibly intractable) high-dimensional system dynamics, and the fully latent propagation. As we increase  $T_m$  (increase  $\rho$ ), the speed-up is increased, as we are using more and more the reduced order dynamics, albeit at the cost of an increasing error.

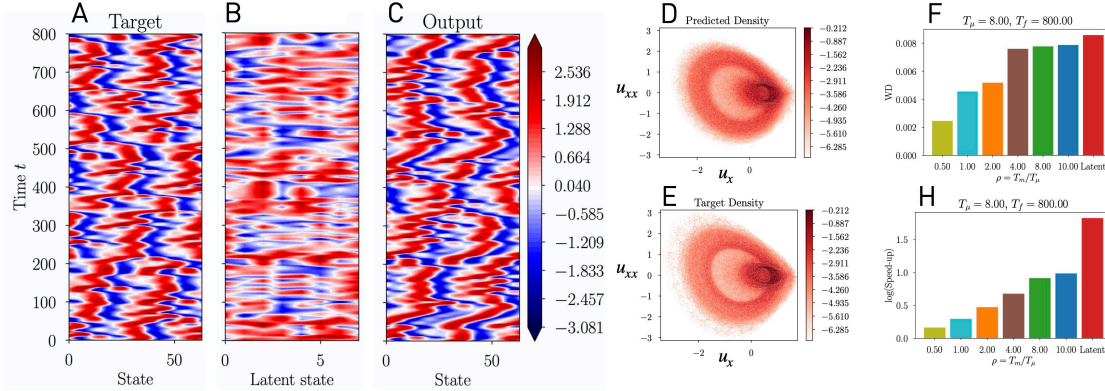


Figure 8: A) Contour plot of the KS dynamics starting from an initial condition from the test data. B) The evolution of the  $d_z = 8$  dimensional latent state of LED. C) The predicted field by LED iteratively propagating the dynamics on a  $d_z = 8$  dimensional latent space, after a warm-up period  $T_{warm} = 60$  ( $T_\mu = 0$ ). D) The density of values in the  $u_x - u_{xx}$  space from the predicted trajectory matches closely the E) ground-truth, illustrating that the LED is able to mimic characteristics of the dynamical system, even though propagating coarse dynamics. F) The statistical error (WD) on the distribution of state values for different variants of LED w.r.t.  $\rho$ . The errors remain small, demonstrating that the LED is capturing the long-term statistics (climate). H) The speed-up of LED w.r.t.  $\rho$ . Evolution of the latent state of LED ( $T_\mu = 0$ ) is approximately two orders of magnitude cheaper than the micro scale dynamics. (Quantitative results on the power spectrum and extensive analysis is provided in the SI)

on the domain  $\Omega = [0, L]$  with periodic boundary conditions  $u(0, t) = u(L, t)$  and  $\nu = 1$ . In this work, we consider the case  $L = 22$  studied extensively in [65] exhibiting a structurally stable chaotic attractor, i.e. an inertial manifold where the long-term dynamics lie. We discretize Equation (8) with a grid of size  $D = 64$ , and solve it using the fourth-order method for stiff PDEs introduced in [66] with a time-step of  $\Delta t = 0.025$  starting from a random initial condition, and keeping every tenth datapoint, to obtain a dataset where samples are distanced by  $\Delta t = 0.25$  in time.

We use  $5 \cdot 10^3$  such samples for training and another  $5 \cdot 10^3$  for validation. For testing purposes (long-term forecasting), we repeat the process with a different random seed, generating another  $10^5$  samples. The results of LED in KS are shown in Figure 8.

## 4 Discussion

We have presented a novel framework for learning the effective dynamics (LED) and accelerate the simulations of multiscale stochastic and deterministic dynamical systems. Our work relies on augmenting the equation-free formalism with state of the art deep learning methods.

We have tested the LED framework on a number of benchmark problems. We find that in systems where evolving the high dimensional state dynamics based on first principles (solvers, equations, etc.) is computationally expensive, LED can accelerate the simulation by propagating on the latent space and upscaling to the high-dimensional system state with the probabilistic generative mixture density decoder, only at the time scales of interest.

The efficiency of LED was evaluated in unraveling and forecasting the stochastic collective dynamics of 1000 particles following Brownian motion subject to advection and diffusion in the three dimensional space, forecasting the FitzHugh-Nagumo equation dynamics achieving an order of magnitude lower approximation error compared to other state of the art equation-free based approaches while being two orders of magnitude faster than the Lattice Boltzmann solver, and identifying the effective dynamics of the Kuramoto-Sivashinsky equation with  $L = 22$ , achieving accurate short term prediction while capturing of the long-term behavior (climate), even though LED is propagating the dynamics on the coarse latent state, achieving a speed-up of  $S \approx 80$ . We note that the present method is readily applicable to all problems where Equation Free, HMM and FLAVOR methodologies have been applied.

In summary, LED identifies and propagates the effective dynamics of dynamical systems with multiple spatiotemporal scales providing significant computational savings. Moreover, LED provides a systematic way of trading between speed-up and accuracy for a multiscale system by switching between propagation of the latent dynamics, and evolution of the original equations, iteratively correcting the statistical error at the cost of reduced speed-up. The present methodology can be deployed both in problems described by first principles as well as for problems where only data are

available for either the macro or microscale descriptions of the system. Finally, by providing a bridge between data driven and first principles models LEDs open new horizons for the effective simulations of complex multiscale systems.

## Contributions & Acknowledgments

P.K. conceived the project; P.R.V., G.A., C.U., and P.K. designed and performed research; P.R.V., and G.A. contributed new analytic tools; P.R.V., G.A., and P.K. analyzed data; and P.R.V., G.A., and P.K. wrote the paper.

The authors declare no conflict of interest.

We would like to thank Nikolaos Kallikounis for helpful discussions on the Lattice Boltzmann method, and Kostas Spiliotis, Joon Lee, and Yannis Kevrekidis for providing code to reproduce the data for the FHN equation. We are also thankful to the Swiss National Supercomputing Centre (CSCS) providing the necessary computational resources under Projects s929.

## References

- [1] Thomas CB McLeish, TL Rodgers, and Mark R Wilson. Allosterity without conformation change: modelling protein dynamics at multiple scales. *Physical biology*, 10(5):056004, 2013.
- [2] David C Wilcox. Multiscale model for turbulent flows. *AIAA journal*, 26(11):1311–1320, 1988.
- [3] Salvador Dura-Bernal, Benjamin A Suter, Pdraig Gleeson, Matteo Cantarelli, Adrian Quintana, Facundo Rodriguez, David J Kedziora, George L Chadderdon, Cliff C Kerr, Samuel A Neymotin, et al. Netpyne, a tool for data-driven multiscale modeling of brain circuits. *Elife*, 8:e44494, 2019.
- [4] Thomas S Deisboeck and Georgios S Stamatakos. *Multiscale cancer modeling*. CRC press, 2010.
- [5] National Research Council. *A National Strategy for Advancing Climate Modeling*. The National Academies Press, 2012.
- [6] Amala Mahadevan. The impact of submesoscale physics on primary productivity of plankton. *Annual review of marine science*, 8:161–184, 2016.
- [7] Nicola Bellomo and Christian Dogbe. On the modeling of traffic and crowds: A survey of models, speculations, and perspectives. *SIAM review*, 53(3):409–463, 2011.
- [8] Eric H Lee, Jen Hsin, Marcos Sotomayor, Gemma Comellas, and Klaus Schulten. Discovery through the computational microscope. *Structure*, 17(10):1295–1306, 2009.
- [9] Volker Springel, Simon DM White, Adrian Jenkins, Carlos S Frenk, Naoki Yoshida, Liang Gao, Julio Navarro, Robert Thacker, Darren Croton, John Helly, et al. Simulations of the formation, evolution and clustering of galaxies and quasars. *nature*, 435(7042):629–636, 2005.
- [10] Richard Car and Mark Parrinello. Unified approach for molecular dynamics and density-functional theory. *Physical review letters*, 55(22):2471, 1985.
- [11] Ioannis G Kevrekidis, C William Gear, James M Hyman, Panagiotis G Kevrekidid, Olof Runborg, Constantinos Theodoropoulos, et al. Equation-free, coarse-grained multiscale computation: Enabling microscopic simulators to perform system-level analysis. *Communications in Mathematical Sciences*, 1(4):715–762, 2003.
- [12] E Weinan, Bjorn Engquist, et al. The heterogenous multiscale methods. *Communications in Mathematical Sciences*, 1(1):87–132, 2003.
- [13] Ioannis G Kevrekidis, C William Gear, and Gerhard Hummer. Equation-free: The computer-aided analysis of complex multiscale systems. *AICHE Journal*, 50(7):1346–1355, 2004.
- [14] Radek Erban, Ioannis G Kevrekidis, David Adalsteinsson, and Timothy C Elston. Gene regulatory networks: A coarse-grained, equation-free approach to multiscale computation. *The Journal of chemical physics*, 124(8):084106, 2006.
- [15] Sabine Attinger, Petros D Koumoutsakos, and Summer Program in Multi-Scale. *Multiscale modelling and simulation*. Springer, 2004.
- [16] Ioannis G Kevrekidis and Giovanni Samaey. Equation-free multiscale computation: Algorithms and applications. *Annual review of physical chemistry*, 60:321–344, 2009.
- [17] Carlo R Laing, Thomas Frewen, and Ioannis G Kevrekidis. Reduced models for binocular rivalry. *Journal of computational neuroscience*, 28(3):459–476, 2010.

- [18] Yohai Bar-Sinai, Stephan Hoyer, Jason Hickey, and Michael P Brenner. Learning data-driven discretizations for partial differential equations. *Proceedings of the National Academy of Sciences*, 116(31):15344–15349, 2019.
- [19] E. Weinan, Xiantao Li, and Eric Vanden-Eijnden. Some recent progress in multiscale modeling. In Sabine Attinger and Petros Koumoutsakos, editors, *Multiscale Modelling and Simulation*, pages 3–21, Berlin, Heidelberg, 2004. Springer Berlin Heidelberg.
- [20] E Weinan, Bjorn Engquist, Xiantao Li, Weiqing Ren, and Eric Vanden-Eijnden. Heterogeneous multiscale methods: a review. *Communications in computational physics*, 2(3):367–450, 2007.
- [21] Molei Tao, Houman Owhadi, and Jerrold E Marsden. Nonintrusive and structure preserving multiscale integration of stiff odes, sdes, and hamiltonian systems with hidden slow dynamics via flow averaging. *Multiscale Modeling & Simulation*, 8(4):1269–1324, 2010.
- [22] Molei Tao, Houman Owhadi, and Jerrold E. Marsden. Space-time FLAVORS: finite difference, multisymplectic, and pseudospectral integrators for multiscale PDEs. *Dynamics of Partial Differential Equations*, 8(1):21–45, MAR 2011.
- [23] Alec J Linot and Michael D Graham. Deep learning to discover and predict dynamics on an inertial manifold. *Physical Review E*, 101(6):062209, 2020.
- [24] James C Robinson. Inertial manifolds for the kuramoto-sivashinsky equation. *Physics Letters A*, 184(2):190–193, 1994.
- [25] Giacomo Fiorin, Michael L Klein, and Jérôme Héning. Using collective variables to drive molecular dynamics simulations. *Molecular Physics*, 111(22-23):3345–3362, 2013.
- [26] Robert B Best and Gerhard Hummer. Reaction coordinates and rates from transition paths. *Proceedings of the National Academy of Sciences*, 102(19):6732–6737, 2005.
- [27] Thorsten Kurth, Sean Treichler, Joshua Romero, Mayur Mudigonda, Nathan Luehr, Everett Phillips, Ankur Mahesh, Michael Matheson, Jack Deslippe, Massimiliano Fatica, et al. Exascale deep learning for climate analytics. In *SC18: International Conference for High Performance Computing, Networking, Storage and Analysis*, pages 649–660. IEEE, 2018.
- [28] Kathleen P Champion, Steven L Brunton, and J Nathan Kutz. Discovery of nonlinear multiscale systems: Sampling strategies and embeddings. *SIAM Journal on Applied Dynamical Systems*, 18(1):312–333, 2019.
- [29] Zhong Yi Wan and Themistoklis P Sapsis. Machine learning the kinematics of spherical particles in fluid flows. *Journal of Fluid Mechanics*, 857, 2018.
- [30] Guido Novati, Lakshminarayanan Mahadevan, and Petros Koumoutsakos. Controlled gliding and perching through deep-reinforcement-learning. *Physical Review Fluids*, 4(9):093902, 2019.
- [31] Zhong Yi Wan, Pantelis Vlachas, Petros Koumoutsakos, and Themistoklis Sapsis. Data-assisted reduced-order modeling of extreme events in complex dynamical systems. *PloS one*, 13(5):e0197704, 2018.
- [32] Steven L Brunton, Bernd R Noack, and Petros Koumoutsakos. Machine learning for fluid mechanics. *Annual Review of Fluid Mechanics*, 52, 2019.
- [33] Steven L Brunton, Joshua L Proctor, and J Nathan Kutz. Discovering governing equations from data by sparse identification of nonlinear dynamical systems. *Proceedings of the National Academy of Sciences*, 113(15):3932–3937, 2016.
- [34] Siddhartha Verma, Guido Novati, and Petros Koumoutsakos. Efficient collective swimming by harnessing vortices through deep reinforcement learning. *Proceedings of the National Academy of Sciences*, 115(23):5849–5854, 2018.
- [35] Jeffrey Pennington, Richard Socher, and Christopher Manning. Glove: Global vectors for word representation. In *Proceedings of the 2014 conference on empirical methods in natural language processing (EMNLP)*, pages 1532–1543, 2014.
- [36] Jiequn Han, Arnulf Jentzen, and E Weinan. Solving high-dimensional partial differential equations using deep learning. *Proceedings of the National Academy of Sciences*, 115(34):8505–8510, 2018.
- [37] Eric J Topol. High-performance medicine: the convergence of human and artificial intelligence. *Nature medicine*, 25(1):44–56, 2019.
- [38] Mark A Kramer. Nonlinear principal component analysis using autoassociative neural networks. *AICHE journal*, 37(2):233–243, 1991.
- [39] Diederik P Kingma and Max Welling. Auto-encoding variational bayes. *arXiv preprint arXiv:1312.6114*, 2013.

- [40] Bethany Lusch, J Nathan Kutz, and Steven L Brunton. Deep learning for universal linear embeddings of nonlinear dynamics. *Nature communications*, 9(1):1–10, 2018.
- [41] Samuel E Otto and Clarence W Rowley. Linearly recurrent autoencoder networks for learning dynamics. *SIAM Journal on Applied Dynamical Systems*, 18(1):558–593, 2019.
- [42] Nicholas Geneva and Nicholas Zabaras. Modeling the dynamics of pde systems with physics-constrained deep auto-regressive networks. *Journal of Computational Physics*, 403:109056, 2020.
- [43] Michele Milano and Petros Koumoutsakos. Neural network modeling for near wall turbulent flow. *Journal of Computational Physics*, 182(1):1–26, 2002.
- [44] Christoph Wehmeyer and Frank Noé. Time-lagged autoencoders: Deep learning of slow collective variables for molecular kinetics. *The Journal of chemical physics*, 148(24):241703, 2018.
- [45] Carlos X Hernández, Hannah K Wayment-Steele, Mohammad M Sultan, Brooke E Husic, and Vijay S Pande. Variational encoding of complex dynamics. *Physical Review E*, 97(6):062412, 2018.
- [46] Mohammad M Sultan, Hannah K Wayment-Steele, and Vijay S Pande. Transferable neural networks for enhanced sampling of protein dynamics. *Journal of chemical theory and computation*, 14(4):1887–1894, 2018.
- [47] Pantelis R Vlachas, Wonmin Byeon, Zhong Y Wan, Themistoklis P Sapsis, and Petros Koumoutsakos. Data-driven forecasting of high-dimensional chaotic systems with long short-term memory networks. *Proceedings of the Royal Society A: Mathematical, Physical and Engineering Sciences*, 474(2213):20170844, 2018.
- [48] Pantelis R Vlachas, Jaideep Pathak, Brian R Hunt, Themistoklis P Sapsis, Michelle Girvan, Edward Ott, and Petros Koumoutsakos. Backpropagation algorithms and reservoir computing in recurrent neural networks for the forecasting of complex spatiotemporal dynamics. *Neural Networks*, 2020.
- [49] Seungjoon Lee, Mahdi Kooshkbaghi, Konstantinos Spiliotis, Constantinos I Siettos, and Ioannis G Kevrekidis. Coarse-scale pdes from fine-scale observations via machine learning. *Chaos: An Interdisciplinary Journal of Nonlinear Science*, 30(1):013141, 2020.
- [50] Christopher M Bishop. Mixture density networks. 1994.
- [51] Marios Mattheakis, P Protopapas, D Sondak, M Di Giovanni, and E Kaxiras. Physical symmetries embedded in neural networks. *arXiv preprint arXiv:1904.08991*, 2019.
- [52] Yann LeCun, Yoshua Bengio, and Geoffrey Hinton. Deep learning. *nature*, 521(7553):436–444, 2015.
- [53] Oriol Vinyals, Samy Bengio, and Manjunath Kudlur. Order matters: Sequence to sequence for sets. *arXiv preprint arXiv:1511.06391*, 2015.
- [54] Sepp Hochreiter and Jürgen Schmidhuber. Long short-term memory. *Neural Comput.*, 9(8):1735–1780, November 1997.
- [55] Junyoung Chung, Caglar Gulcehre, Kyunghyun Cho, and Yoshua Bengio. Empirical evaluation of gated recurrent neural networks on sequence modeling. In *NIPS 2014 Workshop on Deep Learning, December 2014*, 2014.
- [56] Paul J. Werbos. Generalization of backpropagation with application to a recurrent gas market model. *Neural Networks*, 1(4):339 – 356, 1988.
- [57] Diederik P. Kingma and Jimmy Ba. Adam: A method for stochastic optimization. In *3rd International Conference on Learning Representations, ICLR 2015, San Diego, CA, USA, May 7-9, 2015, Conference Track Proceedings*, 2015.
- [58] Yang Cao and Linda Petzold. Accuracy limitations and the measurement of errors in the stochastic simulation of chemically reacting systems. *Journal of Computational Physics*, 212(1):6–24, 2006.
- [59] Richard FitzHugh. Impulses and physiological states in theoretical models of nerve membrane. *Biophysical journal*, 1(6):445, 1961.
- [60] Jinichi Nagumo, Suguru Arimoto, and Shuji Yoshizawa. An active pulse transmission line simulating nerve axon. *Proceedings of the IRE*, 50(10):2061–2070, 1962.
- [61] Iliya V Karlin, Santosh Ansumali, Christos E Frouzakis, and Shyam Sunder Chikatamarla. Elements of the lattice boltzmann method i: Linear advection equation. *Commun. Comput. Phys*, 1(4):616–655, 2006.
- [62] Dieter Armbruster, John Guckenheimer, and Philip Holmes. Kuramoto–sivashinsky dynamics on the center-unstable manifold. *SIAM Journal on Applied Mathematics*, 49(3):676–691, 1989.
- [63] Yoshiki Kuramoto. Diffusion-Induced Chaos in Reaction Systems. *Progress of Theoretical Physics Supplement*, 64:346–367, 02 1978.

- [64] G. I. Sivashinsky. Nonlinear analysis of hydrodynamic instability in laminar flames — I. Derivation of basic equations. *Acta Astronautica*, 4:1177–1206, 1977.
- [65] Predrag Cvitanović, Ruslan L Davidchack, and Evangelos Siminos. On the state space geometry of the kuramoto–sivashinsky flow in a periodic domain. *SIAM Journal on Applied Dynamical Systems*, 9(1):1–33, 2010.
- [66] A. Kassam and L. Trefethen. Fourth-order time-stepping for stiff pdes. *SIAM Journal on Scientific Computing*, 26(4):1214–1233, 2005.

## 5 Appendix A

## 6 Methods

In the following, we describe the different models used in the proposed framework to learn and propagate the effective dynamics (LED) for complex multiscale systems.

### 6.1 Autoencoders (AE)

Classical autoencoders are nonlinear neural networks that map an input to a low dimensional latent space and then decode it to the original dimension at the output, trained to minimize the reconstruction loss  $\mathcal{L} = \|\mathbf{x} - \tilde{\mathbf{x}}\|^2$ . They were proposed in [38] as a nonlinear alternative to Principal Component Analysis (PCA). An autoencoder is depicted in Figure 9a.

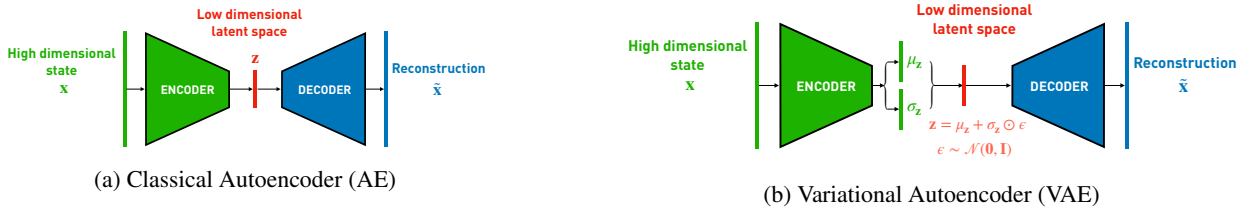


Figure 9: **(a)** A schematic diagram of a classical Autoencoder (AE). A high dimensional state  $\mathbf{x}$  is mapped to a low dimensional feature space  $\mathbf{z}$  by applying the encoder transformation through multiple fully connected layers. The low dimensional feature space  $\mathbf{z}$  is expanded in the original space by the decoder. The autoencoder is trained with the loss  $\mathcal{L} = \|\mathbf{x} - \tilde{\mathbf{x}}\|^2$ , so that the input can be reconstructed as faithfully as possible at the decoder output. **(b)** A schematic diagram of a Variational Autoencoder (VAE). Instead of modeling the latent space deterministically, the encoder outputs a mean latent representation  $\mu_z$ , along with the associated uncertainty  $\sigma_z$ . The latent space  $\mathbf{z}$  is sampled from a normal distribution  $\mathbf{z} \sim \mathcal{N}(\cdot | \mu_z, \sigma_z \mathbf{I})$ , with diagonal covariance matrix.

### 6.2 Variational Autoencoders (VAE)

Research efforts on generative modeling led to the development of Variational Autoencoders (VAEs) [39]. The VAE similar to AE is composed by an encoder and a decoder. The encoder neural network, instead of mapping the input  $\mathbf{x}$  deterministically to a reduced order latent space  $\mathbf{z}$ , produces a distribution  $q(\mathbf{z} | \mathbf{x}; \mathbf{w}_q)$  over the latent representation  $\mathbf{z}$ , where  $\mathbf{w}_q$  is the parametrization of the distribution given by the output of the encoder  $\mathbf{w}_q = \mathcal{E}^{\mathbf{w}_\varepsilon}(\mathbf{x})$ . In most practical applications, the distribution  $q(\mathbf{z} | \mathbf{x}; \mathbf{w}_q)$  is modeled as a factorized Gaussian, implying that  $\mathbf{w}_q$  is composed of the mean, and the diagonal elements of the covariance matrix. The decoder maps a sampled latent representation to an output  $\tilde{\mathbf{x}} = \mathcal{D}^{\mathbf{w}_p}(\mathbf{z})$ . By sampling the latent distribution  $q(\mathbf{z} | \mathbf{x}; \mathbf{w}_q)$ , for a fixed input  $\mathbf{x}$ , the autoencoder can generate samples from the probability distribution over  $\tilde{\mathbf{x}}$  at the decoder output. The network is trained to maximize the log-likelihood of reproducing the input at the output, while minimizing the Kullback-Leibler divergence between the encoder distribution  $q(\mathbf{z} | \mathbf{x}; \mathbf{w}_q)$  and a prior distribution, e.g.  $\mathcal{N}(0, \mathbf{I})$ . VAEs are essentially regularizing the training of AE by adding the Gaussian noise in the latent representation. In this work, we take into account a Gaussian latent distribution with diagonal covariance matrix

$$q(\mathbf{z} | \mathbf{x}; \underbrace{\mu_z, \sigma_z}_{\mathbf{w}_q}) = \mathcal{N}(\mathbf{z} | \mu_z(\mathbf{x}), \text{diag}(\sigma_z(\mathbf{x}))), \quad (9)$$

where the mean latent representation  $\mu_z$  and the variance  $\sigma_z$  vectors are the outputs of the encoder neural network  $\mathcal{E}^{\mathbf{w}_\varepsilon}(\mathbf{x})$ . The latent representation is then sampled from  $\mathbf{z} \sim \mathcal{N}(\cdot | \mu_z, \text{diag}(\sigma_z))$ . The decoder receives as an input the sample, and outputs the reconstruction  $\tilde{\mathbf{x}}$ . A VAE is depicted in Figure 9b.

### 6.3 Permutation Invariance

Physical systems may satisfy specific properties like energy conservation, translation invariance, permutation invariance, etc. In order to build data-driven models that accurately reproduce the statistical behavior of such systems, these properties should ideally be embedded in the model. Translation invariance is taken into account in the design of the convolution operator in Convolutional neural networks (CNNs) developed to process images [52]. Other type of

properties like energy conservation and physical symmetries are discussed in [51]. In this section, we describe how we can ensure permutation invariance to model the dynamics of particles of the same kind. This is useful in simulations of molecules, i.e. molecular dynamics, where the state of the system is described by a configuration of particles, and any permutation of these particles corresponds to the same configuration. Permutation invariance is handled here with a sum decomposition of a feature space [53]. The exact procedure is depicted in Figure 10.

Assume that the state of a dynamical system  $s$  is composed of  $N$  particles of the same kind, each one having specific properties or features with dimensionality  $d_x$ , e.g. position, velocity, etc. The features of a single particle are given by the state  $\mathbf{x} \in \mathbb{R}^{d_x}$  of the particle. As an input to the network, we provide raw data, i.e. the features of all particles, stacked together in a matrix  $s \in \mathbb{R}^{N \times d_x}$ . The problem we are dealing with is that a permutation of two particles represents in essence the same configuration and should be mapped to the same latent representation. This is achieved with a permutation invariant layer that first applies a nonlinear transformation  $\phi : \mathbb{R}^{d_x} \rightarrow \mathbb{R}^{d_p}$  mapping each particles' features to a high dimensional latent representation of dimension  $d_p$ . This mapping is applied to all particles independently leading to  $N$  such latent vectors. The mean of these vectors is taken to construct the representation of the configuration. The representation  $\frac{1}{N} \sum_{i=1}^N \phi(\mathbf{x}^i)$  is finally fed to a final layer reducing the dimensionality to a low-order representation  $\mathbf{z} \in \mathbb{R}^{d_z}$ , with  $d_z \ll d_p, N$ . This is achieved by the mapping  $g : \mathbb{R}^{d_p} \rightarrow \mathbb{R}^{d_z}$ . In this work, we utilize the permutation invariance layer in the modeling of the collective dynamics of a group of particles whose movement is governed by the advection-diffusion equation in the one and three dimensional space. Both mappings  $g$  and  $\phi$  are implemented with neural networks, having 5 layers of 100 hidden units each, residual connections, and tanh activations.

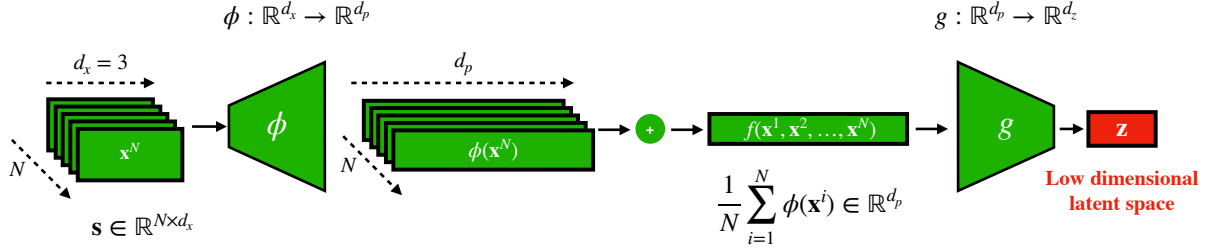


Figure 10: Illustration of the permutation invariant encoder. The input of the network is composed of  $N$  atomic states that are permutation invariant, e.g. positions  $\{\mathbf{x}^1, \dots, \mathbf{x}^N\}$  of  $N$  particles in a particle simulation, each one with dimension  $d_x$ , i.e.  $\mathbf{x}^i \in \mathbb{R}^{d_x}, \forall i \in \{1, \dots, N\}$ . A transformation  $\phi(\cdot) : \mathbb{R}^{d_x} \rightarrow \mathbb{R}^{d_p}$  is applied to each atomic state separately, mapping to a high dimensional latent feature space. The mean of these latent representations of the atomic states is computed, leading to a single latent feature that is permutation invariant with respect to the input. The final layer of the encoder maps the high-dimensional feature to a low dimensional representation  $\mathbf{z}$ , which is again permutation invariant with respect to the input, representing the encoding of the global state.

#### 6.4 Mixture Density Decoder

Mixture density networks (MDNs) [50] are powerful neural networks that can model non-Gaussian, multi-modal data distributions. The outputs of MDNs are parameters of a mixture density model (mixture of probability density functions). The most generic choice of the mixture component distribution, is the Gaussian distribution. Gaussian MDNs are widely deployed in machine learning applications to model structured dynamic environments, i.e. (video) games. However, the effectiveness of MDNs in modeling physical systems remains unexplored.

In physical systems, the state may be bounded. In this case, the choice of a Gaussian MDN is problematic due to its unbounded support. To make matters worse, most applications of Gaussian MDNs when modeling random vectors do not consider the interdependence between the vector variables, i.e. the covariance matrix of the Gaussian mixture components is diagonal, in an attempt to reduce their computational complexity. Arguably in the applications where they were successful, modeling this interdependence was not imperative. In contrast, in physical systems the variables of a state might be very strongly dependent on each other. In order to cope with these problems we consider the following approach. Firstly, we model the distribution  $p(\mathbf{v}|\mathbf{z})$  of an auxiliary vector variable  $\mathbf{v} \in \mathbb{R}^{d_x}$ , of the same dimensionality  $d_x$  as the high dimensional state (input/output of the autoencoder). The distribution is modeled as a mixture of  $K$  **multivariate** Normal distributions

$$p(\mathbf{v}|\mathbf{z}) = \sum_{k=1}^K \pi^k(\mathbf{z}) \mathcal{N}\left(\boldsymbol{\mu}_v^k(\mathbf{z}), \Sigma_v^k(\mathbf{z})\right), \quad (10)$$

We parametrize the multivariate normal distribution in terms of a mean vector  $\boldsymbol{\mu}_v^k$ , a positive definite covariance matrix  $\Sigma_v^k$ , and the mixing coefficients  $\pi^k$  which are functions of  $\mathbf{z}$ . The covariance matrix is parametrised by a lower-triangular matrix  $L_v^k$  with positive-valued diagonal entries, such that  $\Sigma_v^k = L_v^k L_v^{kT} \in \mathbb{R}^{d_x \times d_x}$  (This triangular matrix can be recovered by Cholesky factorization of the positive definite  $\Sigma_v^k$ ). The functional forms of  $\pi^k(\mathbf{z}) \in \mathbb{R}$ ,  $\boldsymbol{\mu}_v(\mathbf{z}) \in \mathbb{R}^{d_x}$ , and the  $n(n+1)/2$  entries of  $L_v^k$  are neural networks, their values are given by the outputs of the decoder for all mixture components  $k \in \{1, \dots, K\}$ , i.e.  $\mathbf{w}_D = \mathcal{D}^{\mathbf{w}_D}(\mathbf{z}) = \{\pi^k, \boldsymbol{\mu}_v^k, L_v^k\}_{1, \dots, K}$ . The positivity of the diagonal elements of  $L_v^k$  is ensured by a **softplus** activation function

$$f(x) = \ln(1 + \exp(x)) \quad (11)$$

in the respective outputs of the decoder. The mixing coefficients satisfy  $0 \leq \pi^k < 1$  and  $\sum_{k=1}^K \pi^k = 1$ . To ensure these conditions, the respective outputs of the decoder are passed through a **softmax** activation

$$\sigma(\mathbf{x})_i = \frac{e^{\mathbf{x}_i}}{\sum_i e^{\mathbf{x}_i}}. \quad (12)$$

The rest (non-diagonal elements and mean vector) of the decoder outputs have linear activations, so no restriction in their sign. In total, the decoder output is composed of  $K(n-1)n/2 + Kn$  single valued outputs with linear activation for the non-diagonal elements of  $L_v^k$  and the mean vectors  $\boldsymbol{\mu}_v^k$ , and  $Kn$  positive outputs with softplus activation for the diagonal of  $L_v^k$ , and  $K$  outputs with softmax activation for the mixing coefficients.

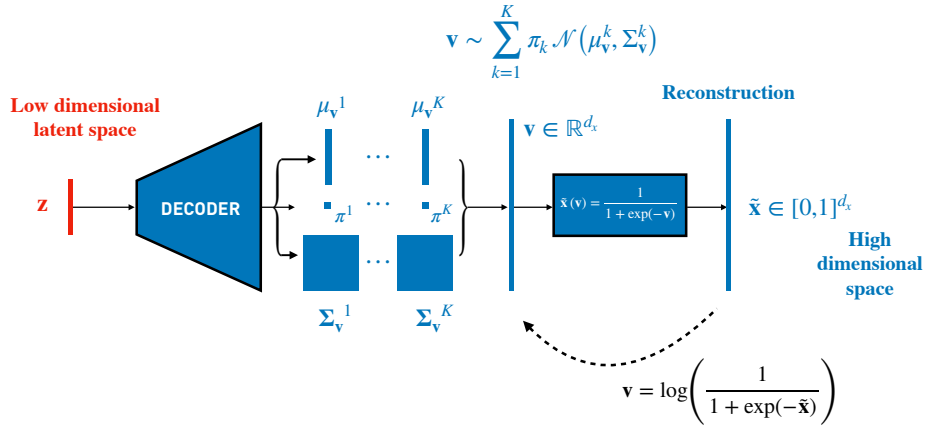


Figure 11: A mixture density network modeling the probability density  $p(\tilde{\mathbf{x}}|\mathbf{z})$ , with bounded  $\tilde{\mathbf{x}}$ . The decoder maps the latent state  $\mathbf{z}$  to the parameters of a mixture model on the latent vector  $\mathbf{v} \in \mathbb{R}^{d_x}$ , which are the mixing coefficients  $\pi^k \in \mathbb{R}$ , mean vectors  $\boldsymbol{\mu}_v^k \in \mathbb{R}^{d_x}$ , and a lower-triangular matrix  $L_v^k \in \mathbb{R}^{d_x \times d_x}$  with positive-valued diagonal entries. From the latter, the covariance matrix is derived from  $\Sigma_v^k = L_v^k L_v^{kT}$  which is positive definite by construction. The mixture models the probability distribution of the latent state  $p(\mathbf{v}|\mathbf{z})$ . However, the targets used to train the network in a supervised way are defined on the reconstruction  $\tilde{\mathbf{x}}$ . The targets are scaled to  $\tilde{\mathbf{x}} \in [0, 1]^{d_x}$ , and then transformed to targets for  $\mathbf{v}$  using the inverse of the softplus activation. The MDN autoencoder is trained to maximize the likelihood  $p(\mathbf{v}|\mathbf{z})$  of the transformed data  $\mathbf{v}$ .

## 6.5 Recurrent Neural Networks

In the low order manifold (coarse, latent state), a Recurrent Neural Network (RNN) is utilized to capture the nonlinear, non-markovian dynamics. The forecasting rule of the RNN is given by

$$\mathbf{h}_t = \mathcal{H}^{\mathbf{w}_H}(\mathbf{z}_t, \mathbf{h}_{t-\Delta t}), \quad \tilde{\mathbf{z}}_{t+\Delta t} = \mathcal{R}^{\mathbf{w}_R}(\mathbf{h}_t), \quad (13)$$

where  $\mathbf{w}_H$  and  $\mathbf{w}_R$  are the trainable parameters of the network,  $\mathbf{h}_t \in \mathbb{R}^{d_h}$  is an internal hidden memory state, and  $\tilde{\mathbf{z}}_{t+\Delta t}$  is a prediction of the latent state. The RNN is trained to minimize the forecasting loss  $\|\tilde{\mathbf{z}}_{t+\Delta t} - \mathbf{z}_{t+\Delta t}\|_2^2$ , which can be written as

$$\|\tilde{\mathbf{z}}_{t+\Delta t} - \mathbf{z}_{t+\Delta t}\|_2^2 = \|\mathcal{R}^{\mathbf{w}_R}(\mathbf{h}_t) - \mathbf{z}_{t+\Delta t}\|_2^2 = \|\mathcal{R}^{\mathbf{w}_R}(\mathcal{H}^{\mathbf{w}_H}(\mathbf{z}_t, \mathbf{h}_{t-\Delta t})) - \mathbf{z}_{t+\Delta t}\|_2^2. \quad (14)$$

This leads to

$$\mathbf{w}_{\mathcal{H}}, \mathbf{w}_{\mathcal{R}} = \underset{\mathbf{w}_{\mathcal{H}}, \mathbf{w}_{\mathcal{R}}}{\operatorname{argmin}} \|\mathcal{R}^{\mathbf{w}_{\mathcal{R}}}(\mathcal{H}^{\mathbf{w}_{\mathcal{H}}}(z_t, \mathbf{h}_{t-\Delta t})) - z_{t+\Delta t}\|_2^2. \quad (15)$$

The RNNs are trained with Backpropagation through time (BPTT) [56]. In this work, we consider two implementations of the mappings  $\mathcal{H}^{\mathbf{w}_{\mathcal{H}}}$  and  $\mathcal{R}^{\mathbf{w}_{\mathcal{R}}}$ , the long short-term memory (LSTM) [54] cell and the Gated Recurrent Unit (GRU) [55]. The output mapping for both cells is given by a linear transformation, i.e.

$$\tilde{z}_{t+\Delta t} = W_{z,h} \mathbf{h}_t, \quad (16)$$

where  $W_{z,h} \in \mathbb{R}^{d_z \times d_h}$ . As a consequence, the set of trainable weights of the hidden-to-output mapping is just one matrix  $\mathbf{w}_{\mathcal{R}} = W_{z,h} \in \mathbb{R}^{d_z \times d_h}$  for both cells. However, the architecture of the hidden-to-hidden mapping, is different. In the following, we describe these implementations for both cells.

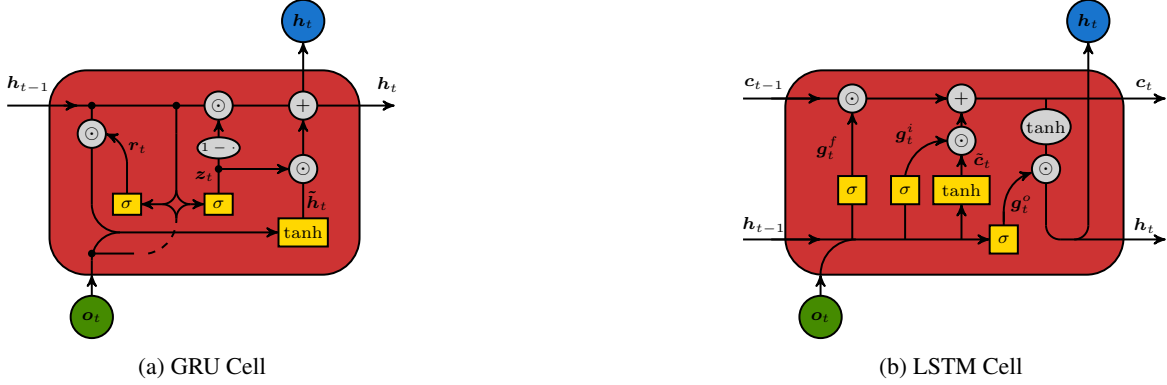


Figure 12: The information flow for a Gated Recurrent Unit (GRU) cell and a Long Short-Term Memory (LSTM) cell. The cells employ gating mechanisms that allow forgetting and storing of information in the processing of the hidden state. Ellipses and circles denote entry-wise operations, while rectangles denote layer operations.

### 6.5.1 Gated Recurrent Unit (GRU)

In the GRU cell, the functional form of the mapping  $\mathbf{h}_t = \mathcal{H}^{\mathbf{w}_{\mathcal{H}}}(z_t, \mathbf{h}_{t-\Delta t})$  is given by

$$\begin{aligned} \mathbf{u}_t &= \sigma_g(W_{\mathbf{u}}[\mathbf{h}_{t-\Delta t}, z_t] + \mathbf{b}_{\mathbf{u}}) \\ \mathbf{r}_t &= \sigma_g(W_{\mathbf{r}}[\mathbf{h}_{t-\Delta t}, z_t] + \mathbf{b}_{\mathbf{r}}) \\ \tilde{\mathbf{h}}_t &= \tanh(W_{\mathbf{h}}[\mathbf{r}_t \odot \mathbf{h}_{t-\Delta t}, z_t] + \mathbf{b}_{\mathbf{h}}) \\ \mathbf{h}_t &= (1 - \mathbf{u}_t) \odot \mathbf{h}_{t-\Delta t} + \mathbf{u}_t \odot \tilde{\mathbf{h}}_t, \end{aligned} \quad (17)$$

where  $z_t \in \mathbb{R}^{d_z}$  is the latent state (output of the encoder, or previous time-step of the RNN) provided at the input of the RNN at time  $t$ ,  $\mathbf{u}_t \in \mathbb{R}^{d_h}$  is the update gate vector,  $\mathbf{r}_t \in \mathbb{R}^{d_h}$  is the reset gate vector,  $\tilde{\mathbf{h}}_t \in \mathbb{R}^{d_h}$ ,  $\mathbf{h}_t \in \mathbb{R}^{d_h}$  is the internal hidden memory state,  $W_{\mathbf{u}}, W_{\mathbf{r}}, W_{\mathbf{h}} \in \mathbb{R}^{d_h \times (d_h + d_z)}$  are weight matrices and  $\mathbf{b}_{\mathbf{u}}, \mathbf{b}_{\mathbf{r}}, \mathbf{b}_{\mathbf{h}} \in \mathbb{R}^{d_h}$  biases. The gating activation  $\sigma_g$  is a sigmoid. An illustration of the information flow in a GRU cell is given in Figure 12a.

### 6.5.2 Long Short-Term Memory Unit (LSTM)

The architecture of the LSTM cell is slightly more complicated. The LSTM possesses two hidden states, a cell state  $\mathbf{c}$  and an internal memory state  $\mathbf{h}$ . The hidden-to-hidden mapping

$$\mathbf{h}_t, \mathbf{c}_t = \mathcal{H}^{\mathbf{w}_{\mathcal{H}}}(z_t, \mathbf{h}_{t-\Delta t}, \mathbf{c}_{t-\Delta t}) \quad (18)$$

takes the form

$$\begin{aligned} \mathbf{g}_t^f &= \sigma_f(W_f[\mathbf{h}_{t-\Delta t}, z_t] + \mathbf{b}_f) & \mathbf{g}_t^i &= \sigma_i(W_i[\mathbf{h}_{t-\Delta t}, z_t] + \mathbf{b}_i) \\ \tilde{\mathbf{c}}_t &= \tanh(W_c[\mathbf{h}_{t-\Delta t}, z_t] + \mathbf{b}_c) & \mathbf{c}_t &= \mathbf{g}_t^f \odot \mathbf{c}_{t-\Delta t} + \mathbf{g}_t^i \odot \tilde{\mathbf{c}}_t \\ \mathbf{g}_t^z &= \sigma_h(W_h[\mathbf{h}_{t-\Delta t}, z_t] + \mathbf{b}_h) & \mathbf{h}_t &= \mathbf{g}_t^z \odot \tanh(\mathbf{c}_t), \end{aligned} \quad (19)$$

where  $\mathbf{g}_t^f, \mathbf{g}_t^i, \mathbf{g}_t^z \in \mathbb{R}^{d_h}$ , are the gate vector signals (forget, input and output gates),  $z_t \in \mathbb{R}^{d_z}$  is the latent input at time  $t$ ,  $\mathbf{h}_t \in \mathbb{R}^{d_h}$  is the hidden state,  $\mathbf{c}_t \in \mathbb{R}^{d_h}$  is the cell state, while  $W_f, W_i, W_c, W_h \in \mathbb{R}^{d_h \times (d_h + d_z)}$ , are weight matrices

and  $\mathbf{b}_f, \mathbf{b}_i, \mathbf{b}_c, \mathbf{b}_h \in \mathbb{R}^{d_h}$  biases. The symbol  $\odot$  denotes the element-wise product. The activation functions  $\sigma_f, \sigma_i$  and  $\sigma_h$  are sigmoids. The dimension of the hidden state  $d_h$  (number of hidden units) controls the capacity of the cell to encode history information. The set of trainable parameters of the recurrent mapping  $\mathcal{H}^{w_h}$  is thus given by

$$\mathcal{H}^{w_h} = \{\mathbf{g}_t^f, \mathbf{g}_t^i, \mathbf{g}_t^z, W_f, W_i, W_c, W_h\} \quad (20)$$

An illustration of the information flow in a LSTM cell is given in Figure 12b.

## 6.6 Multiscale Modeling with LEDMuS

In this work, we consider discrete time autonomous dynamical systems of the form

$$\mathbf{s}_{t+\Delta t} = \mathbf{F}(\mathbf{s}_t), \quad (21)$$

where  $\mathbf{s}_t \in \mathbb{R}^{d_s}$  is the state of the dynamical system at time  $t$ ,  $\Delta t$  is the sampling period and  $\mathbf{F}$  is a function representing the discrete time dynamics. The dynamics  $\mathbf{F}$  may be nonlinear, deterministic or stochastic. In our study, we are interested in systems whose state  $\mathbf{s}_k$  is high dimensional, but the intrinsic dimensionality of the dynamics is low. The complete description of high-dimensional systems with nonlinear dynamics through the governing equations is often challenging for numerous reasons: either because the equations  $\mathbf{F}$  might be unknown, the dynamics might be very hard or computationally expensive to solve with an appropriate resolution, or due to the magnitude of model errors. In many cases, we are interested in more macroscopic, coarse grained characteristics that can be resolved by the large scales. Moreover, the effective system dynamics might live on a low dimensional manifold. Employing classical order reduction methods such as Galerkin projection can be problematic as the truncated modes (i.e. small scales) might be relevant for the effective dynamics, i.e. back-scattering. As a consequence, their effect on the dynamic evolution on the larger scales has to be considered, i.e. closure models in turbulence.

In this work, we propose to learn the effective dynamics (LED) of complex system by coupling an autoencoder (either normal or variational) with a RNN, that learns to forecast these dynamics, and a (mixture density in case of stochastic systems) decoder that reconstructs the high dimensional dynamics. First, the networks are trained with the Adam stochastic optimization method [57]. The trained networks can be utilized to capture and forecast the evolution the dynamics on unseen test data. Given a short-term evolution of the state of a simulation based on first principles composed of  $T_{warm}$  initial time steps  $\{\mathbf{s}_{t-T_{warm}+\Delta t}, \dots, \mathbf{s}_t\}$ , we propose to “teacher force” the LED, iteratively feeding the encoder the high dimensional states, passing the computed latent representations  $\mathbf{z}$  at every time-step to the RNN, and propagating the latent state  $\mathbf{h}_t$  of the RNN up to time-step  $t$ . After this short initial warm-up phase, the dynamics of the system can be propagated on this low-dimensional latent state (coarse representation, or macro dynamics) for a long time horizon  $T_m \gg T_{warm}$  by utilizing the computationally cheap RNN forecasting rule, while the decoder can be utilized to map the latent space back to the high dimensional state space whenever needed. An illustration of the proposed iterative prediction on the latent space is given in Figure 13.

As is the case for any iterative forecasting method, initial model errors will propagate. In order to alleviate this, we propose the following multiscale scheme. Starting from an initial condition, for a warm-up period  $T_{warm}$  the autoencoder projects the high dimensional state to the latent space, while the latent states are fed to the RNN to warm-up its hidden state. For this period  $T_{warm}$  the dynamics are evolved on the high dimensional state, while the RNN is “teacher forced” with the respective latent state at the output of the autoencoder. No forecasting takes place in this initial period. After this initial warm-up period, we propose to iteratively **(1)** propagate the dynamics on the low-dimensional latent space with the RNN for some time  $T_m$ , **(2)** project the latent dynamics at  $t = T_m$  back to the high dimensional state, **(3)** starting from this high-dimensional state as an initial condition, use the **equations/first principles** to evolve the dynamics for  $T_\mu$ , and so on and so forth. The power of the proposed data-driven approach is that it utilizes state of the art deep learning methods, it does not rely on constraints on the system dynamics, it can be utilized to propagate the latent dynamics without the need to transform back to the high-dimensional state space at every time-step, and it can be applied in a generic way augmenting the arsenal of models developed for multiscale problems [19]. The multiscale switching procedure is illustrated in Figure 14.

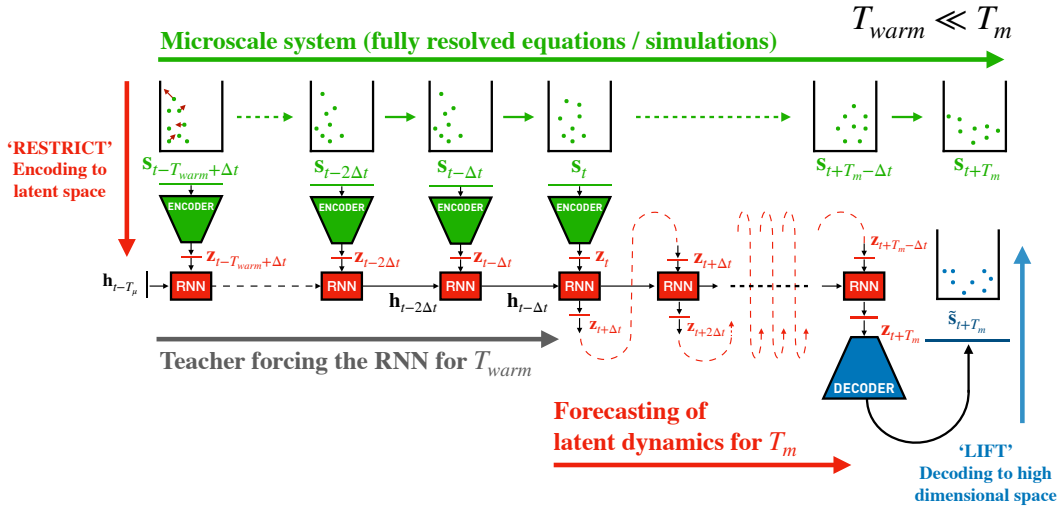


Figure 13: An illustration of the iterative latent space propagation in LED. The high-dimensional state of the dynamical system is passed through the encoder network for some initial time  $T_{warm}$ . The low-dimensional tractable latent representation at the output of the encoder  $z$  is provided as an input to the RNN. Starting from the last latent state ( $z_t$  in the figure), we deploy the RNN to iteratively propagate the dynamics in the latent space up to a total horizon of  $T_m$  timesteps, with  $T_m \gg T_{warm}$ . The decoder can be utilized to upscale the latent state back to the high-dimensional state of the dynamical system, i.e.  $\tilde{s}_{t+T_m} = \mathcal{D}^{w^D}(z^{t+T_m})$ . Due to the fact that the propagation in the latent space can be orders of magnitude cheaper than the evolution of high dimensional dynamics based on first principles, LED can accelerate simulations of dynamical systems. As a consequence, we can achieve longer simulation times, explore the state space faster, and resolve time and spatial scales that would be otherwise intractable.

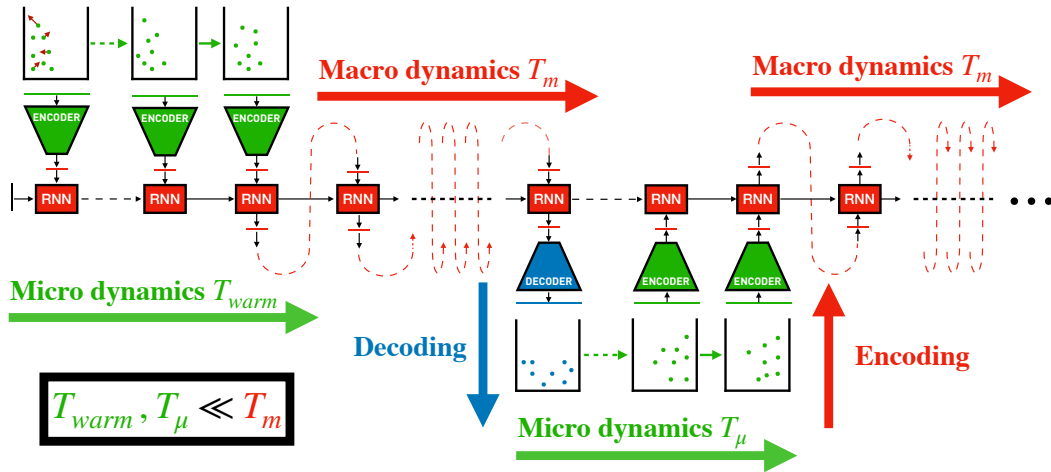


Figure 14: Multiscale forecasting with LED (**testing phase**). By iteratively switching between the computationally cheap propagation in the latent space for a large time horizon  $T_m$  and a computationally expensive model based on first principles for  $T_\mu$ , we may iteratively correct the statistical error and increase further the simulation horizon, without sacrificing the performance of the method, albeit at the cost of a reduction in the overall speed-up of LED compared to solely propagating on the latent space. The speed-up is considered here with respect to propagating the computationally expensive high dimensional dynamics in the micro scale.

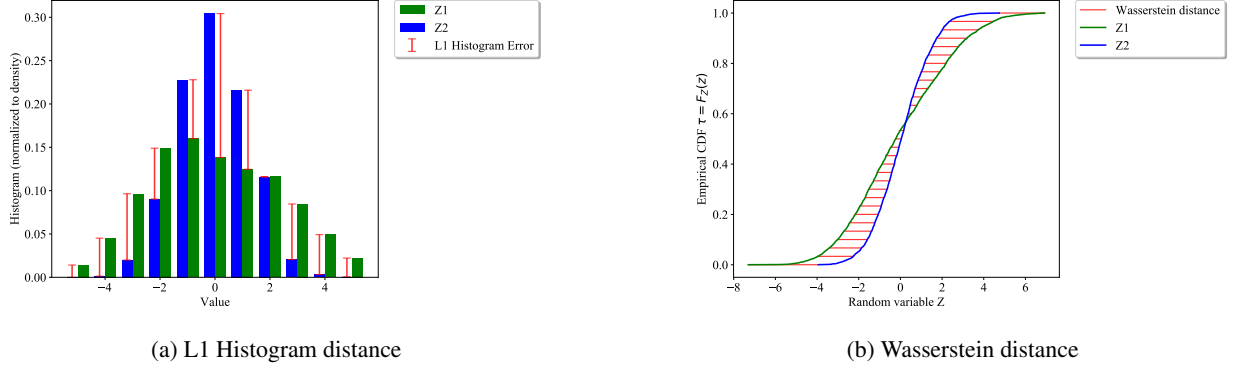


Figure 15: (a) A schematic illustration of the L1 difference of the histograms of two random variables  $Z_1$  and  $Z_2$ . In (b) the Wasserstein distance between the distributions based on the inverse Cumulative Distribution Function (CDF).

## 7 Comparison Measures

In this section, we elaborate on the metrics used to quantify the effectiveness of the proposed approach to capture the dynamics and the state statistics of the systems under study. To quantify the prediction performance of the method in a deterministic system, we use the mean normalized absolute difference (MNAD). The Wasserstein distance (WD) and the L1-Norm histogram distance (L1-NHD) are utilized to quantify the difference between two statistical objects (either state distributions, or random variables).

### 7.1 Mean normalised absolute difference (MNAD)

Assume that a model is used to predict a spatiotemporal field  $y(x, t)$ , at discrete state  $x_i$  and time  $t_j$  locations. Predicted values from a model (neural network, etc.) are denoted with  $\tilde{y}$ , while the groundtruth (simulation of the equations with a solver based on first principles) with  $y$ . The normalized absolute difference (NAD) between the model output and the groundtruth is defined as

$$\text{NAD}(t_j) = \frac{1}{N_x} \sum_{i=1}^{N_x} \frac{|y(x_i, t_j) - \tilde{y}(x_i, t_j)|}{\max_{i,j}(y(x_i, t_j)) - \min_{i,j}(y(x_i, t_j))}, \quad (22)$$

where  $N_x$  is the dimensionality of the discretized state  $x$ . The NAD depends on the time  $t_j$ . The mean NAD (MNAD) is given by the mean over time of the NAD score, i.e.

$$\text{MNAD} = \frac{1}{N_T} \sum_{j=1}^{N_T} \text{NAD}(t_j), \quad (23)$$

where  $N_T$  is the number of timesteps considered. The MNAD is used in the deterministic FitzHugh-Nagumo equation to measure the prediction error of LED and compare it with the state of the art.

### 7.2 Wasserstein Distance

The Wasserstein distance (WD), is a metric used to quantify the difference between the distribution functions of two random variables. It is defined as the integral of the absolute difference of the inverse Cumulative Distribution Functions (CDF) of the random variables. Assuming two random variables  $Z_1$  and  $Z_2$ , with CDFs given by  $\tau = F_{Z_1}(z)$  and  $F_{Z_2}(z)$ , with  $\tau \in [0, 1]$ , the Wasserstein metric is defined as

$$\text{WD}(Z_1, Z_2) = \int_0^1 |F_{Z_1}^{-1}(\tau) - F_{Z_2}^{-1}(\tau)| d\tau. \quad (24)$$

An illustration of WD is given in Figure 15b. In high-dimensional problems, where the random variable is multivariate (random vector), we are reporting the mean WD of each variable after marginalization of all others.

### 7.3 L1-Histogram Distance

In order to quantify the difference of the distributions of two random multivariate random variables  $Z_1$  and  $Z_2$ , we employ in addition to the WD, the L1-Norm histogram distance (L1-NHD). We measure this metric based on the L1

norm of the difference between the normalized histograms of the random variables computed on the same grid. An illustration of the L1-histogram distance is given in Figure Figure 15a. The number of bins for the computation of the histograms, is selected according to Rice rule, given by  $N_{bins} = \lceil 2 \sqrt[3]{n} \rceil$  where  $n$  is the number of observations in the sample  $z$ . The WD and the L1-NHD are used to measure the difference between the distribution of the state in the Advection-Diffusion in 1-D and 3-D (over a single run). Moreover, they are used to measure the difference between the distributions of the mean and variance of the state over multiple runs.

## 8 Results

We evaluate the effectiveness of LED to model the stochastic dynamics of the advection-diffusion equation in one dimension in Section 8.1 and three dimensions in Section 8.2. Moreover, in Section 8.3 we benchmark LED against equation free approaches proposed in [49] that are based on uncovering a PDE on the coarse level using diffusion maps, Gaussian processes or neural networks, and using forward integration in the coarse representation to model the FitzHugh-Nagumo equation. Last but not least, in Section 8.4 we apply LED on the challenging Kuramoto-Sivashinsky equation exhibiting deterministic chaos, unraveling a low dimensional inertial manifold. All LED models are implemented in Pytorch, mapped to a single Nvidia Tesla P100 GPU and executed on the XC50 compute nodes of the Piz Daint supercomputer at the Swiss national supercomputing centre (CSCS).

### 8.1 Advection-Diffusion with Brownian dynamics 1-D

In this section, we evaluate LED on a system of  $N$  point particles on a bounded domain  $\Omega = [-L/2, L/2]^{d_x}$ , where  $d_x$  is the dimension of the space, whose dynamics are determined by the advection-diffusion equation, modeled with the stochastic differential equation (SDE)

$$dx_t = \mathbf{u}(t)dt + \sqrt{D} d\mathbf{W}_t, \quad (25)$$

where  $x_t \in \Omega$  denotes the position of the particle at time  $t$ ,  $D \in \mathbb{R}$  is the diffusion coefficient,  $d\mathbf{W}_t \in \mathbb{R}^{d_x}$  is a Wiener process, and  $\mathbf{u}(t) = \mathbf{A} \cos(\omega t) \in \mathbb{R}^{d_x}$  is a cosine advection (drift) term. Equation (25) is solved with initial conditions  $x_0 = \mathbf{0}$  and reflective boundary conditions, ensuring that  $x_t \in \Omega, \forall t$ . The system is advanced in time with explicit Euler integration. We pick a domain size of  $L = 1$ . In this section, we consider the one dimensional case with  $d_x = 1$ . We solve for  $N = 1000$  particles, and consider the values  $D = 0.2$ ,  $A = 1$  and  $\omega = 0.1$ . The stochastic dynamics are solved with a timestep  $\delta t = 10^{-3}$ . By saving the positions of the particles at a coarser time-step  $\Delta t = 0.5$  and starting from different random initial conditions, we generate three datasets, a training and a validation dataset, each consisting of  $10^3$  samples, and a test dataset with  $10^4$  samples. We trained a VAE with permutation invariant input

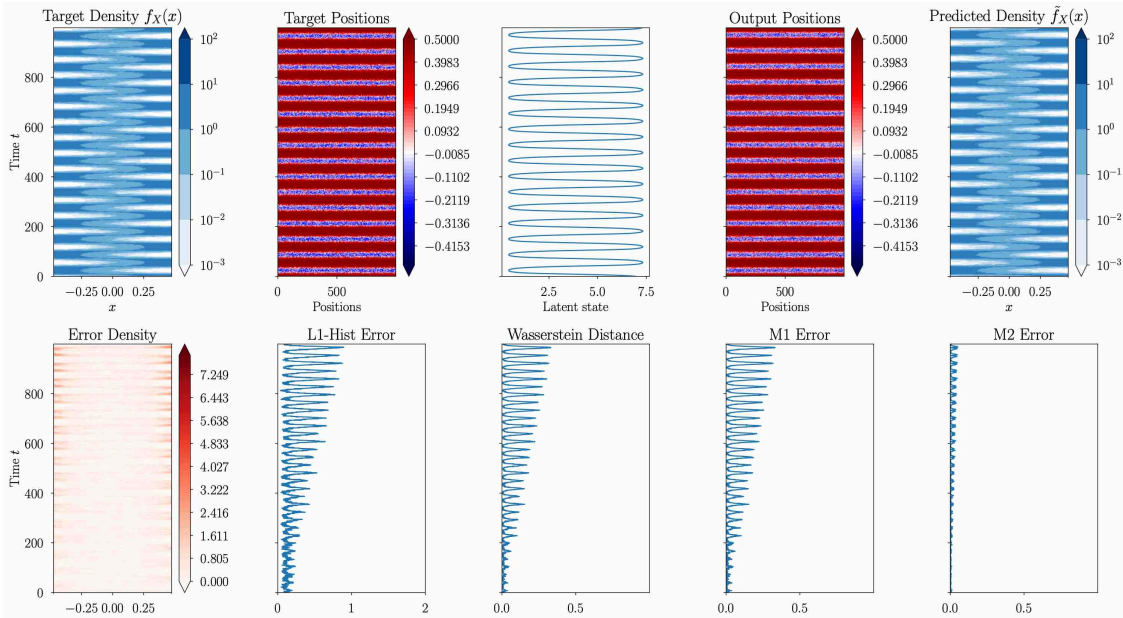


Figure 16: LED applied on the one dimensional Advection-Diffusion equation. The dimensionality of the latent dimension of the VAE is  $d_z = 1$ . LED successfully uncovered the cosine dynamics on the latent space, even though the dimensionality of the original state  $s_t$  describing the state of the system  $s_t \in \mathbb{R}^N$ , with  $N = 1000$ . However, due to the iterative propagation of the latent dynamics with LED, a phase lag is introduced, making the error to increase with time. This can be seen for example, in the error on the estimated mean position (M1) of the particles. Nevertheless, the variance is captured along with the long-term statistical behavior.

layer, a latent dimension  $d_z = 1$ , and a mixture density decoder to compress the dynamics. Then, we trained the RNN of LED to forecast the one-dimensional latent dynamics. The result of an iterative prediction on the test dataset is given

in Figure 16. The warm-up period of LED is set to  $T_{warm} = 60$ . The network is fed an initial configuration of particles  $\mathbf{s}_t = [x_t^1, \dots, x_t^N]^T \in \mathbb{R}^N$ , compresses the configuration to one number  $z_t \in \mathbb{R}$ , and utilizes the RNN to forecast the next latent dynamics  $z_{t+1}$ . From this latent space, the MD decoder of LED is sampling the next configuration  $\mathbf{s}_{t+1}$ . LED successfully uncovered the inherent cosine dynamics of the stochastic movement of the particles, even though the dimensionality of the reduced order space was very low ( $d_z = 1$ ). We plot the L1-Histogram error between the predicted and true density of particle positions, along with the Wasserstein distance and the error on the first two moments on the particle positions as a function of time. From the low dimensional latent space, the decoder of LED learned to map to the position of the  $N = 1000$  particles, as depicted by the low error on the densities. As expected, due to the iterative propagation of the model error, the prediction diverges and there is a phase lag between the predicted and the true dynamics. This causes an increase of the error on the estimated mean position of the particles (M1) and an error on the variance (M2). Even though the error on the variance is kept low, the error on M1 is increasing as we iteratively forecast for a large horizon. The statistics of the system are reproduced accurately, as depicted in Figure 17, where we plot the true and predicted distribution of positions over all timesteps.

Regarding the hyperparameters of LED, we tune them based on a grid search reported in Section 8.1.2. The inputs to the network are scaled to  $[0, 1]$ , while adding noise in the input did not improve performance for this case. Performance is measured in terms of the maximum data likelihood of the MD autoencoder, and the minimum root mean square error for the RNN part, which are trained independently. The autoencoder with the highest likelihood from our grid search, turned out to be a VAE, with a permutation invariant input layer (function  $\phi$  in Figure 10) consisting of 5 residual layers of 100 nodes and tanh activation, mapping to a permutation invariant latent space of dimension  $M = 200$  with mean feature function, with an additional residual autoencoder (modeling function  $g$  in Figure 10) with 5 layers of 100 hidden nodes each and tanh activation, reducing the dimensionality to a latent space of dimension  $d_z = 1$ . Finally, the decoder is composed of 5 additional residual layers of 100 size each, and a mixture density output layer, with 50 hidden units, and 4 kernels outputting the parameters for the mixture coefficients, the means, and the covariance matrices of the 4 kernels. A configuration can be sampled in a trivial way from this representation. Regarding the RNN part of LED, a stateful LSTM with 1 layer of 100 nodes trained with a BBT truncated length of 100 exhibited the lowest validation error.



Figure 17: **(a)** Low order ( $d_z = 1$ ) latent dynamics uncovered by LED, the plot shows the latent state  $z_{t+1}$  as a function of  $z_t$ , while colored according to the density of the values. We observe that the network successfully unraveled the two quasi stable states (particles concentrating on the left or right wall due to the *cos* advection term). **(b)** True distribution of the particle position values, and the predicted one by LED.

In the following, we employ LED to perform multiscale forecasting switching between propagation of the latent dynamics for  $T_m = 450$  and evolution of the particle dynamics for  $T_\mu = 50$ , leading to a multiscale ratio of  $\rho = T_m/T_\mu = 9$ . The initial warm-up period of LED is  $T_{warm} = 60$ . The iterative propagation on the test set is plotted in Figure 18. We observe that by switching to the particle configuration and evolving the dynamics, we alleviate the iterative error propagation, at the additional cost of propagating the original system dynamics (Brownian motion of the  $N = 1000$  particles) for 10% of the total time. The statistics of the system are captured well as demonstrated by the low error on the L1-Histogram error, the mean (M1) and variance (M2) of the particles. For a more detailed statistical analysis of the effectiveness of the proposed approach in modeling the dynamics of the Advection-Diffusion system, please refer to Section 8.1.1.

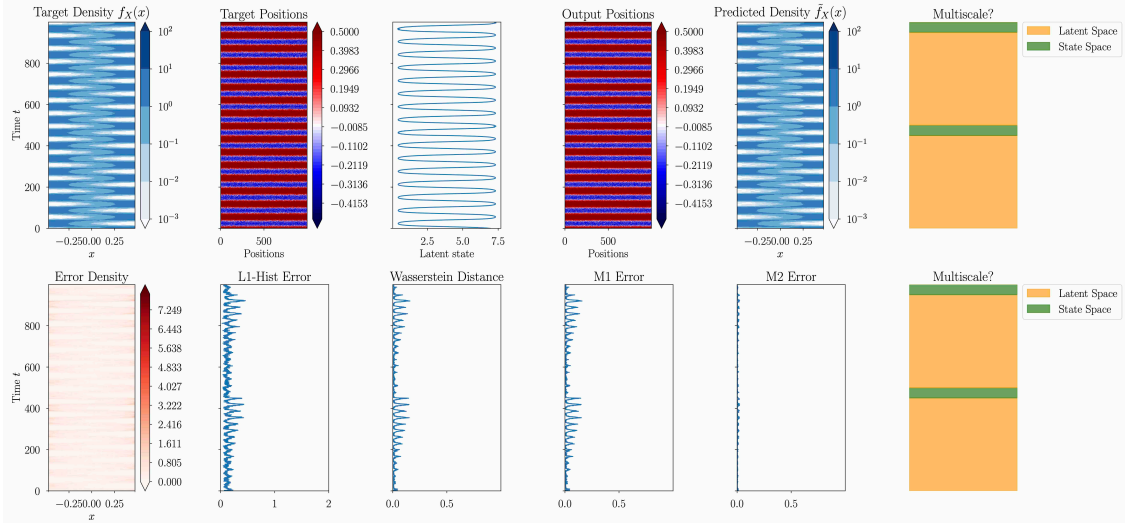


Figure 18: Multiscale LED applied on the one dimensional Advection-Diffusion equation, switching between the propagation of the latent space dynamics for  $T_m = 450$ , and evolution of the particle dynamics for  $T_\mu = 50$ . The dimensionality of the latent dimension of the VAE is  $d_z = 1$ . The particle dynamics are correcting the error in the phase lag introduced by the iterative propagation on the latent space.

### 8.1.1 Statistical Analysis

In this section, we perform a statistical analysis to evaluate the performance of LED in forecasting the stochastic dynamics of a group of  $N = 1000$  particles whose dynamics are governed by the Advection-Diffusion equation. Starting from 20 different initial conditions, we propagate the dynamics with LED 400 different times, changing the seed up to a final time of  $T_f = 4000$ , which is equivalent to 8000 steps. Since LED is sampling from the MD decoder, every run will result to a different evolution of the configuration, as expected. For every run, we calculate the first two moments of the configuration, M1 and M2. At each timestep, we have 400 predicted M1 and M2. In order to evaluate the statistical error, we compare the predicted distributions of M1 and M2, with the groundtruth one, by evaluating their L1-Histogram error and the WD. The evolution of these errors as a function of time is plotted in Figure 19 for four variants of LED with different  $T_m$ . The initial warm-up period of LED is  $T_{warm} = 60$ . Note that as we decrease  $T_m$ , i.e. the time spent evolving the latent dynamics of LED, all error metrics decrease.

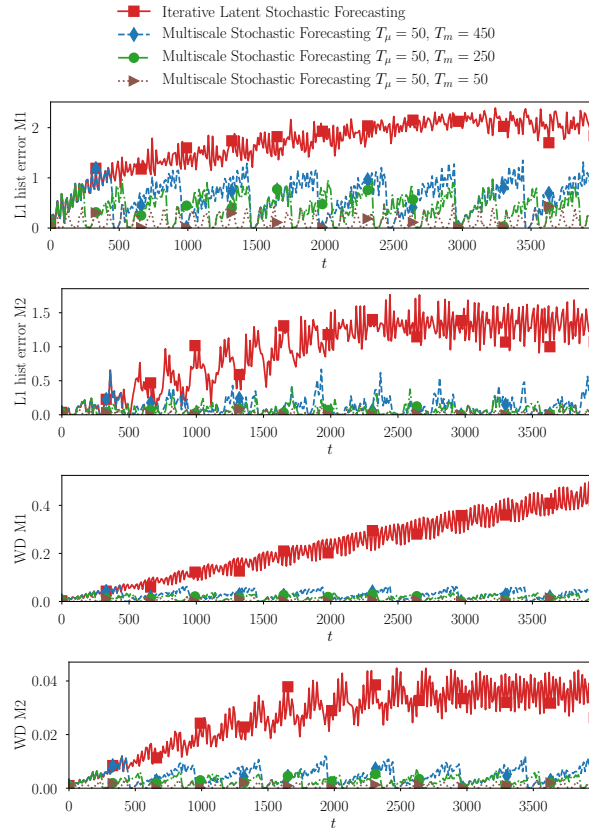


Figure 19: Starting from 20 different initial conditions, we propagate the dynamics of the Advection-Diffusion in the one dimensional space ( $d_x = 1$ ) with LED 400 different times, changing the seed up to a final time of  $T_f = 4000$ , which is equivalent to 8000 steps. For every runs, we calculate the first two moments of the configuration, M1 and M2. At each timestep, we have 400 predicted M1 and M2. We plot the statistical errors (L1-Histogram error and Wasserstein distance), between the predicted distributions of M1/M2 and the groundtruth, as function of time. The mean over all initial conditions is reported.

In Figure 20, we plot how the errors vary with respect to the ratio between the time spent in the macro dynamics (LED latent state) and the micro dynamics  $\rho = T_m/T_\mu$ . The mode where LED is propagating solely on its latent space is denoted as “Latent”. The Latent propagation exhibits the highest errors in all metrics. However, the propagation on the latent state is two orders of magnitude faster compared to the micro dynamics. This speed-up is reduced as we spent more time on the micro state, exchanging between latent propagation and micro solver dynamics (decreasing  $\rho$ ), gaining a reduction on the errors in all metrics.

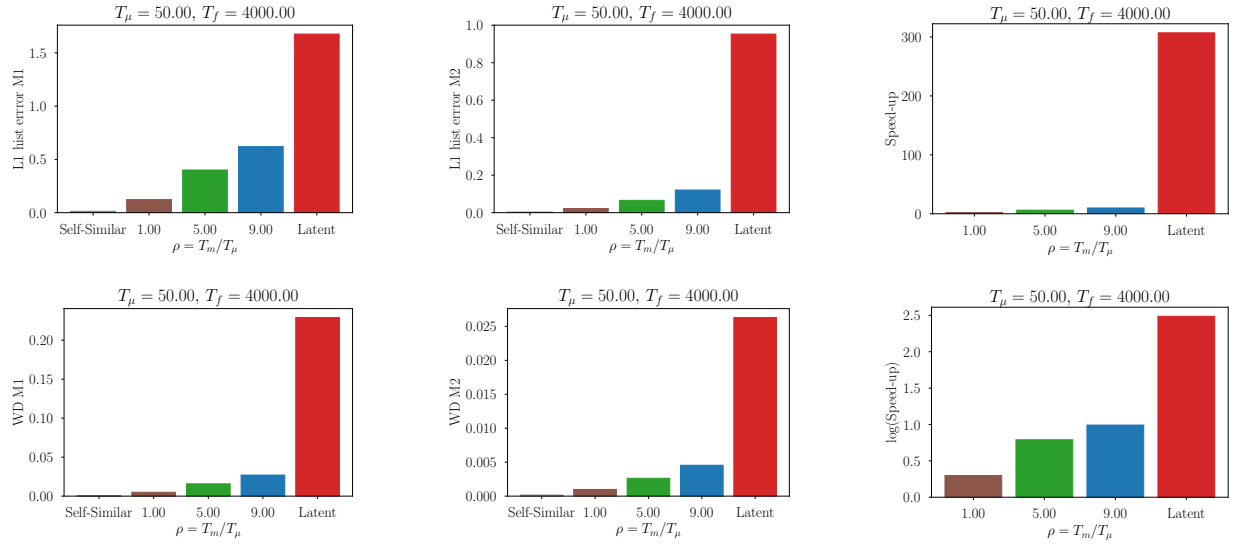


Figure 20: Starting from 20 different initial conditions, we propagate the dynamics of the Advection-Diffusion in the one dimensional space ( $d_x = 1$ ) with LED 400 different times, changing the seed up to a final time of  $T_f = 4000$ , which is equivalent to 8000 steps. For every run, we calculate the first two moments of the configuration, M1 and M2. At each timestep, we have 400 predicted M1 and M2. The bars show the mean (over time and initial conditions) statistical errors (L1-Histogram error and Wasserstein distance), between the predicted distributions of M1/M2 and the groundtruth. The self-similar error is plotted for reference [58] as errors below this level are statistically insignificant. We observe due to the iterative prediction on the latent space, the LED variant that is not evolving the dynamics on the particle level at all (denoted as “Latent”) exhibits the highest errors in all metrics. However the Latent LED is more than two orders of magnitude faster compared to the micro solver. By spending a reference time  $T_\mu$  on the fine scale dynamics (particles), we achieve a significant error reduction in all metrics, albeit at the cost of reduced speed-up. On the other hand, as the multiscale ratio  $\rho$  is increased, spending more time in the latent propagation, the errors gradually increase.

### 8.1.2 Hyperparameter Tuning

We tuned the hyperparameters of LED based on a grid search, considering the values of hyperparameters given in Table 1 for the Autoencoder, and Table 2 for the RNN.

Table 1: Autoencoder Hyperparameters for Advection-Diffusion in 1-D ( $d_x = 1$ )

Hyperparameter	Values
Number of AE layers	{5}
Size of AE layers	{100}
Activation of AE layers	$\tanh(\cdot)$
Latent dimension	{1, 2, 3, 4, 5, 6, 7, 8, 9, 10, 12, 16, 18, 22, 24, 28, 32, 64}
Residual connections	True
Variational	True/False
Permutation Invariant Layer $d_p$	{200, 1001}
Number of MD kernels $K$	{4}
Hidden units of MD decoder	{50}
Input/Output data scaling	Min-Max in [0, 1]
Noise level in the data	{0, 1, 10} (%)
Weight decay rate	{0.0, 0.0001}
Batch size	32
Initial learning rate	0.001

Table 2: LED-RNN Hyperparameters for Advection-Diffusion in 1-D ( $d_x = 1$ )

Hyperparameter	Values
Number of AE layers	{5}
Size of AE layers	{100}
Activation of AE layers	$\tanh(\cdot)$
Latent dimension	{1, 2}
Residual connections	True
Variational	True/False
Permutation Invariant Layer $d_p$	{200}
Number of MD kernels $K$	{4}
Hidden units of MD decoder	{50}
Input/Output data scaling	Min-Max in [0, 1]
Noise level in the data	{0}
Weight decay rate	{0.0001}
Batch size	32
Initial learning rate	0.001
BBTT Sequence length	{100}
Hidden state propagation length	500
RNN cell type	{lstm, gru}
Number of RNN layers	{1}
Size of RNN layers	{100}
Activation of RNN Cell	$\tanh(\cdot)$

## 8.2 Advection-Diffusion with Brownian dynamics in 3-D

In this section, we test LED on capturing the intrinsic dynamics of a set of  $N = 1000$  particles moving according to the Advection-Diffusion equations given in Equation (25) in the three dimensional space. We consider the values  $D = 0.2$ ,  $\mathbf{A} = [1, 1.5, 0.0]^T$  and  $\boldsymbol{\omega} = [0.2, 1.0, 0.5]^T$ . We solve the stochastic equations starting from a random initial condition with a timestep  $\delta t = 10^{-3}$ . By saving the positions of the particles at a coarser time-step  $\Delta t = 0.5$  and starting from different random initial conditions, we generate three datasets, a training and a validation dataset, each consisting of  $10^3$  samples, and a test dataset with  $10^4$  samples. The state of the system is given by the position of the  $N$  particles

$$\mathbf{s}_t = \begin{pmatrix} x_1^{1,t} & x_2^{1,t} & x_3^{1,t} \\ \vdots & \vdots & \vdots \\ x_1^{N,t} & x_2^{N,t} & x_3^{N,t} \end{pmatrix} \in \mathbb{R}^{N \times d_x}, \quad (26)$$

where  $x_k^{n,t}$  denotes position of particle  $n$  at time  $t$  in the  $k^{\text{th}}$  axis of the three dimensional space, while  $d_x = 3$  and  $N = 1000$ . In this case, we pick  $d_z = 8$ . We tune the hyperparameters of LED, ending up with the following architecture: the  $\phi$  function (permutation invariant layer Figure 10) consists of  $5 \times 100$  residual layers and tanh activation, the permutation invariant space has dimension  $M = 200$  with mean feature function ( $f$  in Figure 10), and the  $g$  decoder consists of a residual network with  $5 \times 100$  layers and tanh activation, reducing the dimensionality to the desired latent state of dimension  $d_z = 8$ . The decoder is a variational one and is composed of  $5 \times 100$  residual layers, and a mixture density output layer, with 50 hidden units, and 5 kernels outputting the parameters for the mixture coefficients, the means, and the covariance matrices of the 4 kernels. The RNN propagating the dynamics in the latent space, is composed of one stateful LSTM layer with 100 nodes and was trained with BBTT with a sequence length of 100. For more information on the hyperparameter tuning of the architectures the interested reader is referred to Section 8.2.2. An example of the evolution of the latent state, the errors on the first two moments, and the Wasserstein distance between the groundtruth and the predicted distribution of particle positions in an iterative prediction on the test data is shown in Figure 21a. The initial warm-up period of LED is set to  $T_{warm} = 60$ . All metrics are averaged over the three dimensions. We observe that LED captures the variance of the particle positions but due to the iterative error propagation the error on the distribution (mean and Wasserstein distance) is increasing with time.

In Figures 22a to 22c we plot the evolution of the PCA modes of the latent dynamics  $\mathbf{z}_t$  of LED. The plots are colored according to the density. As depicted clearly in Figure 22b, the latent state exhibits “meta” states, where the coarse dynamics remain for most of the time, and is iteratively jumping between them. We cluster the PCA data of the latent state, identifying six meta stable states, and identify the corresponding particle configuration for each state using the mixture density decoder in Figure 23. LED captures the distribution of the positions of the particles as depicted in Figure 22d.

In the following, we utilize multiscale forecasting, switching between latent propagation for  $T_m = 250$ , and evolution of the AD dynamics for  $T_\mu = 50$ . Note that, the initial warm-up period of LED is  $T_{warm} = 60$ . The evolution of the latent state, and the errors on the mean, the variance of the predicted particle positions, and the Wasserstein distance on their distribution in a single iterative forecast in the test dataset is given in Figure 21b. Indeed multiscale propagation alleviates the problem of iterative error propagation, and evolving the high-dimensional AD particle dynamics for  $T_\mu = 50$  is correcting the error on the statistics. In Figure 24, we plot the LED predictions of the particle configurations for selected time instants.

### 8.2.1 Statistical Analysis

We perform a statistical analysis to evaluate the performance of LED in forecasting the stochastic dynamics. Starting from 12 different initial conditions, we propagate the dynamics with LED 600 different times (different runs starting from the same initial condition), changing the seed up to a final time of  $T_f = 4000$  (equivalent to 8000 steps). Since LED is sampling from the MDN at the decoder output, every run will result to a different evolution of the configuration, as expected. For every run, we calculate the first two moments of the density of particle positions, M1 and M2 (averaged over the three dimensions). At each timestep, we have 600 predicted means and variances. In order to evaluate the statistical error, we compare the predicted distribution of M1 and M2, and the groundtruth one, by evaluating their L1-Histogram error and the WD. The evolution of these errors as a function of time is plotted in Figure 25 for four variants of LED with different  $T_m$ . LED with  $T_m = 0$  corresponding to iterative propagation in the latent space, without any evolution of the particle dynamics, and the distribution of the predicted M1 eventually diverges, although the distribution on M2 is captured accurately. By spending  $T_m = 900$  in the latent space, and  $T_\mu = 50$  in the original dynamics, we achieve a reduction of the error in the distribution of M1 as denoted by the low value of the Wasserstein metric and the lower L1-Histogram error. Note that as we decrease the time spent evolving the latent dynamics ( $T_m$ ), the errors are getting smaller in all metrics, at the cost of evolving the high dimensional particle dynamics.

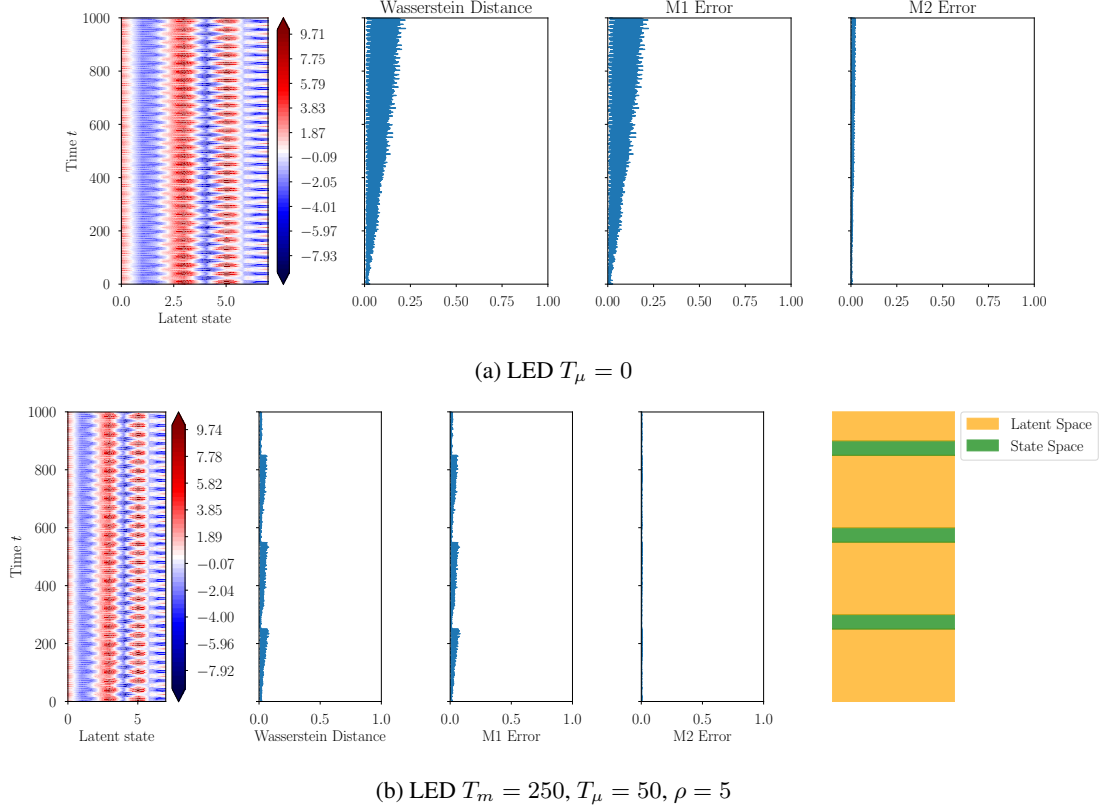


Figure 21: **(a)** LED applied on the 3-dimensional Advection-Diffusion equation, iteratively forecasting the evolution of the particles starting from an initial condition in the test data. The initial warm-up period of LED is set to  $T_{warm} = 60$ . A Variational autoencoder with a permutation invariant input layer, and a latent dimension of  $d_z = 8$  is utilized to coarse grain the high dimensional dynamics. The decoder of LED is mapping from the latent space to the particle configuration using a MD decoder. We plot the evolution of the latent state in time, along with the Wasserstein distance between the predicted and groundtruth particle distributions and the absolute error on the mean, and the standard deviation of the particle distributions. LED can forecast the evolution of the particle positions with low error, even though the total dimensionality of the original state describing the configuration of the  $N = 1000$  particles of the system is  $s_t \in 1000 \times 3$ . The network, learned an  $d_z = 8$  dimensional coarse grained representation of this configuration. However, due to the iterative prediction with LED, the error on the predicted distribution of particles is increasing with time. This can be observed at the increasing error on the estimated mean position (M1) of the particles. Nevertheless, the variance is captured along with the long-term statistical behavior. **(b)** Multiscale propagation in LED. To alleviate the iterative error propagation, the multiscale propagation is utilized with  $T_m = 250, T_\mu = 50, \rho = 5$ . Due to the iterative transition between propagation in the latent space  $z_t$  of LED for  $T_m$  and evolution of the particle dynamics describing the system state for  $T_\mu$ , the effect of iterative statistical error propagation is alleviated. Indeed, the error on the mean (M1) and standard deviation (M2) is not significantly increasing with time and the statistical long-term behavior is accurately captured.

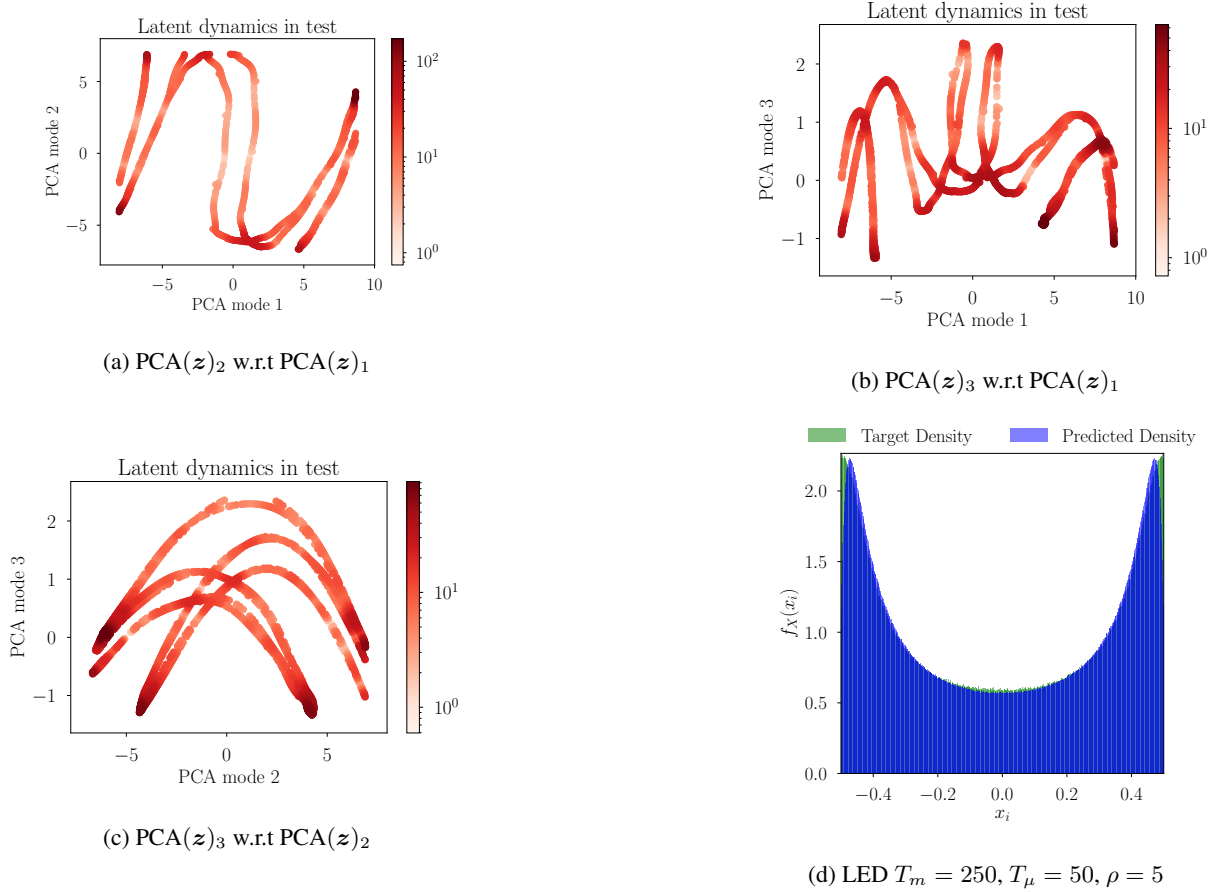


Figure 22: **(a)** Plot of the evolution of the first PCA mode of the latent state  $\mathbf{z}_t \in \mathbb{R}^{d_z}$ , with  $d_z = 8$  plotted against the second mode, where every mark is a point in time of the iterative prediction and colored according to the density. **(b)** First PCA mode against third one. **(c)** Third PCA mode against second one. **(d)** True distribution of the particle position values, and the predicted one by LED. The density of the predicted particle positions matches closely the true one.

In Figure 26 we plot the averaged statistical errors over time, demonstrating that as the ratio between macro and micro dynamics  $\rho = T_m/T_\mu$  decreases, the errors on the statistics are smaller. The LED variant that propagates solely on the latent space ( $T_\mu = 0$ ) denoted as “Latent” is almost two orders of magnitude faster than the micro scale solver. As  $\rho$  decreases, the statistical error may decrease, but this comes at the cost of reduced speed-up introduced by the evolution of the high-dimensional micro dynamics for  $T_\mu$ .

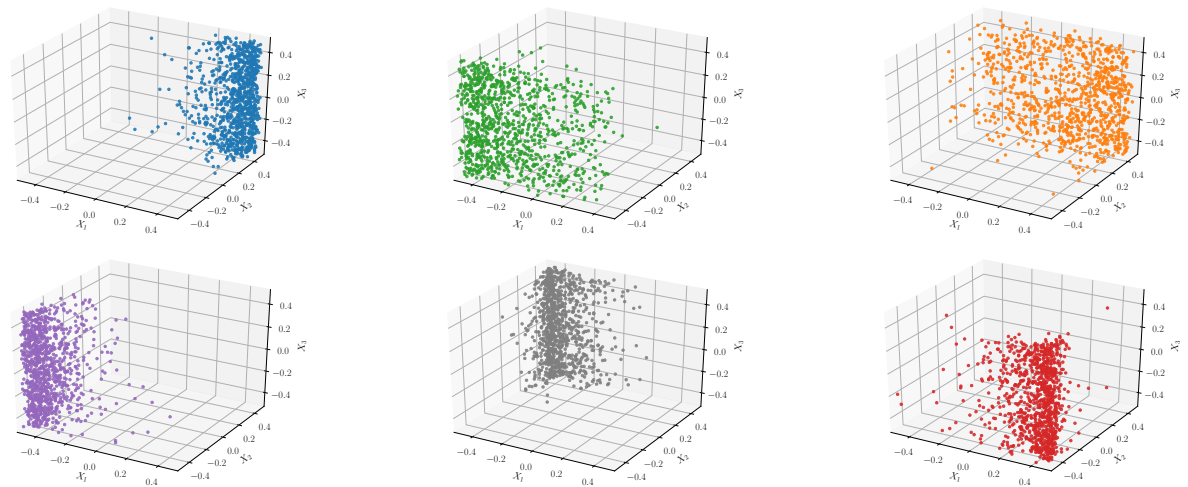
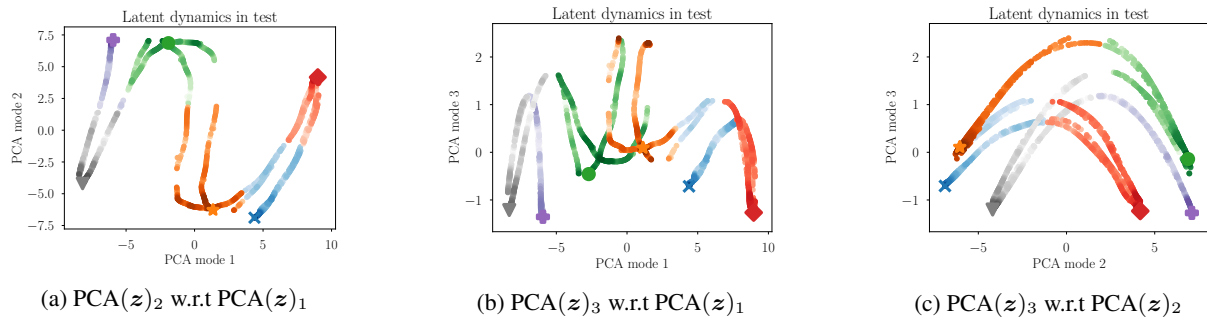


Figure 23: Spectral clustering on the PCA modes of the latent space. The six clusters correspond to different meta stable states. The particles are transitioning between these states. The corresponding particle configuration for each identified cluster in the latent space.

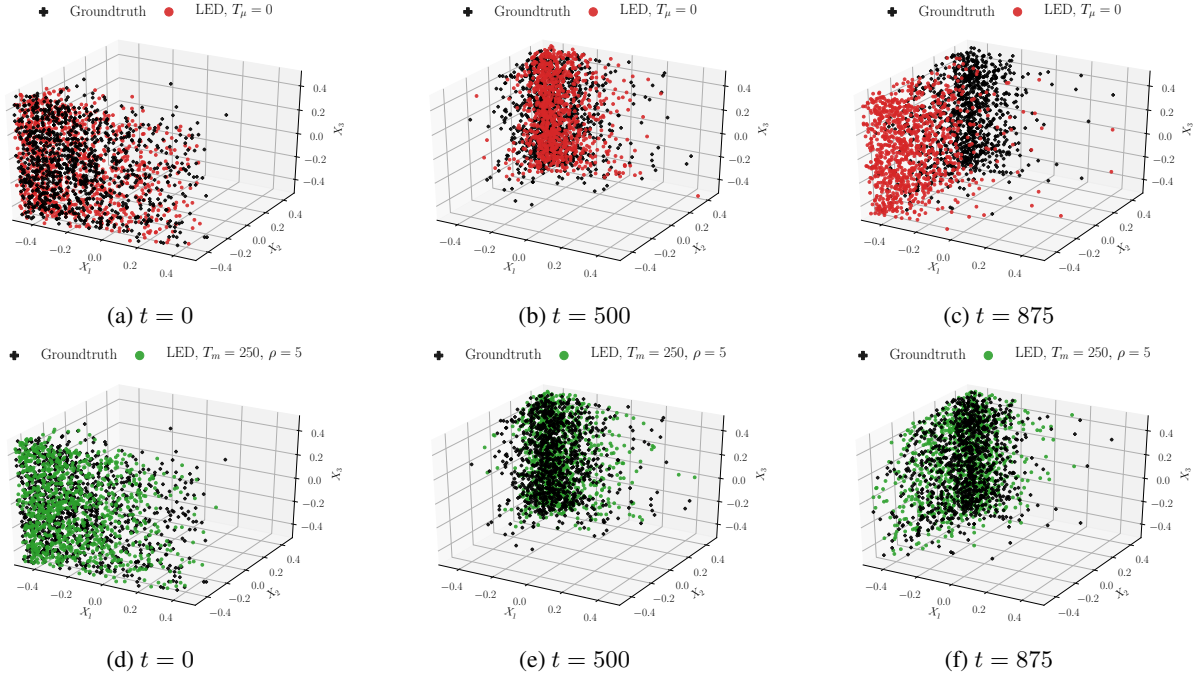


Figure 24: Starting from an initial condition from the test dataset plotted in Figure (a)  $t = 0$ , we evolve the particles of the Advection-Diffusion equation, plotting the state of the system at two later time instants (b)  $t = 500$ , and (c)  $t = 875$ . Two variants of LED with latent state dimension  $d_z = 8$  are utilized to forecast the evolution of the stochastic dynamics, one with  $T_\mu = 0$  in (a)-(c), and one with  $T_m = 250$ ,  $T_\mu = 50$ ,  $\rho = T_m/T_\mu = 5$  in (d)-(f). LED with  $T_\mu = 0$ , is not switching between propagation in the latent space and evolution of the original particle dynamics in the high dimensional state space. Due to the iterative propagation of the error, it cannot capture the state of the system at the final time  $t = 875$  as seen in Plot (c). In contrast, the iterative switching of the second variant, alleviates the problem, and the statistics are captured as seen in Plot (f). Note that the initial warm-up period of LED set to  $T_{warm} = 60$  is not visible here, the time  $t = 0$  is immediately after the warm-up period, when the iterative forecasting on the latent space starts.

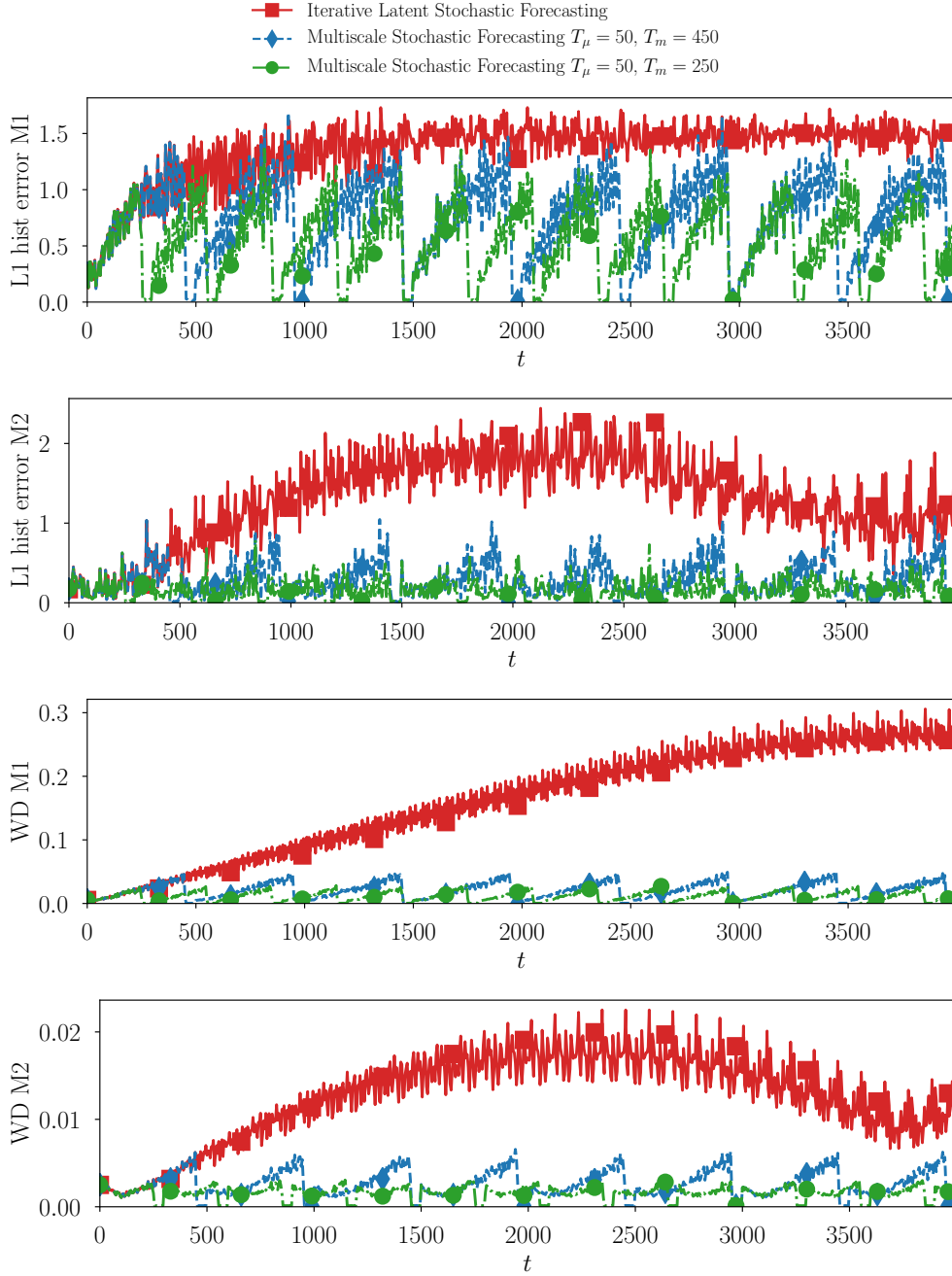


Figure 25: Starting from 12 different initial conditions, we forecast the dynamics with LED restarting from each initial condition 600 different times, changing the seed each time, up to a final time of  $T_f = 4000$  (equivalent to 8000 steps). For every run, we calculate the first two moments of the configuration, M1 and M2. At each timestep, we have 600 predicted M1 and M2. We plot the statistical errors (L1-Histogram error and Wasserstein distance), between the predicted distributions of M1/M2 and the groundtruth, as function of time. The mean over all initial conditions is reported. We observe that by iteratively switching between propagation in the LED latent state and evolution of the particle dynamics, LED can capture the statistics more accurately, at the computational cost of evolving the high-dimensional micro dynamics.

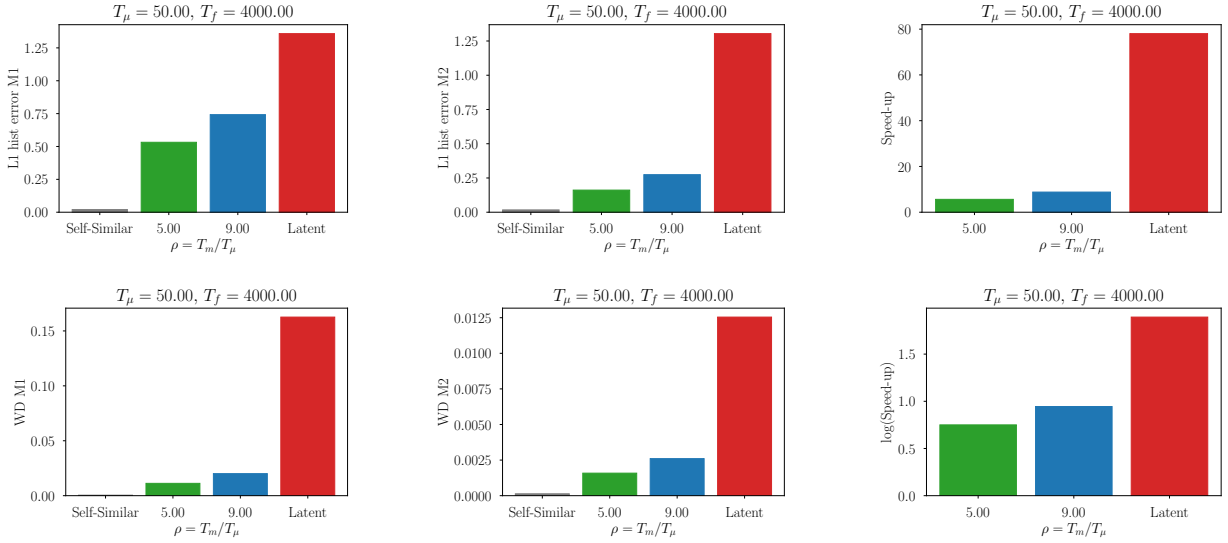


Figure 26: Starting from 12 different initial conditions, we propagate the dynamics with LED restarting from each initial condition 600 different times, changing the seed each time, up to a final time of  $T_f = 4000$  (equivalent to 8000 steps). For every run, we calculate the first two moments of the configuration, M1 and M2. At each timestep, we have 600 predicted M1 and M2. The bars show the mean (over time and initial conditions) statistical errors (L1-Histogram error and Wasserstein distance), between the predicted distributions of M1/M2 and the groundtruth. The self-similar error [58] is plotted for reference as errors below this level are statistically insignificant. We observe due to the iterative prediction on the latent space, the LED variant that is not evolving the dynamics on the particle level at all (denoted as “Latent”) exhibits the highest errors on all metrics. However, the Latent LED is two orders of magnitude faster compared to the micro solver. By spending a reference time  $T_\mu = 50$  on the fine scale dynamics (particles), we achieve a significant error reduction in all metrics, at the cost of reduced speed-up. As the multiscale ratio  $\rho = T_m/T_\mu$  is increased, spending more time in the latent propagation, the errors gradually increase.

### 8.2.2 Hyperparameter Tuning

The hyperparameters of LED are given in Table 3 for the Autoencoder, and Table 4 for the RNN.

Table 3: Autoencoder Hyperparameters for Advection-Diffusion in 3-D ( $d_x = 3$ )

Hyperparameter	Values
Number of AE layers	{5}
Size of AE layers	{100}
Activation of AE layers	$\tanh(\cdot)$
Latent dimension	{1, 2, 3, 4, 5, 6, 7, 8, 9, 10, 12, 16, 18, 22, 24, 28, 32, 64}
Residual connections	True
Variational	True/False
Permutation Invariant Layer $d_p$	{200, 1001}
Number of MD kernels $K$	{5}
Hidden units of MD decoder	{50}
Input/Output data scaling	Min-Max in [0, 1]
Noise level in the data	{0, 1, 10} (%)
Weight decay rate	{0.0, 0.00001}
Batch size	32
Initial learning rate	0.001

Table 4: LED-RNN Hyperparameters for Advection-Diffusion in 3-D ( $d_x = 3$ )

Hyperparameter	Values
Number of AE layers	{5}
Size of AE layers	{100}
Activation of AE layers	$\tanh(\cdot)$
Latent dimension	{8}
Residual connections	True
Variational	True/False
Permutation Invariant Layer $d_p$	{200}
Number of MD kernels $K$	{5}
Hidden units of MD decoder	{50}
Input/Output data scaling	Min-Max in [0, 1]
Noise level in the data	{0}
Weight decay rate	{0.0}
Batch size	32
Initial learning rate	0.001
BBTT Sequence length	{100}
Hidden state propagation length	500
RNN cell type	{lstm, gru}
Number of RNN layers	{1}
Size of RNN layers	{10, 20, 50, 100}
Activation of RNN Cell	$\tanh(\cdot)$

### 8.2.3 Generalization to Different Number of Particles

In this section, we provide additional results on the **generalization** of LED for a different **number of particles** in the simulation. Due to the permutation invariant encoder, coarse-graining the high-dimensional input of LED, we expect the network to be able to generalize to a different number of particles, since the identified coarse representation should rely on global statistical quantities, and not depend on individual positions. We utilize the network trained in configurations of  $N = 1000$  particles, to forecast the evolution of  $N = 400$  particles evolving according to the Advection-Diffusion equation. The propagation of the errors is plotted in Figure 27. The high dimensional state at three time instants as predicted by LED propagating only the latent state, and a variant with  $T_m = 50, T_\mu = 250, \rho = 5$  is plotted in Figure 28 starting from an initial condition in the test data. The initial warm-up period of LED is set to  $T_{warm} = 60$  for all variants. We observe an excellent generalization ability of the network.

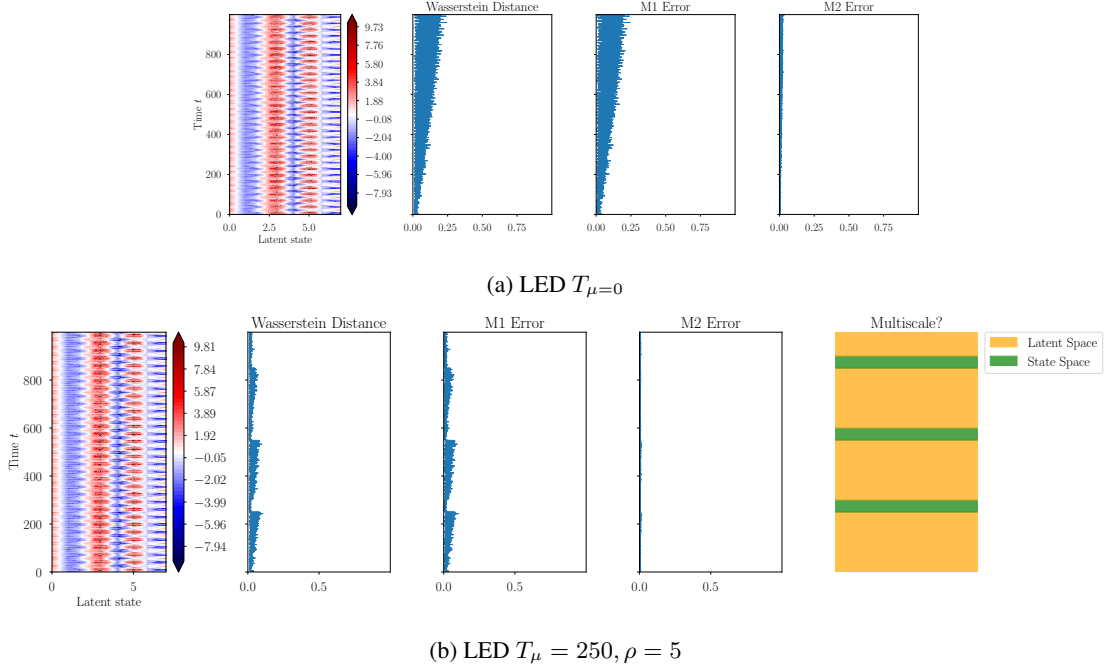


Figure 27: LED trained on particle configurations with  $N = 1000$  number of particles, learned an  $d_z = 8$  dimensional coarse grained representation of this configuration. We utilize two models with  $T_\mu = 0$  (iterative latent propagation) and  $T_\mu = 250, \rho = 5$  (multiscale forecasting) to forecast the evolution of a particle configuration composed of  $N = 400$  particles to test the generalization ability of the model. The initial warm-up period is set to  $T_{warm} = 60$ . We plot the latent space, the Wasserstein distance between the densities of the particle positions, and the error on the first two moments, for both variants of LED. We observe that the LED is able to successfully generalize to the case of  $N = 400$  particles.

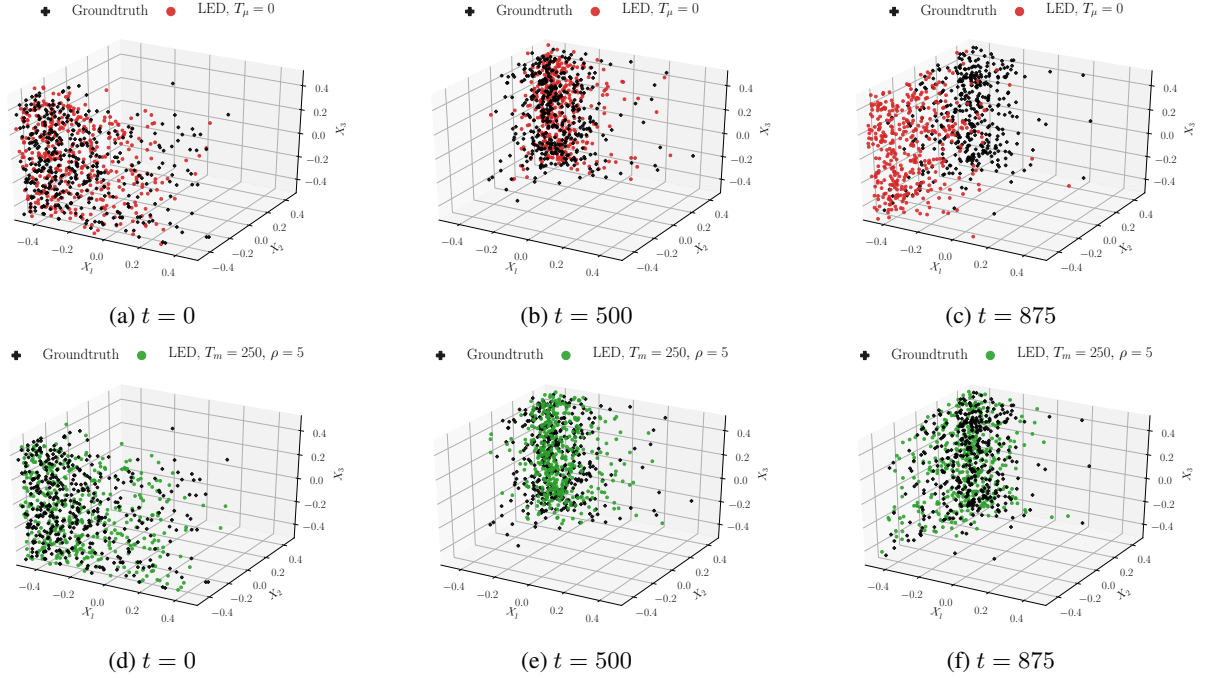


Figure 28: We employ a network trained with  $N = 1000$  particles, to forecast the evolution of  $N = 400$  particles testing the generalization ability of LED. Starting from an initial condition from the test dataset plotted in Figure (a)  $t = 0$ , we evolve the particles of the Advection Diffusion equation, plotting the state of the system at two later time instants (b)  $t = 500$ , and (c)  $t = 875$ . Two variants of LED with latent state dimension  $d_z = 8$  are utilized to forecast the evolution of the stochastic dynamics, one with  $T_\mu = 0$  in (a)-(c), and one with  $T_m = 250$ ,  $T_\mu = 50$ ,  $\rho = T_m/T_\mu = 5$  in (d)-(f). The initial warm-up period is set to  $T_{warm} = 60$  for both variants. LED with  $T_\mu = 0$ , is not switching between propagation in the latent space and evolution of the original particle dynamics in the high dimensional state space. Due to the iterative propagation of the error, it cannot capture the state of the system at the final time  $t = 875$  as seen in Plot (c). In contrast, the iterative switching of the second variant, alleviates the problem, and the statistics are captured as seen in Plot (f). Even though the network is trained on  $N = 1000$  particle configurations, it is able to generalize to different particle sizes.

### 8.2.4 Dependence on the Diffusion Coefficient

In the following study, we evaluate how the diffusion and the advection coefficient affect the efficiency of LED. We set the advection to  $\mathbf{A} = [1, 1.74, 0]^T$  and  $\omega = [0.2, 1.0, 0.5]^T$ . The amplitude of the sinusoidal advection term is thus  $|\mathbf{A}|_2 = 2$ . We utilize the dimensionless Péclet number to quantify the rate of advection by the rate of diffusion, i.e.

$$Pe = \frac{LU}{D}, \quad (27)$$

where we set the characteristic length  $L$  equal to the domain length  $L = 1$ ,  $U$  is the amplitude of the advection  $U = |\mathbf{A}|_2 = 2$ , and  $D$  the diffusion coefficient. We consider 3 different values of the Diffusion coefficient  $D \in \{0.02, 0.2, 2.0\}$ , leading to Péclet numbers  $Pe \in \{100, 10, 1\}$ . In order to select the time-step for each case, we take into account the following considerations. The velocity of each particle, has two parts, one due to the advection, and one due to diffusion. The incremental steps from each part should be much smaller than the domain length, leading to  $U\delta t \ll L$  and  $\sqrt{D\delta t} \ll L$ . The constraints on  $\delta t$  are thus  $\delta t \ll \frac{L}{U}$  and  $\delta t \ll \frac{L^2}{D}$ . As the diffusion coefficient is geometrically increased, the time-step has to be geometrically decreased to achieve the same resolution with respect to the domain size  $L$ . Based on these arguments, we chose the timesteps for the micro solver as  $\delta t \in \{10^{-2}, 10^{-3}, 10^{-4}\}$  for  $D \in \{0.02, 0.2, 2.0\}$  respectively. The LEDs considered in this study, are trained on  $10^3$  training samples (500 data points used for training and 500 for validation purposes) with a coarse time-step  $\Delta t = 1$ . The latent dimension is kept  $d_z = 8$ . The RNN of LED is composed of one LSTM layer of size 40. The rest of the hyperparameters are reported in Section 8.2.2. The results of the analysis are reported in Figure 29.

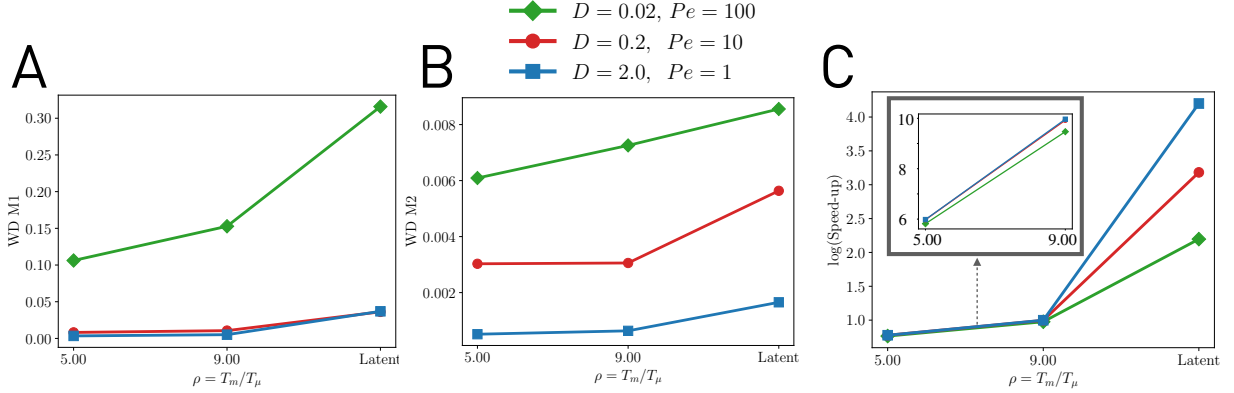


Figure 29: For each case ( $Pe \in \{100, 10, 1\}$ ), starting from a random initial condition, we propagate the dynamics with LED restarting 400 different times, changing the seed each time, up to a final time of  $T_f = 3000$  (equivalent to 3000 steps, as  $\Delta t = 1$ ). For every run, we calculate the first two moments of the configuration, M1 and M2. At each timestep, we have 400 predicted M1 and M2. We plot the mean (over time and initial conditions) statistical error (Wasserstein distance), between the predicted distributions of M1/M2 and the groundtruth. We observe that as the Péclet number increases, the errors on both distributions (M1 and M2) increase. In all cases, LED is capturing the effective dynamics of the system, as demonstrated by the low errors. Moreover, we note that the latent propagation of LED is orders of magnitude faster than the micro-scale solver. For lower Péclet numbers, the time-step needed to resolve the diffusive effects render the micro simulator computationally expensive. Thus, the computational savings by employing the latent propagation of LED are greater for lower Péclet numbers.

### 8.3 FitzHugh-Nagumo Model (FHN)

In the following, we evaluate LED in capturing the low dimensional intrinsic dynamics of the FitzHugh-Nagumo [59, 60] model (FHN) in one spatial dimension and compare its efficiency with the coarse graining approach of [49]. The FitzHugh-Nagumo model describes the governing equations of the evolution of two spatial densities, an inhibitor density  $u(x, t) = \rho^{ac}(x, t)$  and an activator density  $v(x, t) = \rho^{in}(x, t)$ . The governing equations read

$$\begin{aligned}\frac{\partial u}{\partial t} &= D^u \frac{\partial^2 u}{\partial x^2} + u - u^3 - v, \\ \frac{\partial v}{\partial t} &= D^v \frac{\partial^2 v}{\partial x^2} + \epsilon(u - \alpha_1 v - \alpha_0).\end{aligned}\quad (28)$$

The two densities evolve in different timescales, the activator density is considered the ‘‘fast’’ variable, while the inhibitor density, the ‘‘slow’’ variable. The bifurcation parameter  $\epsilon$  controls the difference in the time-scales between the two.  $D^u$  and  $D^v$  are the diffusion coefficients of the activator and the inhibitor respectively. We set the coefficients  $\alpha_0 = -0.03$  and  $\alpha_1 = 2$ . We discretize Equation (28) on the domain  $x \in [0, L]$ , with domain size  $L = 20$ , and  $N = 101$  grid points. The spatial step-size is thus,  $\delta x = L/N = 0.2$ . The diffusion coefficients of the activator and the inhibitor are set to  $D^u = 1$  and  $D^v = 4$ , respectively. We solve the equations using the Lattice Boltzmann method [61]. The interested reader is referred to Section 8.3.1 for the implementation details. The mesoscopic solution obtained by LB is considered our fine-grained solution in agreement with [49]. The time-step considered in the Lattice Boltzmann method is  $\delta t = 0.005$ , while the bifurcation parameter  $\epsilon = 0.006$ . In agreement with [49], we gather data starting from 6 different initial conditions. We subsample the data, keeping every 200<sup>th</sup> data point, leading to time-series with 451 points distant in time by  $\Delta t = 1$ . We consider 5 initial conditions for training purposes and one initial condition for testing.

In [49], a coarse graining framework is introduced, based on the identification of PDEs on the coarse-scale using either neural networks (NN), or Gaussian Processes (GP). The two variants of the method are referred to as CSPDEs-NN and CSPDEs-GP respectively. An improvement on the efficiency of the methods is achieved by augmenting the fine-scale observations from the LB solver, with features uncovered by Diffusion Maps (DM). Three features are included in [49], referred to as F1, F2 and F3 in this work. We train the LED framework with various latent state dimensions to capture

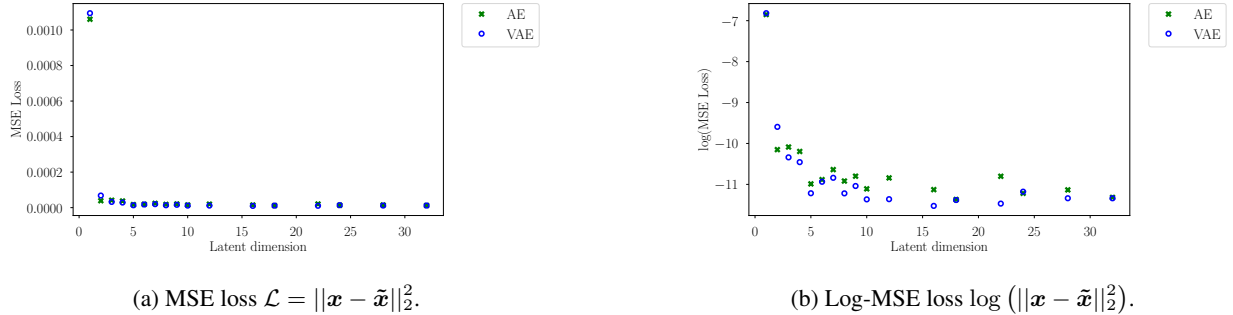


Figure 30: **(a)** MSE loss on the test data set plotted as a function of the latent state dimension. **(b)** Logarithm of the MSE loss on the test data set. We observe for both AE and VAE a latent dimension of  $d = 8$  is enough to capture most information of the data and reproduce the state evolution accurately, as the error is of the order of  $-6$  in logarithmic scale. The gain in MSE loss in using a higher latent state dimension is negligible, providing evidence that we approximately captured the dimensionality of the effective dynamics of the system.

the low order intrinsic dimensionality of the dynamics. We utilize AE and VAE with three layers of 100 nodes each. For more information on the tuned hyperparameters, refer to Section 8.3.2. The reconstruction error on the test dataset is plotted with respect to the latent state dimension in Figure 30. We find that an autoencoder with latent dimension  $d_z = 8$  is able to capture the evolution of the densities, achieving low reconstruction of the error. Further increase on the latent dimension does not lead to a significant reduction on the MSE on the reconstruction. Using the autoencoders with  $d_z = 8$ , we train the RNN. Tuning of the RNN hyperparameters is reported in Section 8.3.2. The lowest error on the validation data, was achieved by an LSTM with  $d_h = 50$  hidden nodes, using a BPTT sequence length of 30. We compare the MNAD defined in Equation (23), where  $N_T = 451$  and  $N_x = 101$ , the spatiotemporal field  $y$  is the result of the LB simulation, and  $\hat{y}$  the forecast of the models. We are considering the MNAD on both the activator and inhibitor density on the testing data. The MNAD comparison between LED and the CSPDEs [49] framework is given in Figure 31. The initial LED warm-up period is set to  $T_{warm} = 75$ . Plots of the prediction on the test data with LED are given in Figures 32 and 33.

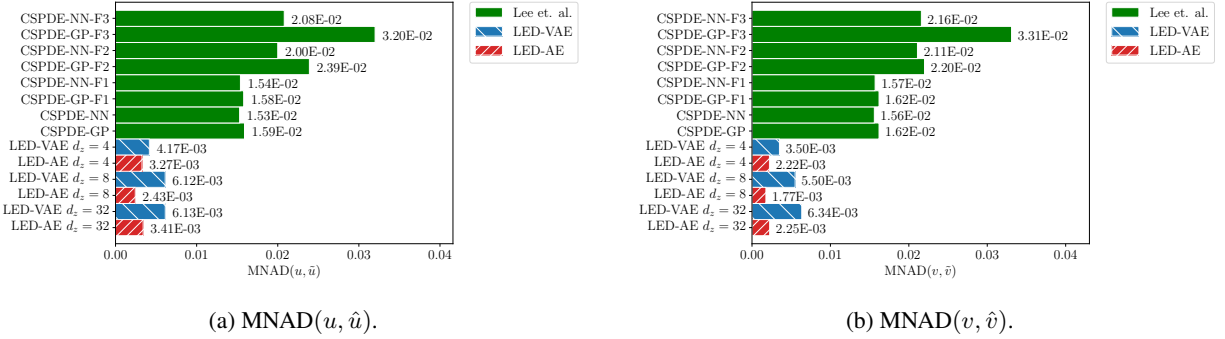


Figure 31: Comparison of LED and CSPDEs [49] models on the FHN equation, on the same testing data. **(a)** Mean normalised absolute difference (MNAD) on the activator density  $u(x, t)$ . **(b)** MNAD on the inhibitor density  $v(x, t)$ . We observe that LED outperforms all CSPDEs variants.

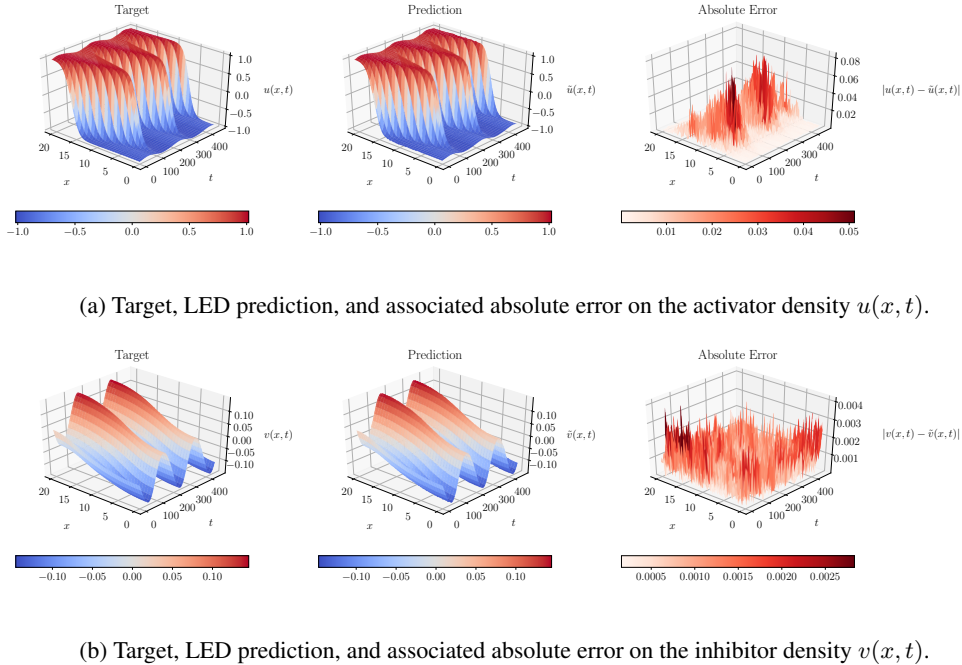
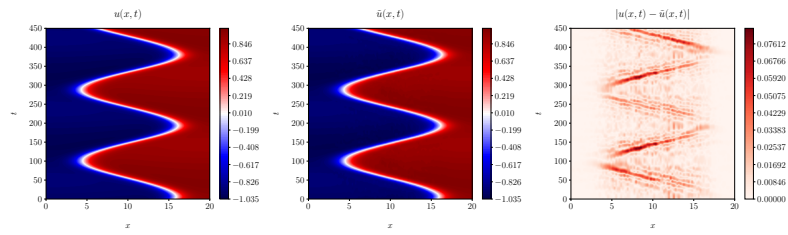
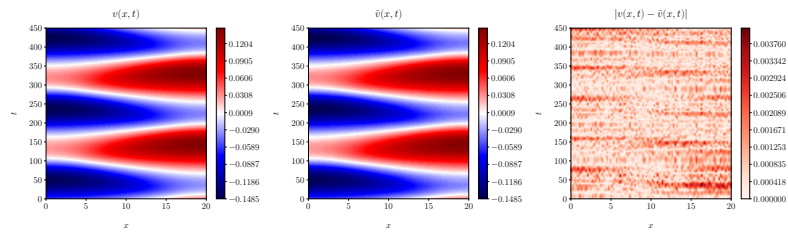


Figure 32: Surface plots of the prediction of the dynamics of the FHN equation on the test dataset using LED.



(a) Target, LED prediction, and associated absolute error on the activator density  $u(x, t)$ .



(b) Target, LED prediction, and associated absolute error on the inhibitor density  $v(x, t)$ .

Figure 33: Contour plots of the dynamics of the FHN equation on the test dataset using LED.

LED identified the intrinsic dynamics and is able to propagate them in time. This iterative propagation introduces an approximation error that accumulates over time. However, the reduced order propagation of LED can be computationally orders of magnitude less expensive compared to evolving the fine-grained dynamics. In this case the fine-grained dynamics are modeled with LB with a small time-step. We define the speed-up as  $S = T^{\text{LED}}/T^{\text{fine}}$ , where  $T^{\text{LED}}$  is the computational time needed to propagate the dynamics in one coarse time unit on average using LED, while  $T^{\text{fine}}$  is the time needed to evolve the dynamics for one coarse time unit using the LB solver on the fine scale. In the FHN we used  $\Delta t = 1$  as the coarse time scale. The speed-up achieved with LED is approximately  $S \approx 120$ , albeit at the cost of the approximation error. This speed-up can be decisive in accelerating simulations and achieving much larger time-scales. By iteratively exchanging between the coarse-grained dynamics of LED and the high-dimensional dynamics (propagation using the solver on the fine-scale) we can reduce the approximation error, at the cost of reduced speed-up. In the following, we fixed the fine scale time at  $T_\mu = 10$ . Note that the initial LED warm-up period is  $T_{\text{warm}} = 75$ . Starting from 100 different initial conditions on the test data, LED is simulated up to final time  $T_f = 8000$ , considering

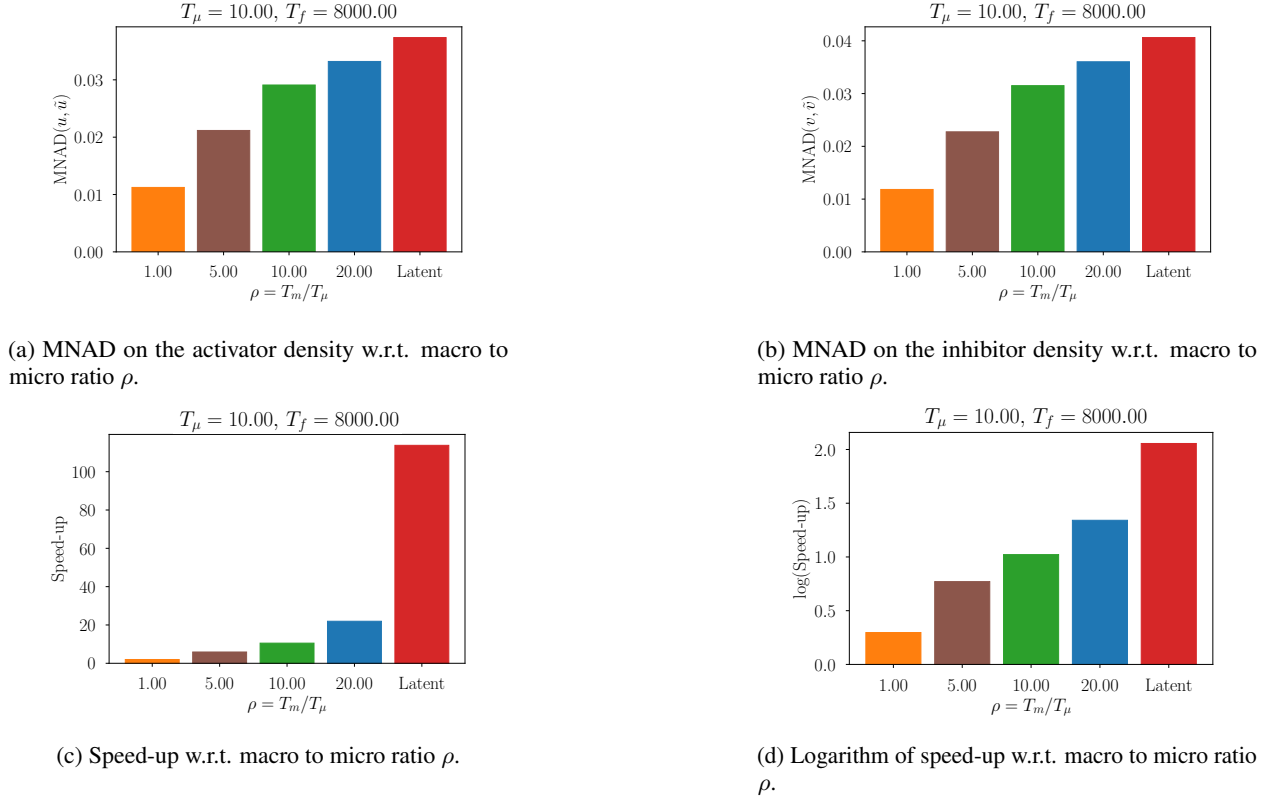


Figure 34: Starting from 100 different initial conditions in the test data, the LB method is utilized to compute the FHN dynamics up to a large horizon  $T_f = 8000$ , approximately 16 times larger than the training data. The evolution of the activator and inhibitor density obtained by the LB solver is considered as the groundtruth evolution. Using the LED framework, either with full iterative propagation on the reduced order latent space (denoted as “Latent”), or alternating between macro-dynamics for  $T_m$  and high-dimensional dynamics for  $T_\mu$ , we approximate the evolution. We fix  $T_m = 10$ . The MNAD error between the predicted and ground-truth evolution of the densities is plotted as a function of the macro-to-micro ratio  $\rho = T_m/T_\mu$  in (a) for the activator density, and (b) for the inhibitor density. In (c) the speed-up compared to the LB solver is plotted w.r.t.  $\rho$ . In (d) the logarithm of the speed-up is plotted w.r.t.  $\rho$ .

different values for the time  $T_m$  spent at the coarse level (propagating the latent dynamics of LED). The MNAD on the activator and inhibitor densities as well as the achieved speed-up depending on  $T_m$  are plotted in Figure 34. The evolution of the NAD averaged over the 100 initial conditions is plotted in Figure 35a for the activator density and in Figure 35b for the inhibitor. The results for  $T_\mu = 0$  are denoted with the label “Latent”. For  $T_m = T_\mu = 10$  ( $\rho = 1$ ), we observe that the MNAD is reduced from  $\approx 0.04$ , to  $\approx 0.01$  compared to only propagating the dynamics on the coarse scale in both the activator and inhibitor densities. However, the speed-up is reduced from  $S \approx 120$  to  $S \approx 2$ . By increasing  $T_m \in \{50, 100, 200\}$ , we get the intermediate regimes between propagation of the computationally expensive (and possibly intractable) high-dimensional system dynamics, and the full iterative propagation. As we

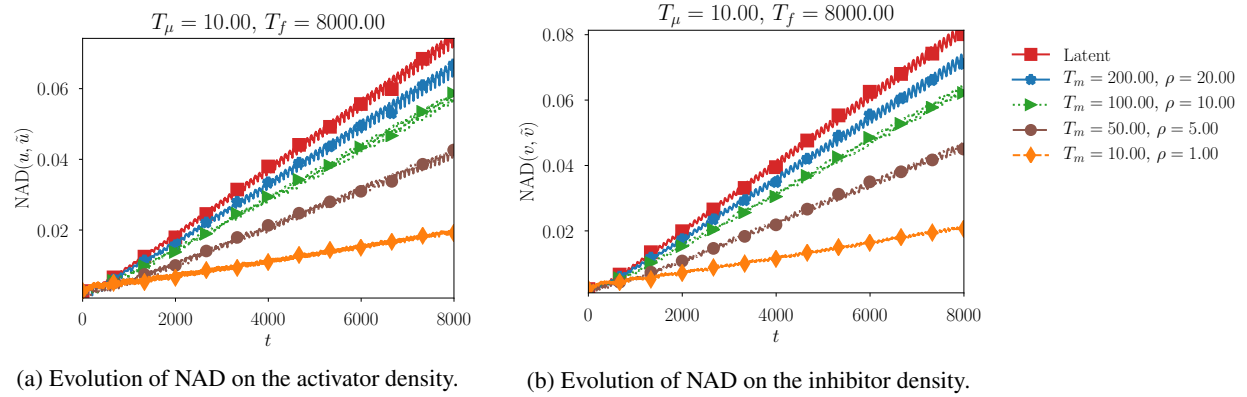


Figure 35: Evolution of the normalized absolute error (NAD) as a function of time, for different values of the macro to micro ratio  $\rho$ . Average over 100 different initial conditions from the test data is reported.

increase  $T_m$  (increase  $\rho$ ), the speed-up is increased, as we are using more and more the reduced order dynamics, albeit at the cost of an increasing error.

### 8.3.1 Lattice Boltzman on FitzHugh-Nagumo model (FHN)

In this section we briefly describe the Lattice Boltzmann [61] method utilized to obtain data from the FitzHugh-Nagumo model (FHN). In our study, the data from the meso-scale LB method are considered the high-dimensional fine-grained dynamics. The FHN system is described by the equations:

$$\begin{aligned}\frac{\partial u}{\partial t} &= D^u \frac{\partial^2 u}{\partial x^2} + u - u^3 - v, \\ \frac{\partial v}{\partial t} &= D^v \frac{\partial^2 v}{\partial x^2} + \epsilon(u - \alpha_1 v - \alpha_0),\end{aligned}\tag{29}$$

where we denote with  $u(x, t) = \rho^{ac}(x, t)$  the density of the activator and  $v(x, t) = \rho^{in}(x, t)$  the density of the inhibitor, while the dependency of  $u$  and  $v$  on  $x$  and  $t$  is omitted from Equation (29) for brevity.  $D^u$  and  $D^v$  are the diffusion coefficients of the activator and the inhibitor respectively. We set the coefficients  $\alpha_0 = -0.03$  and  $\alpha_1 = 2$ . The bifurcation parameter  $\epsilon = 0.006$  controls the difference in the time-scales between the activator and the inhibitor. The domain considered in this study is  $x \in [0, L]$ , with domain size  $L = 20$ , and  $N = 101$  grid points. The step-size is thus,  $\delta x = L/N = 0.2$ . The diffusion coefficients of the activator and the inhibitor are set to  $D^u = 1$  and  $D^v = 4$ , respectively. The time-step considered in the Lattice Boltzmann method is  $\delta t = 0.005$ , while the bifurcation parameter  $\epsilon = 0.006$ . The discrete-velocity distribution functions  $f_i^u$  and  $f_i^v$  (also called particle populations), that describe the mesoscopic LB system are given by

$$f_i^u(x_j + i\delta x, t_{k+1}) = f_i^u(x_j + i, t_{k+1}) = f_i^u(x_j, t_k) + \Omega_i^u(x_j, t_k) + R_i^u(x_j, t_k),\tag{30}$$

$$f_i^v(x_j + i\delta x, t_{k+1}) = f_i^v(x_j + i, t_{k+1}) = f_i^v(x_j, t_k) + \Omega_i^v(x_j, t_k) + R_i^v(x_j, t_k),\tag{31}$$

where in our work we consider the discrete velocities  $c_i \in \{-1, 0, +1\}$  in the one dimensional domain (D1Q3 velocity set). The indexes  $i \in \{-1, 0, 1\}$  denote the particle populations of each velocity. The densities for the activator and the inhibitor are given by:

$$u(x_j, t_k) = \sum_{i=-1}^1 f_i^u(x_j, t_k), \quad v(x_j, t_k) = \sum_{i=-1}^1 f_i^v(x_j, t_k).\tag{32}$$

The reaction terms are given by:

$$R_i^u(x_j, t_k) = \frac{1}{3} \Delta t (u(x_j, t_k) - u(x_j, t_k)^3 - v(x_j, t_k)),\tag{33}$$

$$R_i^v(x_j, t_k) = \frac{1}{3} \Delta t \epsilon (u(x_j, t_k) - \alpha_1 v(x_j, t_k) - \alpha_0).\tag{34}$$

Following [49], the collision terms are given by the Bhatnagar-Gross-Krook (BGK) model:

$$\Omega_i^u(x_j, t_k) = -\omega_i^u (f_i^u(x_j, t_k) - f_i^{u, equil}(x_j, t_k)),\tag{35}$$

$$\Omega_i^v(x_j, t_k) = -\omega_i^v (f_i^v(x_j, t_k) - f_i^{v, equil}(x_j, t_k)),\tag{36}$$

$$\tag{37}$$

where the equilibrium densities are set to

$$f_i^{u, equil}(x_j, t_k) = \frac{1}{3} u(x_j, t_k), \quad f_i^{v, equil}(x_j, t_k) = \frac{1}{3} v(x_j, t_k),\tag{38}$$

based on spatially uniform Local diffusion equilibrium, for which the velocity distributions are homogeneous in all velocity directions. Moreover, the BGK relaxation coefficients are given by

$$\omega_i^u = \frac{2}{1 + 3D^u \frac{\Delta t}{\Delta x^2}}, \quad \omega_i^v = \frac{2}{1 + 3D^v \frac{\Delta t}{\Delta x^2}}.\tag{39}$$

In order to generate the training, validation and testing data, we solve the dynamics up to  $T_f = 450$ , with a time-step  $\delta t = 0.005$  starting from different initial conditions. For the training data set we consider 3 initial conditions, for the validation dataset 2 and one initial condition for testing. The initial conditions are plotted in Figure 36. For the LB method, in order to initialize the particle densities we employ an equal weight rule according to [49] at each grid point  $x_n$  according to:

$$f_{-1}^u(x_n, t=0) = f_0^u(x_n, t=0) = f_{+1}^u(x_n, t=0) = \frac{u(x_n, t=0)}{3},\tag{40}$$

$$f_{-1}^v(x_n, t=0) = f_0^v(x_n, t=0) = f_{+1}^v(x_n, t=0) = \frac{v(x_n, t=0)}{3}.\tag{41}$$

As discussed in [49] this equal weight choice is not in general consistent with the FHN PDE equation, which is not spatially uniformly and simply diffusive. However, we expect that after an initial relaxation period, the fine scale simulation features will become slaved to the local concentration field. For this reason, starting from all initial conditions, we start collecting data after an initial transient period of  $T = 2$  time units.

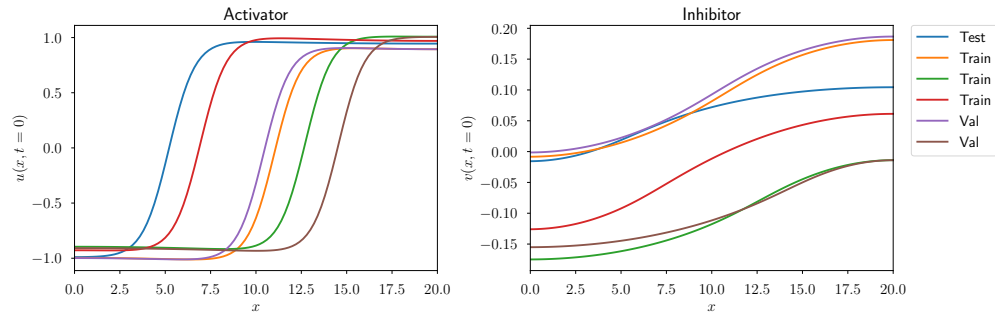


Figure 36: The initial conditions for the activator  $u(x, t)$  and inhibitor  $v(x, t)$  density of the FHN model. Three runs starting from three different initial conditions are used for training the network, two for validation purposes and one for testing the predictive performance.

### 8.3.2 Hyperparameters

The hyperparameters utilized to tune the autoencoder of LED are given in Table 5. The hyperparameters for the RNN are given in Table 6.

Table 5: Autoencoder Hyperparameters for FHN

Hyperparameter	Values
Number of AE layers	{3}
Size of AE layers	{100}
Activation of AE layers	$\tanh(\cdot)$
Latent dimension	{1, 2, 3, 4, 5, 6, 7, 8, 9, 10, 12, 16, 18, 22, 24, 28, 32, 64}
Residual connections	True
Variational	True/False
Input/Output data scaling	$\mathcal{N}(0, 1)$
Noise level in the data	{0, 1, 10} (%)
Weight decay rate	{0.0, 0.0001}
Batch size	32
Initial learning rate	0.001

Table 6: LED-RNN Hyperparameters for FHN

Hyperparameter	Values
Number of AE layers	{3}
Size of AE layers	{100}
Activation of AE layers	$\tanh(\cdot)$
Latent dimension	{4, 8, 32, 64}
Residual connections	True
Variational	True/False
Input/Output data scaling	$\mathcal{N}(0, 1)$
Noise level in the data	{0, 1, 10}
Weight decay rate	{0.0, 0.0001}
Batch size	32
Initial learning rate	0.001
BPTT Sequence length	{30, 60}
Hidden state propagation length	300
RNN cell type	{lstm, gru}
Number of RNN layers	{1}
Size of RNN layers	{50, 100, 200, 400}
Activation of RNN Cell	$\tanh(\cdot)$

## 8.4 Kuramoto-Sivashinsky

The Kuramoto-Sivashinsky (KS) equation [63, 64] is a prototypical spatially extended partial differential equation (PDE) of fourth order that exhibits a very rich range of nonlinear phenomena and is studied extensively as a prototypical model of turbulence. In this section, we demonstrate that LED can be easily adapted to learn the effective dynamics on the inertial manifold in a similar fashion, without making any underlying assumptions about the nature of the PDE (translation invariance, energy conservation loss, etc.). Moreover, iterative forecasting the long-term dynamics with data-driven methods such as the one proposed in [23], can lead to periodic orbits, stable attractors, or other spurious dynamics, not present in the training data [47]. We demonstrate that by utilizing the multiscale approach explained in Section 6.6 we can reproduce the long-term climate and lower the errors on the distribution of the predicted state values.

In this work, we consider the one dimensional K-S equation given by the PDE

$$\frac{\partial u}{\partial t} = -\nu \frac{\partial^4 u}{\partial x^4} - \frac{\partial^2 u}{\partial x^2} - u \frac{\partial u}{\partial x}, \quad (42)$$

on the domain  $\Omega = [0, L]$  with periodic boundary conditions  $u(0, t) = u(L, t)$  and  $\nu = 1$ . The dimensionless boundary size  $\tilde{L} = L/(2\pi)$  directly affects the dimensionality of the attractor. For large values of  $\tilde{L}$ , the attractor dimension scales linearly with  $\tilde{L}$ . In this work, we consider the case  $L = 22$ , corresponding to  $\tilde{L} = L/(2\pi) \approx 3.5014$  studied extensively in [65] exhibiting a structurally stable chaotic attractor, i.e. an inertial manifold where the long-term dynamics lie.

In order to spatially discretize Equation (42) we select a grid size  $\Delta x$  with  $D = L/\Delta x + 1 = 64$  the number of nodes. Further, we denote with  $u_i = u(i\Delta x)$  the value of  $u$  at node  $i \in \{0, \dots, D - 1\}$ . We discretize Equation (42) and solve it using the fourth-order method for stiff PDEs introduced in [66] with a time-step of  $\delta t = 0.025$  starting from a random initial condition. After discarding initial transients, we subsample the data keeping every tenth datapoint, to obtain a dataset where samples are distanced by  $\Delta t = 0.25$  in time (coarse time unit). We use  $5 \cdot 10^3$  such samples for training and another  $5 \cdot 10^3$  for validation. For testing purposes (long-term forecasting), we repeat the process with a different random seed, generating another  $10^5$  samples. The largest Lyapunov exponent is computed as  $\Lambda_1 = 0.048$ , leading to a Lyapunov time of  $T^{\Lambda_1} = 1/\Lambda_1 = 20.83$ .

We tried both VAE and AE, and we tuned the noise level, weight decay rate, the size and number of layers of the autoencoders. For more information on the combinations tried out, the interested reader can refer to Section 8.4.3. The MSE error on the test data is plotted in Figure 37. Using more than  $d_z = 8$  nodes on the latent space, improves the quality of the reconstruction only by a very small margin in the order of  $-6$  in the logarithmic scale. For both AE and VAE a latent dimension of  $d_z = 8$  is enough to capture most information of the data and reproduce the state evolution accurately, as the error is of the order of  $-6$  in logarithmic scale. Note that we are not yet propagating the dynamics, as the autoencoder learned only to encode the data. The evolution though, can be accurately represented in this  $d_z = 8$  dimensional reduced order space learned by the AE/VAE. Among the trained autoencoders with latent dimension  $d_z = 8$ , we pick the one with the lowest MSE error on the validation data set, and couple it with an RNN forecasting the latent dynamics. We tune the hyperparameters of the RNN (see Section 8.4.3). We found that an AE with an encoder and a decoder of 5 layers of size 50 each, trained with additional noise level  $k = 10\%$ , and weight decay rate of 0.0001 (the weight decay is not taken into account in the RNN training, but only in the AE training), with a GRU cell of size 200, trained with a BPTT sequence length of 125 provided the smallest error on the statistics of the state evolution (distribution of the predicted states as compared to the true ones, and their power spectrum).

Using the trained RNN we can evolve the dynamics on the reduced order space. An iterative prediction of LED (solely propagating on the latent space) is illustrated in Figure 38. The initial LED warm-up period is set to  $T_{warm} = 60$ . We observe visually that the predictions do not deviate, which is a classical problem in iterative forecasting [47], while the long-term climate is reproduced. Quantitative results on the power spectrum of the predicted state evolution, and the density of the state are provided in Figure 41. LED can effectively learn and propagate the dynamics on the reduced order manifold capturing the long-term behavior.

### 8.4.1 Multiscale Analysis

Two variants of LED switching between propagation in the latent state of the RNN for  $T_m$  (macro dynamics) and the micro solver for  $T_\mu$  are given in Figure 39 and Figure 40. In both cases, we visually observe that the long-term climate of the system is reproduced. In the following, we plot the NAD error, we quantify the error between the distribution of the state values of the micro solver and the LED variants, and report the speed-up of LED compared to the micro solver in Figure 42.

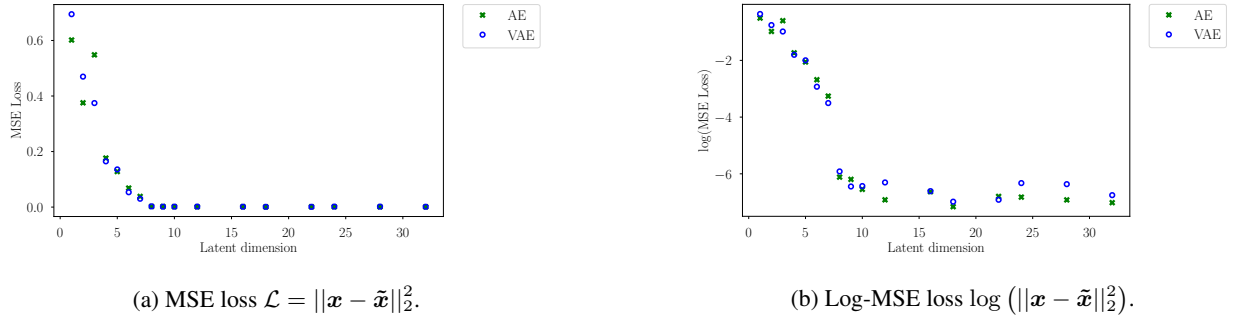


Figure 37: **(a)** MSE loss on the test data set plotted as a function of the latent state dimension. **(b)** Logarithm of the MSE loss on the test data set. We observe for both AE and VAE a latent dimension of  $d_z = 8$  is enough to capture most information of the data and reproduce the state evolution accurately, as the error is of the order of  $-6$  in logarithmic scale. The gain in MSE loss in using a higher latent state dimension is negligible, providing evidence that we approximately captured the dimensionality of the effective dynamics of the system.

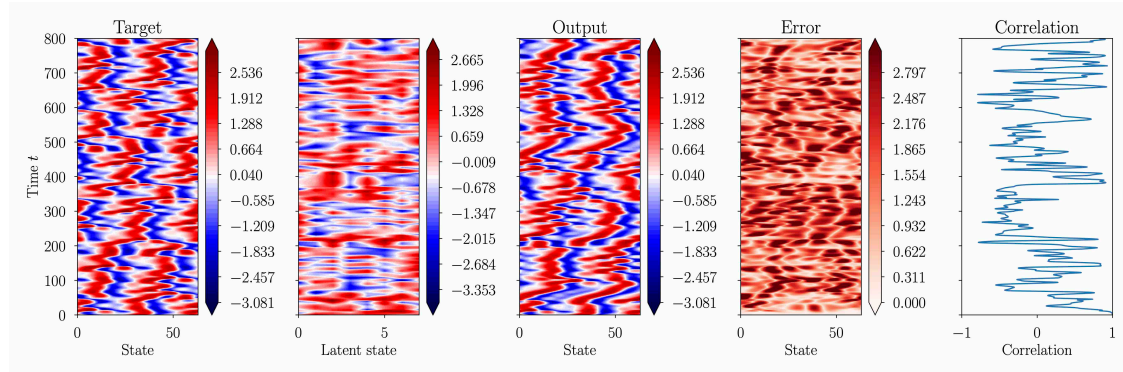


Figure 38: An iterative forecast on the test data set using LED propagating the dynamics on an  $d_z = 8$  dimensional latent space. LED is not switching to the micro scale ( $T_\mu = 0$ ). The initial LED warm-up period is  $T_{warm} = 60$ .

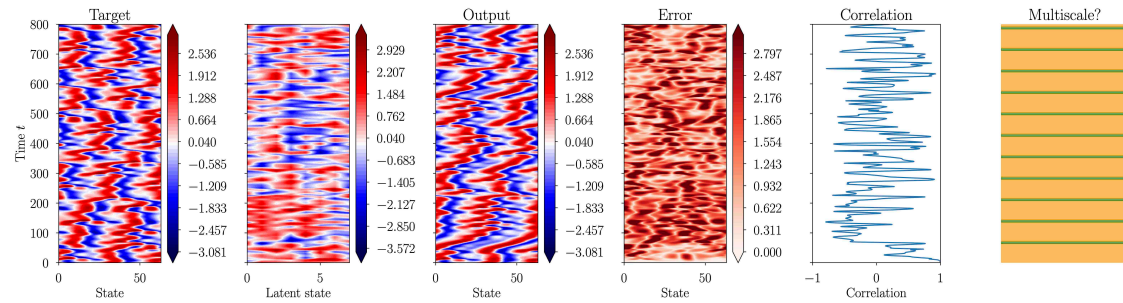


Figure 39: LED switching between propagation of the latent dynamics (macro scale with  $d_z = 8$ ) for  $T_m = 64$  and micro dynamics for  $T_\mu = 8$ . The relative ratio is  $\rho = 8$ .

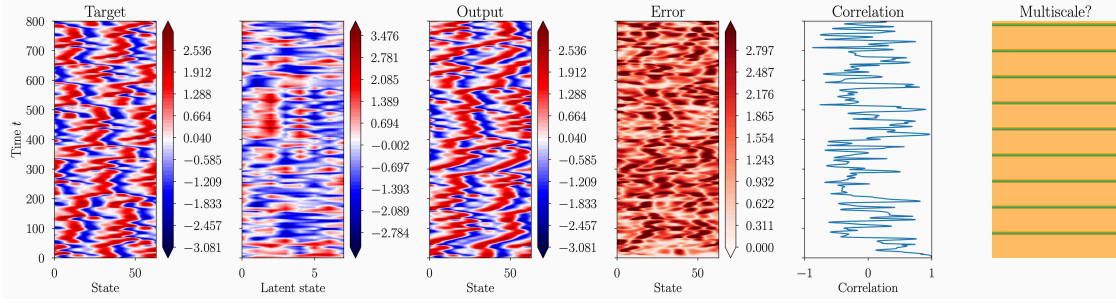


Figure 40: LED switching between propagation of the latent dynamics (macro scale with  $d_z = 8$ ) for  $T_m = 80$  and micro dynamics for  $T_\mu = 8$ . The relative ratio is  $\rho = 10$ .

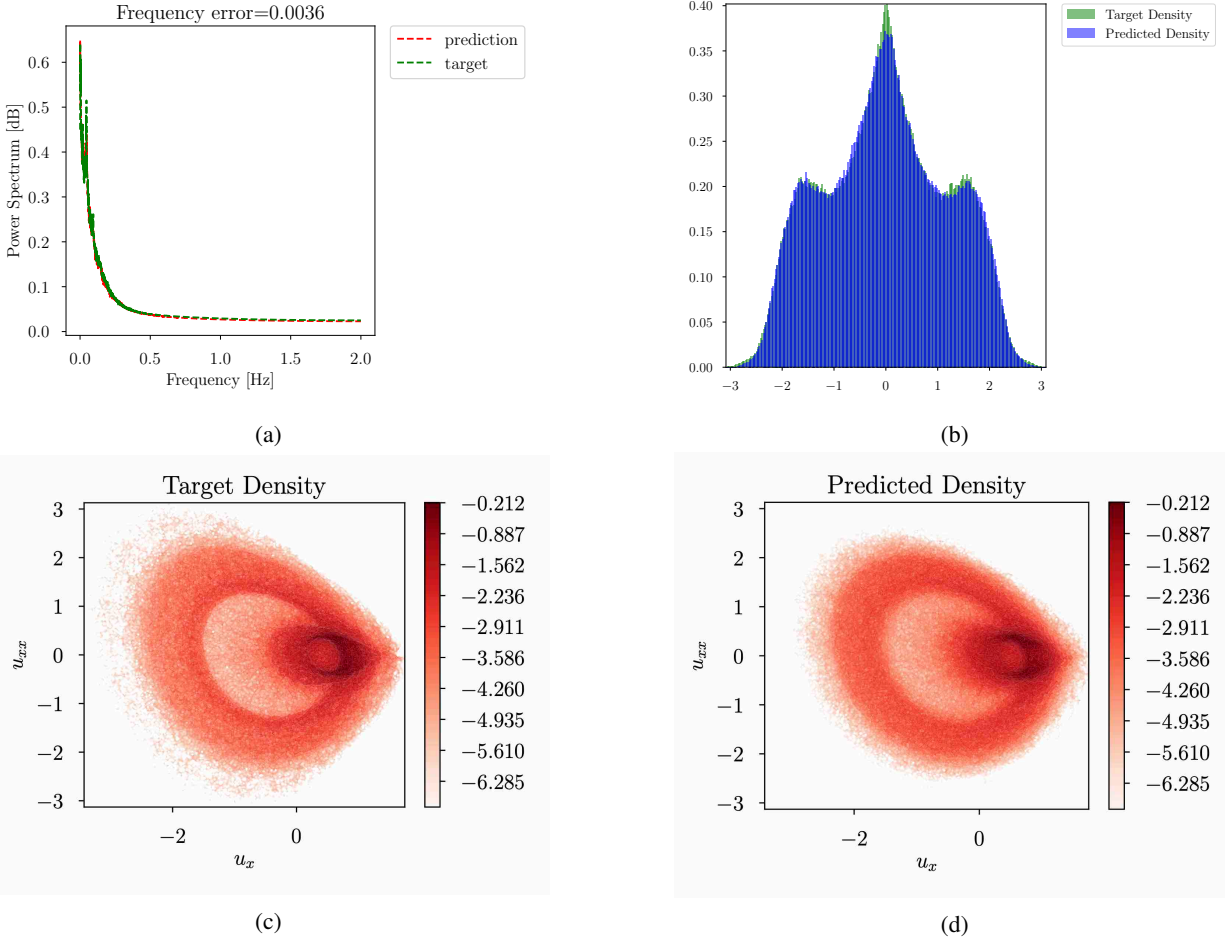
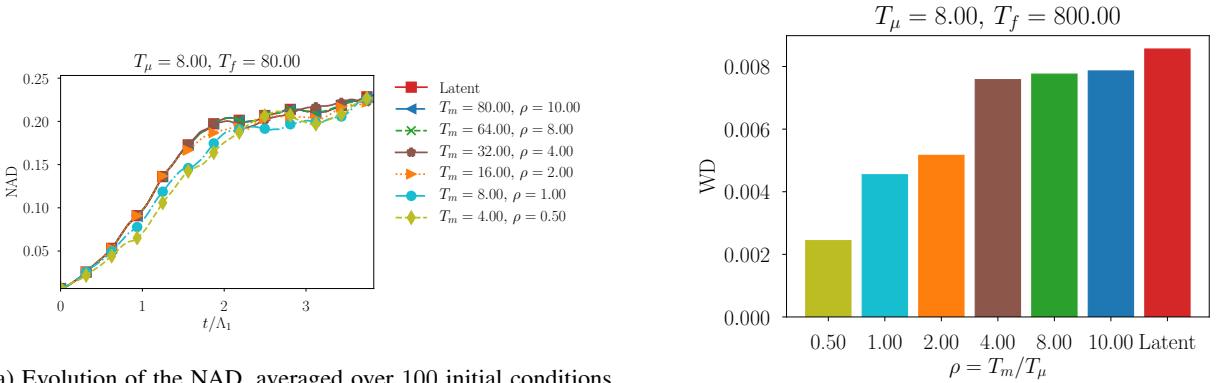
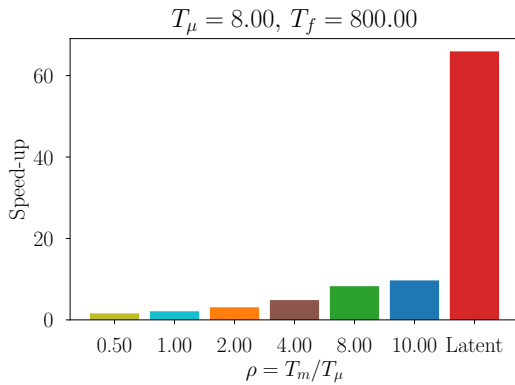


Figure 41: **(a)** The predicted power spectrum plotted against the true one. **(b)** The distribution of the predicted state  $u$  values plotted against the correct distribution. The two distributions match. Plot of the density of values in the  $u_x - u_{xx}$  space obtained from **(c)** the groundtruth trajectories and **(d)** the predicted ones. Even though the LED is propagating the dynamics on a low order  $d_z = 8$  dimensional space (after an initial warm-up period  $T_{warm} = 60$ ), the statistics of the system, or long-term climate, is reproduced accurately, as demonstrated by the power spectrum, the state distribution of the predictions and the dynamics of the  $u_x - u_{xx}$  density plot.

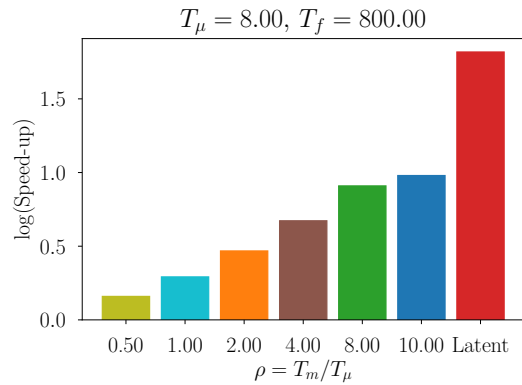


(a) Evolution of the NAD, averaged over 100 initial conditions from the test data.

(b) WD on the state distribution w.r.t. macro to micro ratio  $\rho$ .



(c) Speed-up w.r.t. macro to micro ratio  $\rho$ .



(d) Log of the speed-up w.r.t. macro to micro ratio  $\rho$ .

Figure 42: Results of LED on the Kuramoto-Sivashinsky equation. Starting from 100 different initial conditions from the test data, we utilize LED with  $T_\mu = 0$ , and 6 variants switching between evolution of the dynamics based on the spectral solver for  $T_\mu = 8$ , and propagation of the latent space in LED for  $T_m$ , with different values of  $T_m$  for each variant. Unless  $\rho$  drops to  $\rho = 0.5$ , no significant drop in the NAD or the WD on the state distribution is observed, while at this multiscale ratio, the speed-up is negligible. This may be attributed to the chaotic nature of the Kuramoto-Sivashinsky equation, where even a small initial error propagates exponentially. Nevertheless, the NAD error is under 0.1 for at least one Lyapunov time  $1/\Lambda_1$  for LED variants and the state distribution is captured as demonstrated by the low WD errors on the state distributions, even though LED is utilizing a latent space with dimension 8 and being almost two orders of magnitude faster than the spectral solver (micro scale).

### 8.4.2 Principal component analysis

The dynamics of the Kuramoto-Sivashinsky equation with  $L = 22$  mostly take place on an 8 dimensional manifold [65]. By performing Principal Component Analysis (PCA), we indeed see that 99.8% of the total energy can be captured with the first 8 most energetic PCA modes. The energy distribution is shown in Figure 43. The dynamics can be represented in an 8 dimensional space in the PCA basis, while the statistics of the system are captured correctly as shown in Figure 44, where the reconstructed evolution  $\mathbf{u}_{rec}(t)$  using only the 8 most energetic PCA modes closely matches the ground-truth  $\mathbf{u}(t)$ . However, the transformation to the PCA basis is static, i.e. the PCA transformation does not take into account the dynamics on the reduced order manifold, i.e. how predictable the evolution of the reduced order modes is. Indeed, utilizing the LED-VAE, the reconstruction error is smaller as depicted in Figure 45.

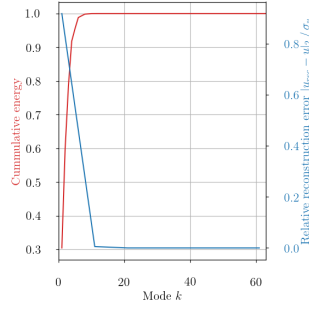


Figure 43: The energy of the Principal Components of the Kuramoto-Sivashinsky equation with  $L = 22$ . The 8 most energetic modes contain approximately 99.8% of the total energy.

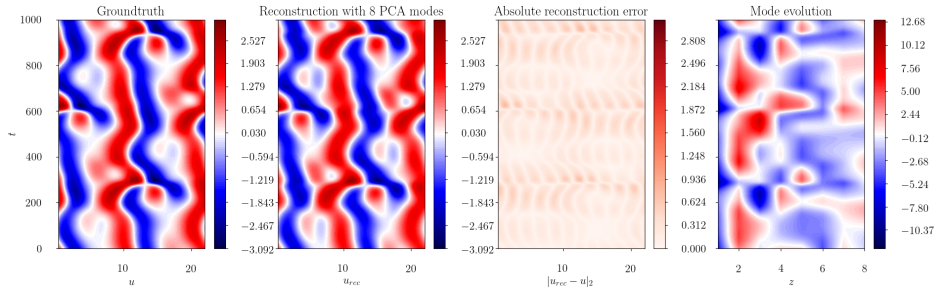


Figure 44: The evolution of a trajectory  $\mathbf{u}(t)$  in the state space of the Kuramoto-Sivashinsky equation with  $L = 22$ . The reconstruction of the trajectory  $\mathbf{u}_{rec}(t)$  using only the first 8 most energetic PCA modes, along with the reconstruction error  $|\mathbf{u} - \mathbf{u}_{rec}(t)|_2$  and the evolution of these 8 modes  $\mathbf{z}(t)$ .

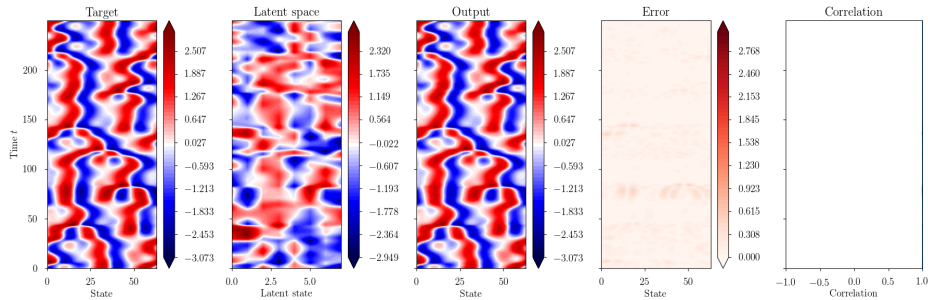


Figure 45: The evolution of a trajectory  $\mathbf{u}(t)$  in the state space of the Kuramoto-Sivashinsky equation with  $L = 22$ . The reconstruction of the trajectory  $\mathbf{u}_{rec}(t)$  using a VAE that first compresses the input to a latent space with dimension 8 and then projects back to the original space. The long-term statistics can be represented in this low dimensional manifold, while the error is smaller compared to PCA.

### 8.4.3 Autoencoder Hyperparameter Study

In this section, we provide the results of a hyperparameter study we conducted on the Autoencoder on the Kuramoto-Sivashinsky equation. We trained the network with  $10^4$  samples, half of them used for training and half for validation. All hyperparameter combinations we tried are given in Table Table 7. We found that VAE/AE with 5 layers and 50 units, equipped with residual connections and tanh activation function consistently provided better results in terms of the MSE loss in the test data compared to other combinations. For this reason, during the search for the optimal hyperparameters for the LED architecture, where we further need to optimize the hyperparameters of the RNNs, we restrict ourselves to the combinations reported in Table 8.

Table 7: Autoencoder Hyperparameters for Kuramoto-Sivashinsky

Hyperparameter	Values
Number of AE layers	{4, 5, 6, 7}
Size of AE layers	{50, 100}
Activation of AE layers	selu( $\cdot$ ), tanh( $\cdot$ )
Latent dimension	{1, 2, 3, 4, 5, 6, 7, 8, 9, 10, 12, 16, 18, 22, 24, 28, 32, 64}
Residual connections	True/False
Variational	True/False
Input/Output data scaling	$\mathcal{N}(0, 1)$
Noise level in the data	{1, 10, 100}
Weight decay rate	{0.0, 0.0001, 0.001}
Batch size	32
Initial learning rate	0.001

Table 8: LED Hyperparameters for Kuramoto-Sivashinsky

Hyperparameter	Values
Number of AE layers	{5}
Size of AE layers	{50}
Activation of AE layers	tanh( $\cdot$ )
Latent dimension	{8}
Residual connections	True
Variational	True/False
Input/Output data scaling	$\mathcal{N}(0, 1)$
Noise level in the data	{1, 10}
Weight decay rate	{0.0, 0.0001}
Batch size	32
Initial learning rate	0.001
BPTT sequence length	{125, 250}
Hidden state propagation length	1000
RNN cell type	{lstm, gru}
Number of RNN layers	{1, 2}
Size of RNN layers	{100, 200, 400}
Activation of RNN Cell	tanh( $\cdot$ )

## 9 Discussion

We have presented a novel data-driven framework for learning the effective dynamics (LED) and performing multiscale modeling on both stochastic and deterministic dynamical systems, extending the equation-free formalism with state of the art deep learning methods. LED is utilizing deep autoencoders to compress the high dimensional state to a few effective degrees of freedom in a latent space representation. A RNN is utilized to forecast the dynamics on this latent representation. In stochastic systems, a Mixture Density decoder is probabilistically mapping the reduced order latent space in the high dimensional state space.

In systems where evolving the high dimensional state dynamics based on first principles (solvers, equations, etc.) is computationally expensive, or time consuming, LED can accelerate the simulation by propagating on the latent space and then upscaling to high-dimensional system state with the decoder, when necessary. We demonstrate that LED can be orders of magnitudes faster than micro scale solvers, extending the simulation times that are possible with the solvers based on first principles. Moreover, we demonstrate how LED can be operated in a multiscale fashion, switching between propagation of the latent dynamics, and evolution of the micro dynamics, achieving lower error at the cost of reduced speed-up. In this way, a trade-off between accuracy and speed-up may be achieved. The efficiency of the proposed approach is evaluated on a stochastic dynamical system composed of 1000 particles following the Advection-Diffusion dynamics (AD) in one and three dimensions, the FitzHugh-Nagumo (FHN), and the chaotic Kuramoto-Sivashinsky (KS) equation.

We demonstrate that LED efficiently uncovers the meta stable regions in the AD dynamics in both one and three dimensions, capturing the distribution of the positions of the particles with low error, while being two orders of magnitude faster than the micro scale solver. Moreover, by utilizing the proposed multiscale forecasting scheme, we demonstrate that the statistical error is decreased as more time is spent evolving the particle dynamics, and the less time spent on the latent space of LED, albeit at the cost of lower computational savings. In addition, we demonstrated that the computational savings of LED increase for higher Péclet numbers (higher diffusion coefficient) albeit at the cost of slightly higher errors, and we demonstrated that LED can generalize to a different number of particles ( $N = 200$ ).

We evaluated the efficiency of LED in forecasting the evolution of the densities of the activator and the inhibitor in the FHN equation, and compared it with 8 variants of the equation-free approach based on uncovering a PDE model on the coarse level. LED variants exhibit one order of magnitude less mean normalised absolute difference (MNAD) on both predicted densities, while being two orders of magnitude faster compared to the Lattice Boltzmann method considered as the micro scale solver. Moreover, we tested the multiscale approach on the FHN, demonstrating that the error can be further reduced by utilizing the solver for some portion of the forecasting time, at the cost of reduced speed-up, achieving a compromise between the desired accuracy and execution time.

Last but not least, LED efficiently uncovered an  $d_z = 8$  dimensional reduced order manifold in the dynamics of the KS equation with  $L = 22$ . Even though LED is propagating the dynamics on this reduced order space, it is able to reproduce the statistics of the high dimensional space at the output of the decoder accurately and reproduce the long-term behavior (climate) of the KS equation for a large forecasting horizon, while being two orders of magnitude faster.

Scalability of the approach to more high dimensional problems and application to more realistic scenarios are matters of current research efforts. Further study is required in the analyzing the latent space that the LED autoencoders are learning. In this work, there is no guarantee that the components of the latent space are independent. Future work can be targeted at unraveling a statistically independent latent space. Moreover, the latent space can be used to efficiently classify various regions of the state space of each system and assist in understanding the different regions and their properties. Tailoring the proposed framework to the problem under study, might further improve its efficiency. For example, incorporating expert knowledge, e.g. with an additional physics based loss, may reduce the errors significantly, achieving even larger prediction horizons. Moreover, algorithmic advancements and optimization on the architectures used in this study may help achieve further speed-ups.

In summary, LED identifies and propagates the effective dynamics of dynamical systems with multiple spatiotemporal scales providing significant computational savings. Moreover, LED provides a systematic way of trading between speed-up and accuracy for a multiscale system by switching between propagation of the latent dynamics, and evolution of the original equations, iteratively correcting the statistical error at the cost of reduced speed-up. The present methodology can be deployed both in problems described by first principles as well as for problems where only data are available for either the macro or microscale descriptions of the system. Finally, by providing a bridge between data driven and first principles models LEDs open new horizons for the effective simulations of complex multiscale systems.